Title

EMPIRICAL PSEUDOPOTENTIAL METHOD FOR ELECTRONIC BAND STRUCTURE CALCULATIONS IN INSULATORS

Author

Fong, Ching-Yao.

Publication Date

1968-07-01

Thesis/dissertation

UCRL-18356

University of California

Ernest O. Lawrence Radiation Laboratory

EMPIRICAL PSEUDOPOTENTIAL METHOD FOR ELECTRONIC BAND STRUCTURE CALCULATIONS IN INSULATORS

Ching - Yao Fong
(Ph.D. Thesis)

July 1968

Berkeley, California

UCRL-18356

UNIVERSITY OF CALIFORNIA

Lawrence Radiation Laboratory
Berkeley, California
AEC Contract No. W-7405-eng-48

EMPIRICAL PSEUDOPOTENTIAL METHOD FOR ELECTRONIC BAND STRUCTURE CALCULATIONS IN INSULATORS

Ching - Yao Fong

(Ph.D. Thesis)

July 1968

TABLE OF CONTENTS

EMPIRICAL PSEUDOPOTENTIAL METHOD FOR ELECTRONIC BAND STRUCTURE CALCULATIONS IN INSULATORS

Ching - Yao Fong

Inorganic Materials Research Division, Lawrence Radiation Laboratory
and Department of Physics,
University of California, Berkeley, California

ABSTRACT

Electronic and structures are calculated by the "Empirical Pseudopotential Method" for three ionic crystals: MgO, NaCl and KCl. The pseudopotential form factors of the first two crystals are determined by assuming the potentials are local. For the case of KCl, an additional angular momentum dependent nonlocal pseudopotential is introduced. The imaginary part of the frequency dependent dielectric function, $\epsilon_2(\omega)$, calculated from the band structure is directly compared to the measured ultraviolet spectrum. Apart from the excitonic structure, the agreement of the $\epsilon_2(\omega)$ between theory and experiment for the position in energy of the prominent structure is within 0.1 eV for photon energy less than 14.0 eV, and 1.0 eV for higher photon energy. There exists discrepancy between the magnitudes of the calculated and the measured peaks and this is discussed. The complete critical point analysis enables us to identify all the prominent structure in the $\epsilon_2(\omega)$.

I. INTRODUCTION

Since 1930 when Hilsch and Pohl[1] first reported on the ultraviolet absorption measurements on alkali halides, a considerable amount of optical data at different temperatures have been obtained.[2] Most of these experiments were performed with photon energies from 5.0 to 12.0 eV. These results are difficult to interpret for two reasons. First, there is excitonic structure associated with high energy interband transitions in addition to the one at the band edge. Secondly, the measured quantity is the optical density,[2] ($\log_{10} \frac{I}{I_0}$, where I_0 is the intensity of the incident light, and I is the intensity of the transmitted light), which is equal to $\frac{\omega}{n(\omega)} \epsilon_2(\omega)$ where ω is the frequency of the incident light, $n(\omega)$ is the real part of the frequency dependent refractive index, and $\epsilon_2(\omega)$ is the imaginary part of the frequency dependent dielectric function. This is the quantity directly calculated from the theory. The corresponding peaks in the optical density and $\epsilon_2(\omega)$ may be shifted by the factor $\frac{\omega}{n(\omega)}$. Several reflectance measurements[3] on the alkali halides have been reported, but with photon energy only up to 12.0 eV, and an accurate $\epsilon_2(\omega)$ is not available. Roessler and Walker[4] recently obtained the $\epsilon_2(\omega)$ for Na Cl and KCl by measuring the reflectance over a wide range of photon energy (5 to 28 eV) and then these authors used the Kramers-Kronig relation to obtain $\epsilon_1(\omega)$ and $\epsilon_2(\omega)$. In the following discussion, we shall deal with these two alkali halides.

Theoretical interpretation of the optical data for the two crystals has not been very successful. Some attempts at calculating the band structure of NaCl were made by Shockley[5a] and Casella[5b] which give the valence bands only, and a rough calculation made by Tribbs.[5c] Howland[6a] calculated the valence band of KCl, and two other first principle calculations on KCl exist in the literature. The Orthogonalized Plane Waves (OPW) calculation by Oyama and Miyakawa[6b] gives the conduction bands only, and the Augmented Plane Waves (APW) calculation by DeCicco[6c] gives the fundamental energy gap of 6.5 eV, whereas experimentally it is 8.69 eV. A detailed comparison between theory and experiment is not available, and the dielectric function, $\epsilon_2(\omega)$, is not computed in these calculations.

The successful work done by M. L. Cohen and T. K. Bergstresser[7] on applying the Empirical Pseudopotential Method (EPM) to interpret the optical data of semiconductors and some II-VI compounds suggests a promising way to examine the optical data of NaCl and KCl.

The EPM is an ingeneous extension of the OPW method. It is based on the "Phillips' Cancellation Theorem,"[8] which has been explored by Cohen and Heine[9] and elaborated upon by Austin, Heine and Sham.[10] The Fourier coefficients of the effective crystalline potential -- Pseudopotential form factors -- are determined in one of two ways. First, they are determined by the model potential in real space.[11,12] The model potential is ℓ-dependent and the strength of the potential for particular ℓ is determined from the known energy of the corresponding atomic level. Secondly, the form factors are determined by reference to experimental data, e.g. optical data, de Haas-van Alphen data, etc. In our work, we adopted the second scheme. There are constraints on the empirical pseudopotential form factors. For example, the symmetric part for the form factors of a compound should be very close in numerical value to the form factors of a crystal composed of the element in the corresponding IV-th column of the periodic table. These constraints and experimental information are the basis for giving the correct interpretation of the optical spectrum by EPM. The eigenvalues calculated by the EPM characterize all the states of the valence electrons. The method has become one of the best tools for studying the Fermi surface of metals[13] and the optical properties in semiconductors.[7]

One may wonder whether the weak pseudopotential resulting from the Phillips' cancellation theorem will be a good description for the effective crystal potential in very ionic crystals. Physically, this can be made plausible because the valence electrons in these crystals are bound to the halogen ion; the core electron contribution to the potential tends to cancel the large part of strong nuclear attractive potential. To test this idea, it was decided to work on a less ionic crystal before extending the method to the alkali halides; this is the reason for choosing MgO. MgO is a light II-VI compound which has the structure of most alkali halides -- the rocksalt structure. It turns out that the spectrum of MgO is very much like that of NaCl, and results for MgO have helped us to interpret some of the important energy gaps for determining the form factors of NaCl. The experimental $\epsilon_2(\omega)$ for MgO was also obtained by Roessler and Walker.[14,15]

The spectrum of KCl is complicated by the kind of exciton structure we mentioned above. The exciton is identified as being associated with the lowering of the d like conduction band at X.[3,16] If a set of local pseudopotential form factors are chosen we do not obtain a band structure and an $\epsilon_2(\omega)$ which agrees well with experiment. We can, however, obtain good results and identify the optical structure by introducing an angular momentum dependent nonlocal pseudopotential with $\ell = 2$. This extra potential provides the necessity for treating the d-states on a different footing than the s and p states.

The arrangement of the present work is as follows: In section II, we give the results for the calculation of MgO. It contains two subsections. In part A we give a general discussion of the pseudopotential form factors and structure factors for the f.c.c. lattice with two atoms in a unit cell as a basis. This applies also to NaCl and the local pseudopotential of KCl. The calculation of the imaginary part of the frequency dependent dielectric function is also included. In part B a detailed analysis of the critical points for the interband transition of MgO and a comparison with the experimental spectrum are given. In section III we give the results for NaCl. This contains a brief discussion of the pseudopotential form factors, a complete critical point analysis, and the $\epsilon_2(\omega)$ for NaCl. In section IV the results of KCl are given. This section is divided into two subsections: A. Discussion is given on the angular momentum dependent nonlocal potential. B. We give the results of a critical point analysis and the $\epsilon_2(\omega)$ for KCl. In section V a comparison of the results for the three crystals is made. In subsection A we compare the results of MgO and NaCl. In subsection B the results of two alkali halides are compared.

II. MAGNESIUM OXIDE

The band structure calculation presented here employs the EPM. This method involves adjusting pseudopotential form factors to give the energies of a few of the principal optical transitions (e.g. the fundamental gap) to the experimentally identified values. These form factors are then used to determine the electronic energy bands over a wide range in energy and at many points in the first Brillouin zone. The discussion is confined to MgO. Nevertheless, it is equally applicable to NaCl and KCl, except the latter has an extra angular momentum dependent nonlocal pseudopotential. We shall discuss first the method of solving the pseudopotential Hamiltonian and the expressions used for calculating the $\epsilon_2(\omega)$.

A. Pseudopotential Hamiltonian

The pseudopotential Hamiltonian has the form

$$\mathcal{H} = -\frac{\hbar^2}{2m}\nabla^2 + V(\underline{r}) \tag{1}$$

The weak pseudopotential $V(\underline{r})$ is expanded in the reciprocal lattice vectors

$$V(\underline{r}) = \sum_{|\underline{G}|} V(\underline{G})\, e^{i\underline{G}\cdot\underline{r}} \tag{2}$$

where the $\underline{G}$'s are the reciprocal lattice vectors and are measured in units of $(2\pi/a)$, a is the lattice constant. The $V(\underline{G})$ are the pseudopotential form factors.

$$V(\underline{G}) = \sum_{\alpha} V_\alpha(\underline{G})\, S_\alpha(\underline{G}) \tag{3}$$

$$S_\alpha(\underline{G}) = e^{i\underline{G}\cdot\underline{\tau}_\alpha} \tag{4}$$

$$V_\alpha(\underline{G}) = \frac{1}{\Omega}\int_{\text{cell}} V_\alpha(\underline{r})\, e^{-i\underline{G}\cdot\underline{r}}\, d^3r \qquad (5)$$

where $S_\alpha(\underline{G})$ is the structure factor and is a function of the positions of the atoms in the unit cell. $V_\alpha(\underline{r})$ is the atomic pseudopotential, τ_α is the position vector of an atom in the unit cell, Ω is the volume of the unit cell, and α is the index of the atom in the unit cell.

Magnesium oxide as well as the other two alkali halides has the rocksalt structure (see Ref. 23, p. 24). We treat it as an f.c.c. lattice with a basis. The lattice constant, a, of MgO is 4.21Å. If the origin of the coordinate system is taken at a Mg site, the vectors $\underline{\tau}_1 = (0,0,0)$ and $\underline{\tau}_2 = a(\frac{1}{2},\frac{1}{2},\frac{1}{2})$ give the positions of the Mg and the O atoms in the cell. The structure factors are then ±1 depending on whether $|\underline{G}|^2$ is an even or odd integer. The form factors can be divided into symmetric and antisymmetric components as follows:

$$V(\underline{G}) = V_1(\underline{G}) + V_2(\underline{G}) = 2V^S_G \quad \text{for } |G|^2 \text{ even} \qquad (6)$$

$$V(\underline{G}) = V_1(\underline{G}) - V_2(\underline{G}) = 2V^A_G \quad \text{for } |G|^2 \text{ odd} \qquad (7)$$

where the subscripts 1 and 2 refer to the two atoms in the unit cell. V^S and V^A are the symmetric and antisymmetric form factors. In this way, we get a real symmetric matrix for the pseudopotential Hamiltonian when the wavefunction is expanded in plane wave states. The form factors are small for large $\underline{G}$ because of the Cancellation theorem;[8,9] this allows us to truncate the form factors. In all our cases, we set

$$V(|\underline{G}|^2) = V(\underline{G}) = 0 \qquad \text{for } |\underline{G}|^2 \geq 16 . \qquad (8)$$

and we have $V^A(3)$, $V^A(11)$; $V^S(4)$, $V^S(8)$, $V^S(12)$. These five form factors are treated as disposable parameters. We have taken some advantage from previous calculation on MgO,[14] in determining the form-factors. We started with the existing form factors and varied slightly to have five chosen energy gaps ($\Gamma_{15} \rightarrow \Gamma_1$, $\Gamma_{15} \rightarrow \Gamma_{25}$, $L_3 \rightarrow L_2{}'$, $L_3 \rightarrow L_3{}'$ and $X_5{}' \rightarrow X_1$) consistent with the identified experimental values. The comparison of the two sets of form factors are given in Table I. The basis states used to form the hamiltonian matrix elements consist of plane waves with wavevectors $\underline{G} + \underline{k}$, where $\underline{k}$ lies within the first Brillouin zone. We can use Lowdin perturbation theory as modified by Brust,[17] since only the lowest ten energy bands are needed and the form factors are truncated. All vectors, $\underline{G}$, such that $(\underline{G} + \underline{k})^2 \leq E_1$ form the basis and all vectors, $\underline{G}$, such that $E_1 < (\underline{G} + \underline{k})^2 \leq E_2$ are treated through perturbation theory. The convergence to the order of 0.1 eV for the few important energy gaps is obtained with $E_1 = 11.1$ and $E_2 = 32.1$. The size of the matrix is of the order of 50×50.

The determination of $\epsilon_2(\omega)$ requires a knowledge of the energy bands throughout the Brillouin zone[17] since this function has the form

$$\epsilon_2(\omega) = \frac{e^2h^2}{m} \sum_{i,j} \frac{2}{(2\pi)^3} \int \frac{f_{ij}(\underline{k})dS}{E_{ij}|\nabla_{\underline{k}}E_{ij}|} \qquad (9)$$

where e and m are the charge and mass of the electron and h is the Planck's constant;

$$f_{ij}(k) = \frac{2}{3m} \frac{|\langle \underline{k},i|\underline{P}|\underline{k},j|\rangle^2}{E_{ij}} \qquad (10)$$

is the interband oscillator strength and S is a surface of constant interband energy, and $E_{ij} = E_j - E_i = \hbar\omega$. The prominent optical structure in the $\epsilon_2(\omega)$ originates from Van Hove[18,19] singularities at the critical points (c.p.) where $|\nabla_{\underline{k}} E_{ij}| = 0$. These critical points can be classified[17] according to symmetry (minima, saddle points and maxima) M_0, M_1, M_2 and M_3.

Because of the cubic symmetry, the integral in (9) need only be calculated in 1/48 of the Brillouin zone.[17] The energy bands and the oscillator strengths have been computed at a mesh of 356 points in the subzone. Another 2×10^6 sampling points are chosen randomly by the Monte-Carlo method. The eigenvalues and the oscillator strengths associated with each random point are obtained by interpolation between the points on the mesh.

B. Critical Points Analysis for MgO

The band structure of MgO is given in Fig. 1 along several symmetry lines in the Brillouin zone. The lowest band, at about 25 eV below the top of the valence band, is given only for completeness. It is not expected that the pseudopotential calculation determines the energy of this band accurately. Since the optical structure discussed in this work originates from transitions involving the upper valence bands and the lower conduction bands, the inaccuracy in determining the lowest valence band has no effect on the results of the $\epsilon_2(\omega)$ calculation.

The theoretical and experimental values for the energies of the prominent optical structure in $\epsilon_2(\omega)$ are listed in Table II. The calculated critical point energies, the associated band transitions and the symmetry of the critical points are given in Table III. Figure 2 gives the calculated $\epsilon_2(\omega)$ assuming constant matrix elements in Eq. (9). In Fig. 3, $\epsilon_2(\omega)$ is plotted with matrix elements computed using pseudopotential wavefunctions.

The top of the valence band and the bottom of the conduction band are both at Γ and the fundamental gap is therefore direct. The exciton associated with this gap has been studied,[14,15,20] and the line shape was fitted by a Lorentzian curve yielding an experimental gap energy of 7.77 eV. The theoretical value for $\Gamma_{15} \rightarrow \Gamma_1$ is 7.76 eV and the c.p. has M_0 symmetry as is shown in the total $\epsilon_2(\omega)$. The energy contours are given in Figs. 4, 5, and 6 and the ϵ_2's for the transitions between bands 4 and 5 is given in Fig. 7.

It is interesting to note that the band structure calculation gives some fine structure in the conduction band near Γ. The conduction band in the X direction is flat near Γ and then "dips" about 0.07 eV at a k-vector which is approximately 3% of the Brillouin zone k-vector. This structure is relatively insensitive to the variations in the pseudopotential. It is difficult at this time to determine whether the effects of this structure can be observed or if it is connected with the structure seen in the exciton peak.

The next structure in $\epsilon_2(\omega)$ which appears around 11 eV arises from $4 \rightarrow 5$ and $3 \rightarrow 5$ band transitions (Figs. 2,4,5 and 7). This structure is associated with $L_3 \rightarrow L_2'$ and $\Lambda_3 \rightarrow \Lambda_1$ transitions with c.p. symmetry M_0 and M_1. The M_0 c.p. lies only slightly below the M_1 c.p. in energy and as can be seen from the ΓKL plane energy contours of Figs. 4 and 5, a broad region of the zone near L contributes to the 11.1 eV peak. Although in this work we are primarily interested in the identification of the optical structure and in the determination of the energy of this structure and only secondarily in the peak heights, we note that over the entire energy range most of the peak heights are in relatively good agreement with experiment, except that the "L --Λ" peak is too small in the calculated $\epsilon_2(\omega)$ as calculated with constant matrix elements and with pseudo potential wavefunction matrix elements. This discrepancy also exists for the corresponding peaks in GaAs[21] and other zincblende compounds.[22] It is not clear at present why this structure is too small. Some possible explanations are: 1) the pseudopotential wavefunctions are not giving accurate transition matrix elements; 2) excitonic structure is associated with Λ transitions; 3) local field corrections. There is some experimental evidence for the second explanation.[22] We note that if this structure were stronger in the $\epsilon_2(\omega)$, the energy region between 7.77 eV and 11.0 eV would be "filled in," and the theoretical $\epsilon_2(\omega)$ would look much more like the experimental curve in this region.

The peak centered around 13.2 eV is the most prominent peak in the spectrum. This structure is caused by $4 \rightarrow 5$ and $3 \rightarrow 5$ transitions along Δ and $4 \rightarrow 5$ transition along Σ (Figs. 4, 5 and 7). The structure begins with an M_0 c.p. at 12.35 eV arising from $X_5' \rightarrow X_1$ transitions (Figs. 4 and 5). The main peak is caused primarily by $4 \rightarrow 5$ transitions; in particular, an M_1 along Δ and an M_2 along Σ. This peak is usually referred to as the "X-peak" because this structure varies in the same way as the $X_5' \rightarrow X_1$ splitting with changes in the potential. The shape of the calculated "X-peak" (see Fig. 3) is very close to the measured structure observed by Roessler and Walker.[15]

The lack of structure between about 14 and 15 eV is very interesting and it appears in both the calculated and measured $\epsilon_2(\omega)$. This region represents the separation between $4 \rightarrow 5$ and $3 \rightarrow 5$ band transitions, i.e. the top two valence bands and the bottom conduction bands, and transitions involving lower valence bands and higher conduction bands. There is one exception to this, the $4 \rightarrow 6$ transition $X_5' \rightarrow X_3$ is found to be at 14.02 eV which is at the beginning of this "dip" region, but this transition contributes only a weak M_0 c.p. (Figs. 2, 8 and 9), and we assign it to the 14 eV region in the experimental curve.

The structure in $\epsilon_2(\omega)$ above 15 eV arises from $2 \rightarrow 5,6,7$; $3 \rightarrow 5,6,7$ and $4 \rightarrow 6,7$ band transitions. The energy contours for these transitions are given in Figs. 5 through 14. The calculated energies for the dominant transitions differ from the experiment by about one eV, and the experimental structure is broader than the theoretical structure in this region (Fig. 3).

The measured $\epsilon_2(\omega)$ shows a "twin peaks" structure in the 15.5 eV to 18.0 eV range with smaller structures on the low and high energy sides of this region. Similar structure is seen in the calculated $\epsilon_2(\omega)$ in the 15.2 eV to 17.0 eV region as shown in Fig. 3. There are many c.p.'s which contribute to $\epsilon_2(\omega)$ in this region, but we will discuss only the strongest of these. It should be emphasized that the agreement between experiment and theory in this region is lost if the potential is slightly changed.

For energies just above 15 eV, the calculated $\epsilon_2(\omega)$ rises more sharply than the measured $\epsilon_2(\omega)$ in the corresponding energy region (~ 15.5 eV), indicating that the calculated c.p.'s are probably closer together in energy than they should be. The beginning structure is caused by two M_0 c.p.'s and an M_1 c.p. . The M_0's contribute strongly since they involve transitions between doubly degenerate ($L_3 \rightarrow L_3'$ at 15.2 eV) and triply degenerate ($\Gamma_{15} \rightarrow \Gamma_{25}$ at 15.43 eV) bands. The M_1 c.p. at 15.35 eV is also strong and it arises from $\Delta_1 \rightarrow \Delta_1$ transitions (Figs. 6, 10).

The region around 15.6 eV also involves several transitions; $4 \rightarrow 6$ transitions contribute strongly. The two main c.p.'s involved come from $\Delta_5 \rightarrow \Delta_2'$ and $\Sigma_4 \rightarrow \Sigma_1$ transitions near Γ. In both cases, however, the region close to the c.p. contributes rather weakly, and the contributions come from an extended region of the zone (Figs. 9, 10 and 11). In contrast, the c.p. $\Delta_5 \rightarrow \Delta_2'$ at 15.57 eV, coming from $3 \rightarrow 6$ transitions, contributes strongly in this region and the characteristics of this c.p. are not "smeared out" by the large background. A $\Sigma_3 \rightarrow \Sigma_1$ M_2 c.p. at 15.66 eV, coming from $3 \rightarrow 5$ transitions, also contributes strongly in this region.

The second peak of the "twin peaks" structure begins with a strong peak coming from a transition between doubly degenerate bands, $\Lambda_3 \rightarrow \Lambda_3$. The c.p.'s arising from these transitions have both M_2 and M_3 characters. The strong M_3 c.p. caused by $4 \rightarrow 7$ transitions tends to flatten the peak in this region. The structure at 16.4 eV and 16.6 eV arises from $4 \rightarrow 7$ and $3 \rightarrow 7$ transitions. The $\Sigma_4 \rightarrow \Sigma_2$ and $\Delta_5 \rightarrow \Delta_1$ M_3 c.p.'s contribute to the $4 \rightarrow 7$ transitions and regions near Δ and Σ contribute to the $3 \rightarrow 7$ peak (Figs. 2, 13 and 14).

The decrease in $\epsilon_2(\omega)$ in the experimental curve in this region is less rapid than the calculated curve. Again, the c.p.'s may lie too close together in energy. The main contributions in this region come from $\Delta_5 \rightarrow \Delta_1$ transitions at 17.01 eV.

The measured $\epsilon_2(\omega)$ shows little structure for energies above 17 eV except for a bump around 20.5 eV. The $\epsilon_2(\omega)$ in the region from 18 to 20 eV is still fairly large, and it is possible that this structure exists which has not been resolved. The calculated $\epsilon_2(\omega)$ with constant matrix elements does show some structure in this region. The $\epsilon_2(\omega)$ with pseudopotential wavefunction matrix elements has just a "hint" of this structure, and it resembles the measured $\epsilon_2(\omega)$. The origin of the main structure is listed in Table III. The bump in the constant matrix element $\epsilon_2(\omega)$ (Fig.2) at 19 eV comes from $4 \rightarrow 6$ transitions (Figs. 8 and 9) in a region near W. The small structure around 20.5 eV in Fig. 3 comes from $4 \rightarrow 7$ transitions near K and $3 \rightarrow 7$ transitions near W. It is difficult at this time to make a detailed comparison of the calculated curve with experiment because of the lack of experimental structure. More refined measurements of the spectrum in this region would be very helpful. Such measurements would make these assignments possible.

The function $\epsilon_2(\omega)$ as given in Fig. 3 was used to obtain $\epsilon_2(\omega)$ by means of the Kramers-Kronig relation. The $\epsilon_2(\omega)$ function in Fig. 3 was multiplied by a scale factor 1.1 before the Kramers-Kronig analysis was done. The resulting $\epsilon_1(\omega)$ appears in Fig. 15. Since the theoretical $\epsilon_2(\omega)$ does not contain the exciton peak and the $\epsilon_2(\omega)$ in the region of 8 to 11 eV is too flat, the ϵ_1 is not very accurate in this region. In fact, a peak occurs near the threshold. The measured dip between 11 and 12 eV is reproduced and the general shape of the rest of the curve is very similar to the curve derived from experiment. The calculated ϵ_1 goes to zero at 20 eV and we pick this as the plasma energy. The measured plasma energy quoted by ref. 15 is 22.2 eV.

Using the calculated values for $\epsilon_1(\omega)$ and $\epsilon_2(\omega)$ and the standard semi-infinite plane boundary conditions, the reflectivity, $R(\omega)$, is calculated as a function of energy. This curve appears in Fig. 16. The peak in $\epsilon_1(\omega)$ below 8 eV causes a peak in this energy range; the next prominent structure is at 11 eV arising from $\Lambda_3 \rightarrow \Lambda_1$ transitions. The $R(\omega)$ curve strongly resembles the $\epsilon_2(\omega)$ in Fig. 3 for energies below 15 eV, as is expected. The shapes, heights and energies of the measured and calculated optical structure in this region are in good agreement with experiment. For higher energies, our reflectivity drops faster than the experimental reflectivity; this is due to the fact that the calculated ϵ_2 is low for the L peak as discussed before.

The functions $\epsilon_1(\omega)$ and $\epsilon_2(\omega)$ are also used to calculate $\mathrm{Im}[\frac{1}{\epsilon(\omega)}]$; this curve is plotted in Fig. 17. At low energies of the peaks in these curves exactly coincide with the ones in $\mathrm{Im}[\frac{1}{\epsilon(\omega)}]$ obtained from the optical data while at high energies the shape is very close to the results of electron energy loss experiment.

III. SODIUM CHLORIDE

The optical spectrum of NaCl is similar to that of MgO,[4,14,15] and it was therefore expected that the electronic band structures of these two crystals should be similar. The method described in subsection A of section II applies equally well to NaCl, because both materials have the same crystal structure. The lattice constant, a, of NaCl is 5.63Å. The starting set of pseudopotential form factors for the symmetric part of the potential were obtained by scaling the silicon potential[7] for the lattice constant of sodium chloride. The results after scaling and the actual values used in the calculation are listed in Table IV. They differ by about 0.01 Ryd. We expect the form factors at high $|\underline{G}|$ values to have larger difference because of the truncation, the results, however, are close to the scaled values. The starting antisymmetric part of the potential was obtained by scaling the MgO form factors. The actual values used in the present calculation are given in Table V. Our $V^A(11)$ is negative, and this can be explained in the following way: The choice of the origin at the metallic ion causes the structure factor of the halogen ion to be -1, and $V^A(\underline{G}) = \frac{1}{2}\left(V_{Na}(\underline{G}) - V_{Cl}(\underline{G})\right)$ as shown in Eq. (7). The form factors at high $|\underline{G}|$ values reflect the localization of the potential and since in alkali halides, the valence electrons are near the halogen ion, they see a large potential due to halogen ion. As a result, $V_{Cl}(\underline{G})$ is larger than $V_{Na}(\underline{G})$ and $V^A(\underline{G})$ is negative. The energies E_1 and E_2 used in this calculation are the same as used for MgO. The convergence is of the order of 0.1 eV, for the main energy gaps; they are $\Gamma_{15} \rightarrow \Gamma_1$, $L_3 \rightarrow L_2'$, $\Sigma_4 \rightarrow \Sigma_1$, $\Gamma_{15} \rightarrow \Gamma_{25}'$, $L_3 \rightarrow L_3'$.

The resulting band structure is given in Fig. 18. The band structure bears an overall similarity to the band structure of MgO, but some of the energy splittings are different (e.g. the $\Gamma_{15} \rightarrow \Gamma_1$ gap in MgO is 7.77 eV). Another difference between MgO and NaCl is that there is less dispersion in the energies of the various bands as a function of wavevector. The major difference, however, is the relative lowering of the upper conduction bands (bands 6 through 10). These bands contain d-wave components, and they are lowered to such an extent that in the calculation we find that the X_3 level lies below the X_1 level. It is difficult to check this experimentally. The lowest valence band is included for completeness, but it is not expected that the EPM will give the energies of this band accurately. The comparison of the values of the energies of the prominent optical structure in the $\epsilon_2(\omega)$ are listed in Table VI. Table VII gives the complete lists of c.p.'s for transitions from 2, 3, 4 bands to 5, 6, 7 bands.

Figure 19 gives the calculated $\epsilon_2(\omega)$ assuming constant matrix elements in Eq. (9) and Fig. 20 give the $\epsilon_2(\omega)$ with matrix elements computed with pseudopotential wavefunctions. The relative heights of the peaks shown in Fig. 20 are consistent with experiment. We have, however, used an overall scale factor of 0.6 in the calculated $\epsilon_2(\omega)$ to make the main peak at 11.1 eV agree with the corresponding experimental value. The curve is plotted up to an energy of 18 eV; the sum rule for the theoretical curve is obviously not obeyed, because of the scale factor.

The exciton appearing at 7.73 eV (300°K) and the structure near the fundamental gap agree very well for the two measurements.[3,4] The exciton structure which is well separated from the band edge has been examined at low temperatures, and the spin-orbit splitting and higher order lines in the exciton series have been observed.[3,4] The exciton structure is not included in the theoretical $\epsilon_2(\omega)$. The fundamental gap $\Gamma_{15} \rightarrow \Gamma_1$ was adjusted to 8.97 eV to agree with the gap determined experimentally. It has M_0 symmetry as shown in the energy contours (Figs. 21, 24, 27). The exciton is associated with this edge.

The next structure arises from transitions along the [111] direction, i.e. an M_0 c.p. at 9.86 eV arising from $L_3 \rightarrow L_2'$ transitions and an M_2 c.p. at 10.29 eV coming from $\Lambda_3 \rightarrow \Lambda_1$ transitions, (Figs. 21 and 24). We think it is this M_2 type singularity which causes the distinct shape of the corresponding peaks for NaCl and MgO. Experimentally, NaCl has a round smeared out peak, whereas MgO has a sharp peak. A differential reflectance measurement near this energy region would be very helpful for this identification. The magnitude of this structure differs greatly between experiment and theory as it does in MgO, GaAs and other zincblende compounds as we mentioned in section II. In the latter case, part of $L - \Lambda$ structure is masked by the prominent $\Sigma - \Delta - X$ peak around 11 eV.

As in MgO and in the zincblende structures, the largest interband peak of NaCl in the optical spectrum comes from transitions along Δ and Σ (see Table VI, Figs. 20 and 21). The magnitude of this peak is strengthened by a large region in the k-space (Fig. 21). As we mentioned above the X_3 level is lowered and is nearly degenerate with X_1 (Fig. 18). The lowering of X_3 does not affect the optical structure greatly in this region. As we will show later, X_3 is even lower in KCl, this has a large effect on the spectrum.

Because of the lowering of the upper conduction bands in NaCl the wide dip in $\epsilon_2(\omega)$ around 14.5 eV in MgO is absent in the corresponding 11-12 eV region in NaCl. However, there are quite a few weak c.p.'s arising from the Δ and Σ regions (Table VII).

The peak at 12.26 eV is the most distinct structure in the $\epsilon_2(\omega)$ for NaCl compared to the $\epsilon_2(\omega)$ for MgO (Figs. 3 and 20). The matrix elements for the individual interband transitions show the dominant contribution arising from an M_1 type singularity from $L_3 \rightarrow L_3'$ $(4 \rightarrow 6)$, and the M_0 type c.p. at L for $4 \rightarrow 7$, $3 \rightarrow 6$, $3 \rightarrow 7$ transitions (Figs. 22, 25, 27 and 28). The energy contours for 12.25 eV shown in Figs. 22 and 25 contribute to the background of the peak.

The next structure in the calculated ϵ_2 is at 13 eV which is 0.3 eV lower than the corresponding one in the experimental curve (see Fig. 20). We attribute the discrepancy to be due to the pseudopotential which as chosen does not include the energy dependent part. The peak starts with an M_0 c.p. arising from $\Gamma_{15} \rightarrow \Gamma_{25}'$ with energy 12.67 eV. The c.p.'s in this region are quite complicated. A strong M_1 c.p. from $\Delta_5 - \Delta_2'$ (Fig. 22) follows the Γ transitions; these form a weak peak at 12.7 eV. Another strong contribution from $\Lambda_3 \rightarrow \Lambda_3$ $(3 \rightarrow 7)$ transitions (Fig. 26) causes the peak at 13 eV. As in the case of MgO, the volume effects are large for this energy range (Figs. 23, 25, 26, 28 and 29). This structure resembles the twin peaks structure in MgO, it is not clearly shown in the $\epsilon_2(\omega)$(Fig. 20) because of the lack of dispersion in the energy bands as a function of wave vectors in this energy range. The rounded peak in the experimental curve does not resolve the fine structure either. The c.p.'s with energy higher than 13.6 eV are listed in Table VII, but we do not expect these energy determinations to be calculated very accurately because of the omission of the energy dependence of the pseudopotential at high energy. The theoretical and experimental ϵ_2 both drop in this energy range.

We also note that we confirm many of the assignments made by Roessler and Walker[4] who used the MgO band structure as a prototype (Table VI).

IV. POTASSIUM CHLORIDE

A. Pseudopotential Hamiltonian with $\ell = 2$ Nonlocal Term

KCl has the same crystal structure as NaCl, and the method described in section II for the local pseudopotential applies for this case. We start with a set of form factors which are scaled to the lattice constant of KCl from an average of the form factors for sodium chloride and germanium[7] for the symmetric part, and from MgO for the antisymmetric part. By adjustment we tried to fix the energy at the fundamental gap to be 8.69 eV. The resulting spectrum looks very much like the one for NaCl. Experimentally, we see the two spectra are completely different. This led us to suspect that the simple local pseudopotential approximation has to be augmented for the case of KCl, and a nonlocal potential was tried. The valence electrons in KCl are the (4s) electron of the K^+ ion and the $(3s)^2(3p)^5$ electrons of the Cl^- ion. The core states of KCl have mainly s and p characters. So the approximation that there is complete cancellation for s and p states in the local pseudopotential should be reasonable. For the d-like conduction electrons, there will be no complete cancellation, and these bands cannot be treated on an equal footing as the s and p bands. Thus we add the nonlocal potential term only for $\ell=2$.

The pseudopotential hamiltonian has the following form:

$$H = -\left(\frac{\hbar^2}{2m}\right)\nabla^2 + V(\underline{r}) + V_{NL}(\underline{r}) \qquad (11)$$

where the first two terms on the right hand side are the same as in Eq. (1), V_{NL} is the nonlocal pseudopotential term.

We know from studies of the atomic energy level that the energy of the d-state will be closer to the $(3p)^6$ core states in K^+ ion than the $(2p)^6$ core for the Cl^- ion. The effect of the core contribution to the nonlocal pseudopotential is primarily from the K^+ ion. The form of the d-character nonlocal potential[22] is

$$V_{NL} = \sum_{\underline{R}_j} V_2(\underline{r} - \underline{R}_j)\, P_2^{\ell}\, P_2^{r} \tag{12}$$

where $\underline{R}_j$ is the lattice vector. P_2^{ℓ} is the projection operator which acts on the left when the matrix elements of V_{NL} are taken and projects out only $\ell = 2$ component. P_2^r is the same kind of operator but acts on the right and

$$\begin{aligned} V_2(\underline{r} - \underline{R}_j) &= A_2 \qquad \text{for } |\underline{r} - \underline{R}| \leq R_s \\ &= 0 \qquad \text{for } |\underline{r} - \underline{R}| > R_s \end{aligned}$$

where A_2 is treated as disposable parameter and is the depth of the square well. R_s is the radius for the square well. It is determined from the potassium ion.[23]

The matrix elements of V_{NL} are evaluated over plane wave states with energy less than or equal to E_1. The algebra is shown in Appendix I. We have neglected the matrix elements for those plane waves with energy between E_1 and E_2. The resultant matrix elements of the potential energy are the sum of the matrix elements for the local pseudopotential and the $\ell = 2$ nonlocal pseudopotential. When the convergence of the eigenvalues is tested, we find that in order to have the variations of the eigenvalues at the symmetry points, such as Γ, X, L, within 0.1 eV, we need E_1 and E_2 equal to 16.1 and 38.1 respectively. The size of the matrix is of the order of 65×65.

B. Numerical Results and Critical Point Analysis for KCl

The numerical values of the form factors are given in Table VIII, with the comparison of the scaled form factors. This calculation gives only rough agreement because of the following two reasons. First, our attention is mostly restricted to the low energy peaks in the spectrum. Better agreement for high energy part ($\hbar\omega > 13.0$ eV) for the spectrum by putting the $\ell = 2$ nonlocal potential may be possible if the truncation of the local pseudopotential at $|\underline{G}|^2 = 16$ was pushed to higher values. Secondly, the large size of the matrix at each $\underline{k}$ in the first Brillouin zone requires an excessive amount of computer time, this restricted us to a rough analysis.

The band structure of KCl is plotted in Fig. 30. The order of the conduction bands are very similar to that obtained by the OPW method,[6b] however, our results show less dispersion for the energy as a function of wavevector. The valence bands are consistent with the results of the APW method.[6c] Figures 31 and 32 give the $\epsilon_2(\omega)$ with constant matrix elements and with matrix elements computed from the pseudo potential wavefunctions, respectively. The scale factor used to reduce the main peak in the calculated ϵ_2 to the experimental value is 0.41. The decreasing of the scale factors from MgO to KCl is consistent with the extent of the complication of the exciton structure and we shall discuss this point in section V. The exciton at the fundamental edge has been studied extensively.[3,4] The peak is at 7.5 eV (300°K). The calculated $\epsilon_2(\omega)$

starts at 8.69 eV with an M_0 type singularity (Figs. 33, 36, 39). The peak at 9.8 eV in the experimental curve is temperature dependent;[3,4] there is no corresponding peak in the spectrum of NaCl. It must be associated with the difference of the K^+ ion and the Na^+ ion. As we mentioned previously, the K^+ ion has a $(3p)^6$ core whereas Na^+ has a $(2p)^6$ core; the conduction bands with 3d-character states therefore lower in KCl than in NaCl and the exciton is identified as the X_3 exciton.[3,4] The calculated ϵ_2 does not include this peak. The next structure is at the beginning of sharp rise in the calculated ϵ_2, it arises from $X_5 - X_3$ transitions at 10.06 eV with c.p. symmetry M_0. The matrix element of this transition is large. The conduction band at X_3 is the lowest energy band above the edge at Γ_1 (Fig. 30). The exciton structure at 9.8 eV is associated with this gap and the binding energy for the exciton is of the order of 0.15 eV. The $L_3 - L_2'$ and $\Lambda_3 - \Lambda_1$ transitions are at 10.08 eV and 10.14 eV with M_0 and M_1 type of c.p.'s respectively. The small sharp peak at 10.4 eV in the experimental ϵ_2 is identified as $\Delta_5' - \Delta_1'$ transitions at 10.44 eV with symmetry M_1 (Tables IX, X and Figs. 33 and 36). The value of $\underline{k}$ in the first BZ where the transitions occur is at the crossing of the 5 and 6th bands in the [100] direction. The calculated strength of the peak is rather high compared to the experimental data. We think most of the oscillator strengths associated with $X_5' - X_3$ transitions and $\Delta_5 - \Delta_1'$ transitions are taken away by the strong exciton structure at 9.8 eV (see Fig. 32). We therefore confirm the identification of the 9.8 eV peak. We note in addition that in this crossing region, there are a few weak M_0 c.p.'s at 10.5 eV from $4 \rightarrow 6$, $3 \rightarrow 6$ and $2 \rightarrow 6$ transitions (Figs. 34, 37, 39). The transition at

$X_5' \rightarrow X_1$ contributes a very weak M_0 c.p. at 10.52 eV. This structure ends at 10.97 eV with an M_2 type c.p. arising from $\Sigma_4 \rightarrow \Sigma_1$ $(4 \rightarrow 6)$ transitions. This peak corresponds to the usual X-Δ-Σ peak in MgO, NaCl and other crystals with the zincblende structure. However, the strong c.p.'s which contribute to the beginning of the structure come from transitions of p-like states to d-like states.

The c.p.'s between 11 eV to 11.45 eV are listed in Table X. There are large regions in the BZ which contribute to the ϵ_2 in this energy range (Figs. 34,36,37 and 39). The calculated ϵ_2 resembles the experimental ϵ_2 in this region, but it is one of the difficult parts in the process of determining the form factors. The transitions from $\Gamma_{15} \rightarrow \Gamma_{25}'$ is at 11.45 eV and the c.p.'s associated with these transitions are complicated. All the transitions from the valence bands to the 6th band have M_3 symmetry because of the lowering of X_3, Σ_3, and Λ_1. The transitions from the valence bands to the 7th band cause an M_0 (Figs. 34, 35, 37, 38 39 and 40); this occurs at the beginning of the broad peak in the ϵ_2. The strongest contribution for the broad peak is mainly from volume effects i.e., large region in the BZ with interband energy differences of interest. The interband energy contours are shown in Figs. 35, 37, 38, 40 and 41. The hump in the experimental curve starts at 11.5 eV and ends at 11.8 eV. The calculated results show a rise at 11.5 eV which ends at 11.9 eV. No c.p. is found in this region of energy (Table X). The slope at 11.5 eV differes from the experimental results; we believe that the calculated band structure may not have enough density of states in the region near 11.5 eV. The calculated ϵ_2 has a peak at 12.15 eV which is 0.35 eV lower than the experimentally measured value. The strongest contribution near 12.15 eV comes from the $4 \rightarrow 7$ transitions at L with an energy of 12.13 eV having M_1 symmetry. The experimental ϵ_2 drops rapidly with energy larger than 12.5 eV. The calculated ϵ_2 shows a sharp drop after the corresponding peak at an energy of 12.15 eV. The other c.p.'s up to 13.31 eV are included in Table X, they are mostly singularities of type M_2 and M_3. The calculated spectrum is cut off at 14 eV, so the overall sum rule is not obeyed.

The Γ_{12} band is included in Fig. 30 and it is farther from Γ'_{25} than in the OPW and APW calculations. We have investigated the effect of V_{NL} on this band. The energy value obtained by setting V_{NL} equal to zero gives a higher Γ_{12}, i.e., the $\Gamma_{15} \rightarrow \Gamma_{12}$ transitions are at 14.9 eV. The $\ell = 2$ nonlocal pseudopotential does bring down the Γ_{12} band. At present, we leave this question open; a density of states measurements (e.g. X-ray measurements) on KCl would help to determine the exact energy for Γ_{12}.

V. COMPARISON OF THE RESULTS FOR THE THREE CRYSTALS: MgO, NaCl and KCL

The spectra of MgO and NaCl resemble each other, whereas KCl has its own distinct spectrum. We shall compare the results of MgO and NaCl first, and then we go on to compare the results of the two alkali halides.

A. Comparison of MgO and NaCl

The band structure of MgO shows larger E(k) dispersion than the band structure of NaCl. The exciton structure is different in the two cases. MgO has a larger static dielectric constant (9.8, see ref. 23, p. 156) than NaCl ($\epsilon_0 = 5.9$). The effective mass at the band edge is smaller in the case of MgO (see the curvature for the two band structures at Γ, Figs. 1 and 18). The exciton binding energy is 0.1 eV in MgO and 1 eV in NaCl. We also see that the intensities of the peaks near the edge are different, in MgO, ϵ_2 is 5.4 and in NaCl, it is 6.8. The overall resemblence of the two spectra is remarkable. Physically, the two crystals have the same core states for the metallic ions. MgO has a complete $(2p)^6$ core at the O^{--} ion and NaCl has the complete $(3p)^6$ core states at the Cl^- ion. The effect of upper d-band is small. No drastic change in band structure and ϵ_2 are expected. However, there are slight differences in the [111] direction. At 11.1 eV in MgO and 9.8 eV in NaCl, the shapes of the peaks are different because of the M_1 type singularity for $\Lambda_3 \rightarrow \Lambda_1$ transitions in MgO and the M_2 type c.p. for the corresponding transitions in NaCl. The largest difference in the spectra is the extra peak at 12.25 eV in NaCl which has no corresponding peak in the MgO spectrum. The peak is identified as coming mainly from $L_3 \rightarrow L_3'$ transitions. We can see this qualitatively because the conduction band states of the ionic crystals are orthogonal to the valence band states, and they localize at the metallic ion.[24] At Γ, the ordering of the conduction bands must be consistent with the atomic levels of the metallic ion. Na^+ and Mg^{++} have the same core states and the numerical values of Γ_{25}' with reference to the valence band must be higher in MgO than in the case of NaCl, because the O^{--} have a $(2p)^6$ shell and Cl^- has a $(3p)^6$ shell. We have seen that in MgO, Γ_{25}' is 15.6 eV from the top of valence band and is 12.67 eV in NaCl. For $\underline{k}$ equal to zone edge value in the [111] direction, the charge density of the conduction band states will not be localized at the metallic ion. The energy of the level must be some value between the corresponding atomic levels of the two constituent atoms. For example, since the charge density is localized at the halogen ion, its energy must be consistent with the atomic level of the halogen ion. In NaCl, the unfilled 3d states are closer to $(3p)^6$ states of the Cl^- ion than the $(2p)^6$ states in the O^{--} ion. We would expect that the L_3' levels in NaCl are lower and farther apart from Γ_{25}' as compared with the case of MgO. We have checked the charge density by using the pseudopotential wavefunctions for $\underline{k} = (0,0,0)$ and $\underline{k} = (2\pi/a)(1/2, 1/2, 1/2)$ and showed that the above is in fact the case. The oscillator strength of ϵ_2 is large up to 15 eV in NaCl whereas MgO has considerable strength up to 20 eV.

B. Comparison of NaCl and KCl

The band structures for the two crystals show some common characteristics, i.e., little dispersion of the energies with respect to the wavevectors. The binding energy of the exciton at the fundamental edge is of the same order of magnitude ~ 1 eV. The measured spectra, however, show great difference. The sharp peak at 9.8 eV in KCl, which is strongly temperature dependent,[3,4] does not have a counterpart in NaCl. As we mentioned in section IV, the difference is attributed to the unfilled nearby 3d states in K^+ ion, because Na has a complete n = 2 shell and one 3s electron, and K has a complete n = 3 shell and one 4s electron. The band formed by the unfilled 3d states does not have complete cancellation from the core states which have mainly s and p characters. The valence bands should be the same for the two alkali halides. We can compare the numerical values of the energies for NaCl and KCl. We then see that the s-like band, i.e., the fifth band, does not differ so much for the two crystals. The Γ_{25}' band has d-character and is lowered by half a volt for KCl compared to NaCl. If we use our simple argument again, we expect the energy of L_3' in both crystals to be close with respect to the top of valence band, and slightly lower in KCl. The numerical values of L_3' in NaCl is 12.2 eV and in KCl 12.02 eV. The effect of lowering the d-like bands in KCl not only causes the interband transitions to differ from NaCl, for example the X-Δ-Σ peak discussed in subsection B of section IV, but the lowering also causes an additional exciton peak at 9.8 eV. The X_3 level in KCl is 0.48 eV lower than X_1 whereas in NaCl, the two bands are nearly degenerate. The oscillator strengths for both crystals are large at energies below 15 eV. We have taken the Cl potentials from the results of the two crystals. The results are plotted in Fig. 42 and they agree very well.

Finally, the scale factor which we used to adjust the main peak in the theory to the experimental value is closest to unity in MgO. The exciton in MgO is relatively weakly bound. In NaCl, the scale factor is 0.6. The extra X_3 exciton in KCl causes further decreasing of the scale factor. Although we include 10 bands in the ϵ_2 calculations, the sum rule is not obeyed, the general trend of the weakening of the strength of the interband transitions because of exciton effects is clear because the overall sum rule must be obeyed by the experiment and theory.

FIGURE CAPTIONS

MgO

Fig. 1	Electronic energy band structure of MgO
Fig. 2	Theoretical $\epsilon_2(\omega)$ with constant matrix elements.
Fig. 3	Theoretical $\epsilon_2(\omega)$ with matrix elements computed using pseudo-potential wavefunctions.
Fig. 4	Energy contours for 4 → 5 transitions in the ΓKL and ΓKWX planes.
Fig. 5	Energy contours for 3 → 5 transitions in the ΓKL and ΓKWX planes.
Fig. 6	Energy contours for 2 → 5 transitions in the ΓKL and ΓKWX planes.
Fig. 7	Contributions to ϵ_2 from 4 → 5 transitions.
Fig. 8	Contributions to ϵ_2 from 4 → 6 transitions.
Fig. 9	Energy contours for 4 → 6 transitions in the ΓKL and ΓKWX.
Fig.10	Energy contours for 3 → 6, 4 → 6, and 2 → 5 transitions in the ΓXU plane.
Fig.11	Energy contours for 3 → 6 transitions in the ΓKL and ΓKWX planes.
Fig.12	Energy contours for 2 → 6 transitions in the ΓKL and ΓKWX planes.
Fig.13	Energy contours for 4 → 7 transitions in the ΓKL and ΓKWX planes.
Fig.14	Energy contours for 3 → 7 transitions in the ΓKl and ΓKWX planes.
Fig.15	The real part of the dielectric function as a function of energy.
Fig.16	The reflectivity as a function of energy.
Fig.17	The imaginary part of the reciprocal of the dielectric function as a function of energy.

NaCl

Fig. 18 Electronic energy band structure of NaCl.

Fig. 19 Theoretical ϵ_2 with constant matrix elements.

Fig. 20 Theoretical ϵ_2 with matrix elements computed using pseudopotential wavefunctions.

Fig. 21 Energy contours for 4 → 5 transitions in the ΓKL and ΓKWX planes.

Fig. 22 Energy contours for 4 → 6 transitions in the ΓKL and ΓKWX planes.

Fig. 23 Energy contours for 4 → 7 transitions in the ΓKL and ΓKWX planes.

Fig. 24 Energy contours for 3 → 5 transitions in the ΓKL and ΓKWX planes.

Fig. 25 Energy contours for 3 → 6 transitions in the ΓKL and ΓKWX planes.

Fig. 26 Energy contours for 3 → 7 transitions in the ΓKL and ΓKWX planes.

Fig. 27 Energy contours for 2 → 5 transitions in the ΓKL and ΓKWX planes.

Fig. 28 Energy contours for 2 → 6 transitions in the ΓKL and ΓKWX planes.

Fig. 29 Energy contours for 2 → 7 transitions in the ΓKL and ΓKWX planes.

KCl

Fig. 30 Electronic energy band structure of KCl.

Fig. 31 Theoretical ϵ_2 with constant matrix elements.

Fig. 32 Theoretical ϵ_2 with matrix elements computed using pseudopotential wavefunctions.

Fig. 33 Energy contours for 4 → 5 transitions in the ΓKL and ΓKWX planes.

Fig. 34 Energy contours for 4 → 6 transitions in the ΓKL and ΓKWX planes.

Fig. 35 Energy contours for 4 → 7 transitions in the ΓKL and ΓKWX planes.

Fig. 36 Energy contours for 3 → 5 transitions in the ΓKL and ΓKWX planes.

Fig. 37 Energy contours for 3 → 6 transitions in the ΓKL and ΓKWX planes.

Fig. 38 Energy contours for 3 → 7 transitions in the ΓKL and ΓKWX planes.

Fig. 39 Energy contours for 2 → 5 transitions in the ΓKL and ΓKWX planes.

Fig. 40 Energy contours for 2 → 6 transitions in the ΓKL and ΓKWX planes.

Fig. 41 Energy contours for 2 → 7 transitions in the ΓKL and ΓKWX planes.

Fig. 42 Comparison of two Cl potentials extrapolated from the results of NaCl and KCl. $|\underline{G}|^2$ is in units of $(2\pi/a_{KCl})^2$.

Appendix:

Fig. A1 Geometry of the angles used in evaluating the $\ell = 2$ nonlocal pseudopotential.

TABLE CAPTIONS

Table I	A comparison of MgO form factors (in rydbergs) used in the present work with those used in reference 14.
Table II	Identification of prominent optical structure of MgO and comparison of the energies (in eV's) between the calculated and measured ϵ_2.
Table III	Calculated critical point energies, associated band transitions and critical point symmetries of MgO.
Table IV	A comparison of NaCl symmetric form factors (in rydbergs) used in the calculation with those scaled from Si.
Table V	The antisymmetric form factors of NaCl used in the present calculation.
Table VI	Identification of prominent optical structure of NaCl and comparison of the energies (in eV's) between the calculated and measured ϵ_2.
Table VII	Calculated critical points energies, associated band transitions and critical point symmetries of NaCl.
Table VIII	Form factors of KCl (in rydbergs) used with the scaled values for the symmetric part of the form factors.
Table IX	Identification of prominent optical structure of KCl and comparison of the energies (in eV's) between the calculated and measured ϵ_2.
Table X	Calculated critical points energies, associated band transitions and critical point symmetries of KCl.

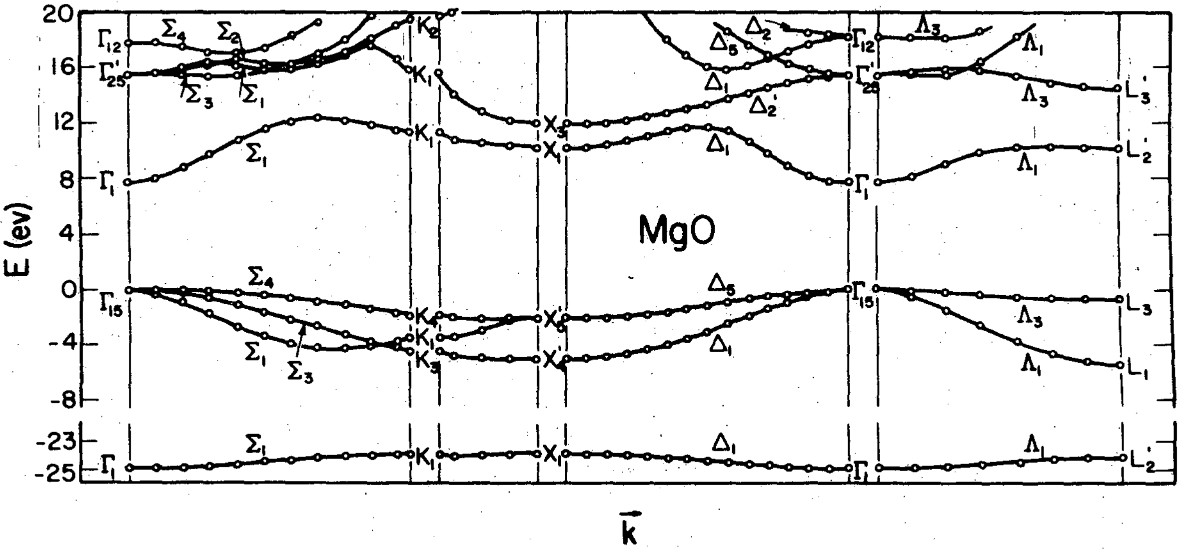

E (ev)
20
16
12
8
4
0
-4
-8
-23
-25
MgO
k
Γ12
Γ25'
Γ1
Γ15
Σ4
Σ2
Σ3
Σ1
K2
K1
K3
X3
X1
X5'
X4'
Δ5
Δ2
Δ1
Δ2'
Γ12
Γ25'
Γ1
Γ15
Λ3
Λ1
L3'
L2'
L3
L1
L2'

Fig. 1

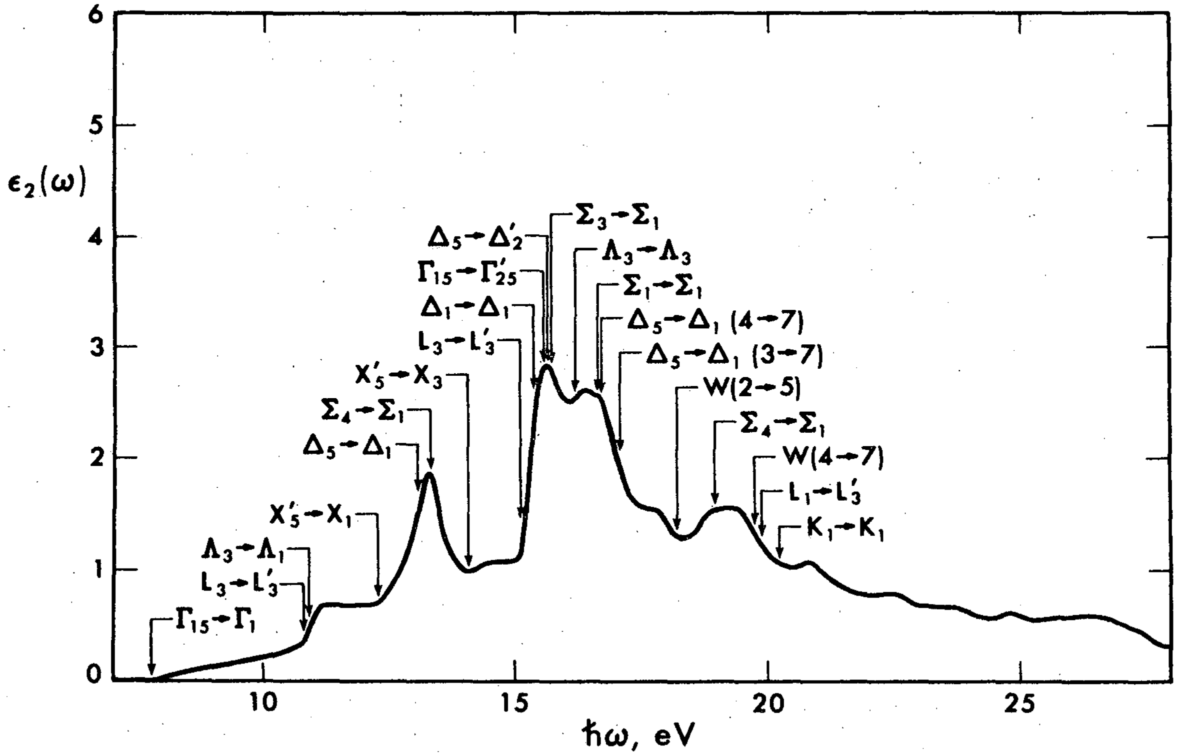

$\epsilon_2(\omega)$
0
1
2
3
4
5
6
10
15
20
25
$\hbar\omega$, eV
$\Gamma_{15} \to \Gamma_1$
$L_3 \to L_3'$
$\Lambda_3 \to \Lambda_1$
$X_5' \to X_1$
$\Delta_5 \to \Delta_1$
$\Sigma_4 \to \Sigma_1$
$X_5' \to X_3$
$L_3 \to L_3'$
$\Delta_1 \to \Delta_1$
$\Gamma_{15} \to \Gamma_{25}'$
$\Delta_5 \to \Delta_2'$
$\Sigma_3 \to \Sigma_1$
$\Lambda_3 \to \Lambda_3$
$\Sigma_1 \to \Sigma_1$
$\Delta_5 \to \Delta_1$ (4→7)
$\Delta_5 \to \Delta_1$ (3→7)
W(2→5)
$\Sigma_4 \to \Sigma_1$
W(4→7)
$L_1 \to L_3'$
$K_1 \to K_1$

Fig. 2

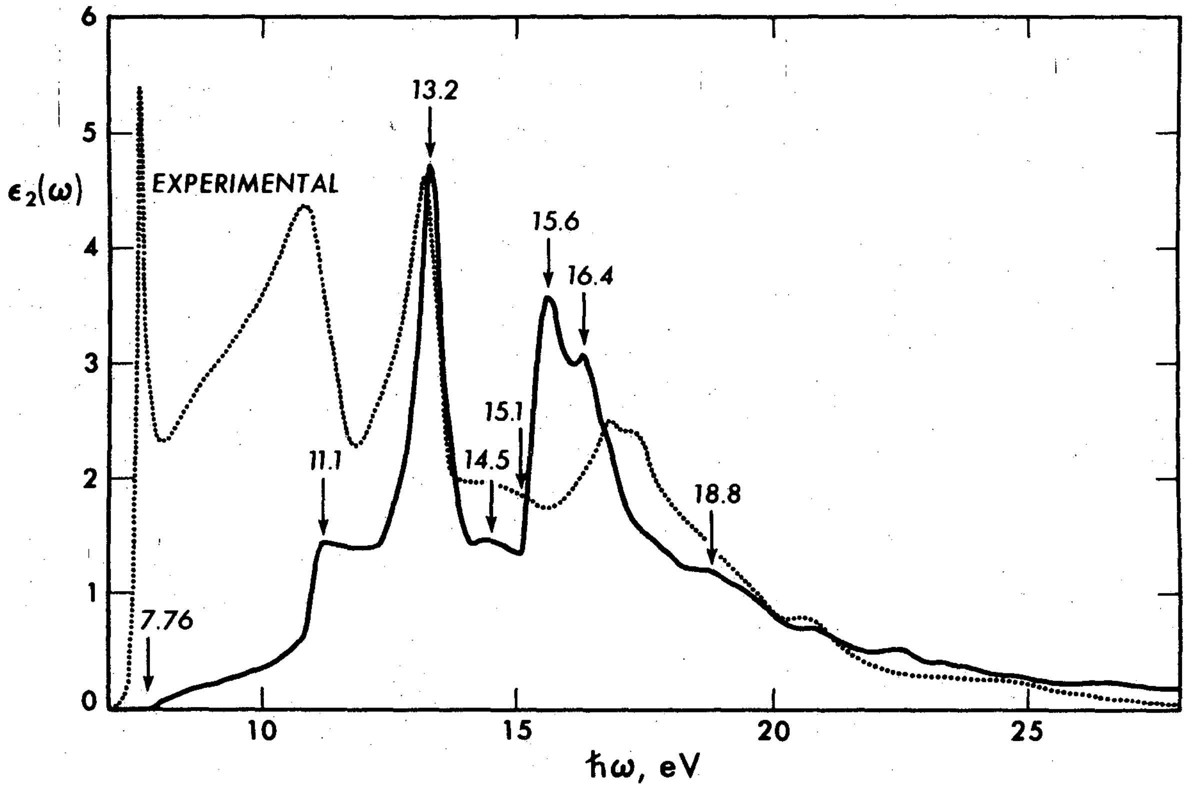
6
5
4
3
2
1
0
$\epsilon_2(\omega)$
EXPERIMENTAL
13.2
15.6
16.4
15.1
14.5
11.1
18.8
7.76
10
15
20
25
$\hbar\omega$, eV

Fig. 3

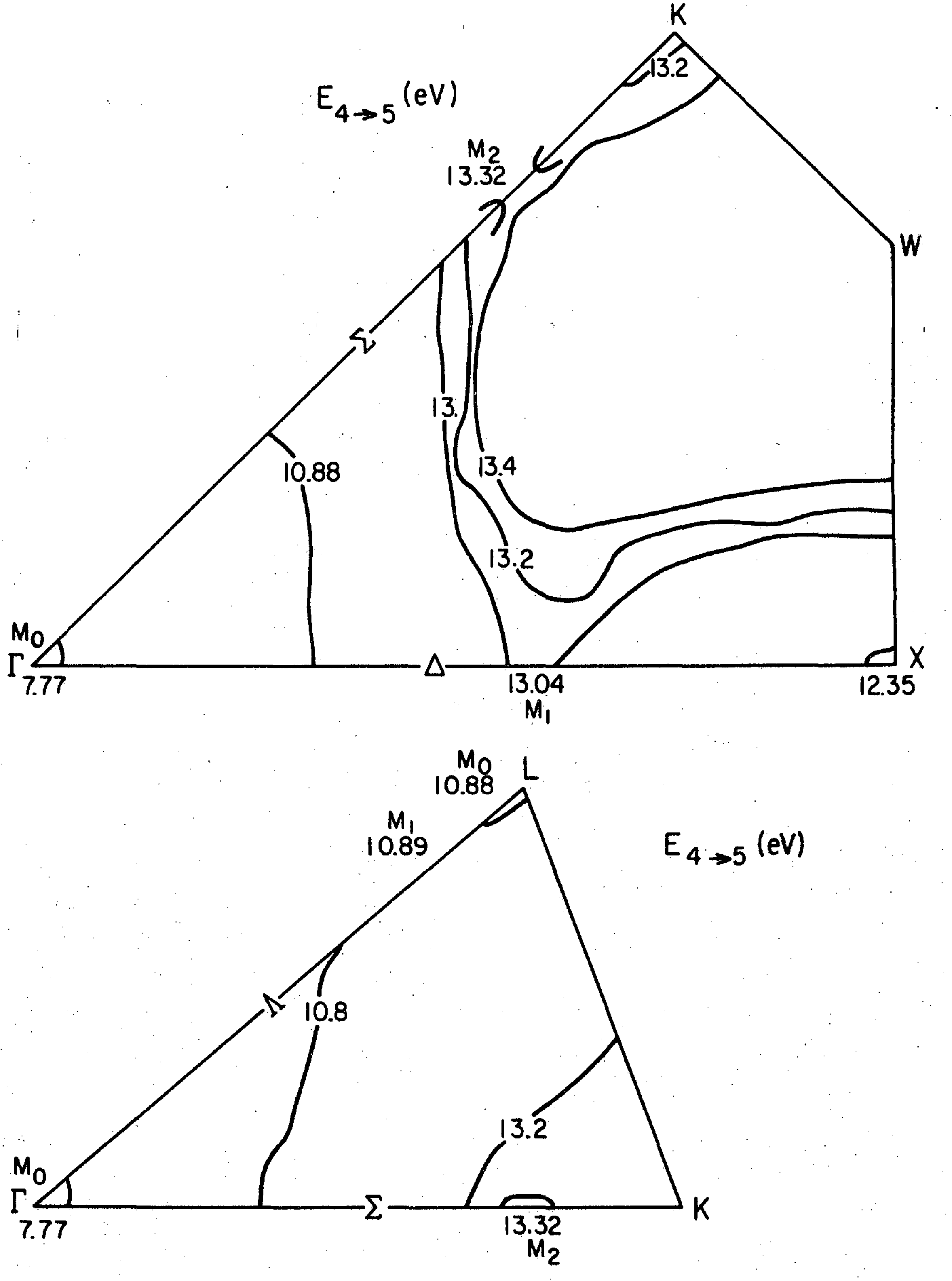
K
13.2
$E_{4\rightarrow5}$ (eV)
M2
13.32
W
Σ
13.
13.4
10.88
13.2
M0
Γ
7.77
Δ
13.04
M1
X
12.35
M0
10.88
L
M1
10.89
$E_{4\rightarrow5}$ (eV)
Λ
10.8
13.2
M0
Γ
7.77
Σ
13.32
M2
K

Fig. 4

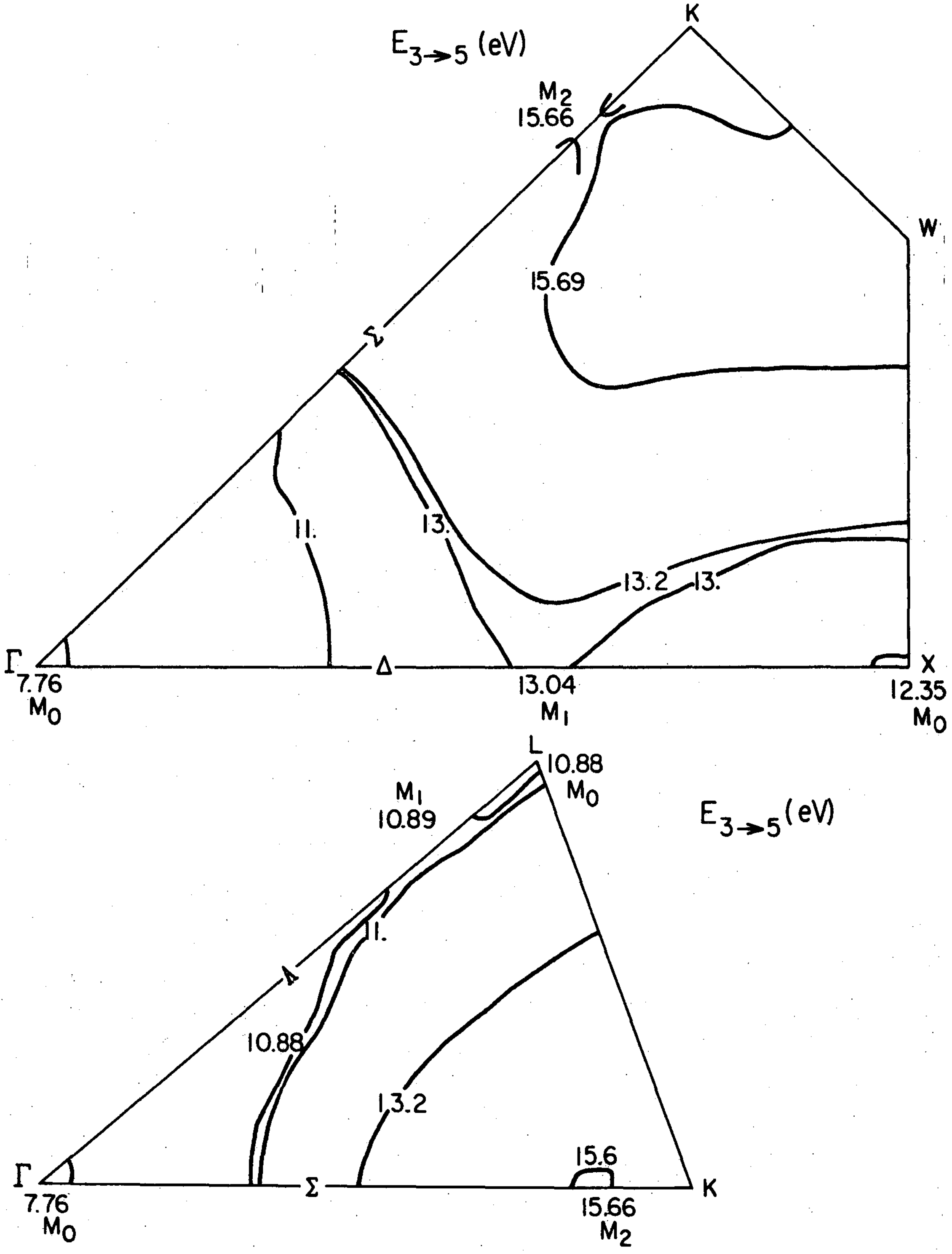
$E_{3\to5}$ (eV)
K
M_2
15.66
W
15.69
Σ
11.
13.
13.2
13.
Γ
7.76
M_0
Δ
13.04
M_1
X
12.35
M_0
L
10.88
M_0
M_1
10.89
$E_{3\to5}$(eV)
11.
Λ
10.88
13.2
15.6
Γ
7.76
M_0
Σ
15.66
M_2
K

Fig. 5

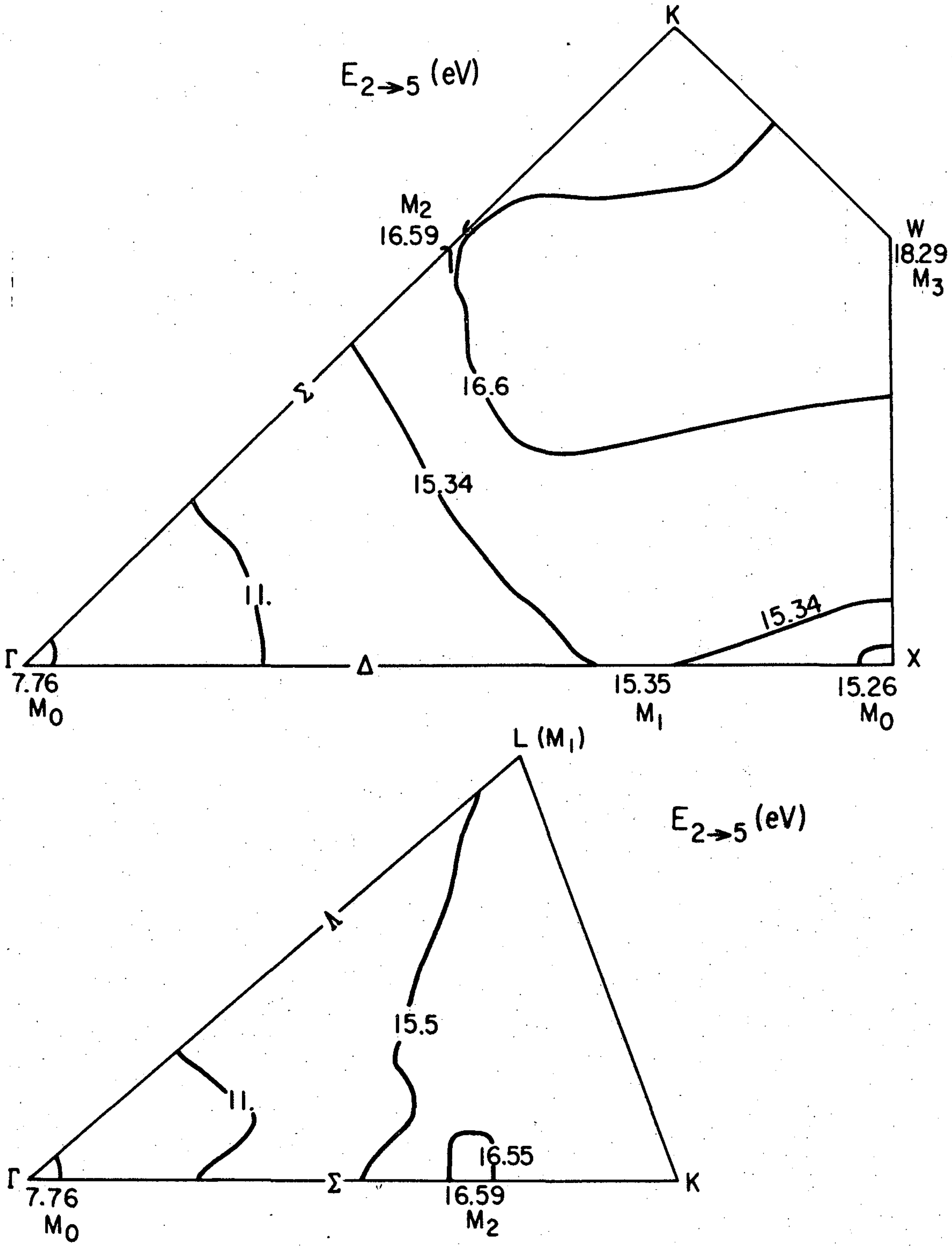
$E_{2\to5}$ (eV)
K
M_2
16.59
W
18.29
M_3
Σ
16.6
15.34
11.
15.34
Γ
7.76
M_0
Δ
15.35
M_1
X
15.26
M_0
L (M_1)
$E_{2\to5}$ (eV)
Λ
15.5
11.
16.55
Γ
7.76
M_0
Σ
16.59
M_2
K

Fig. 6

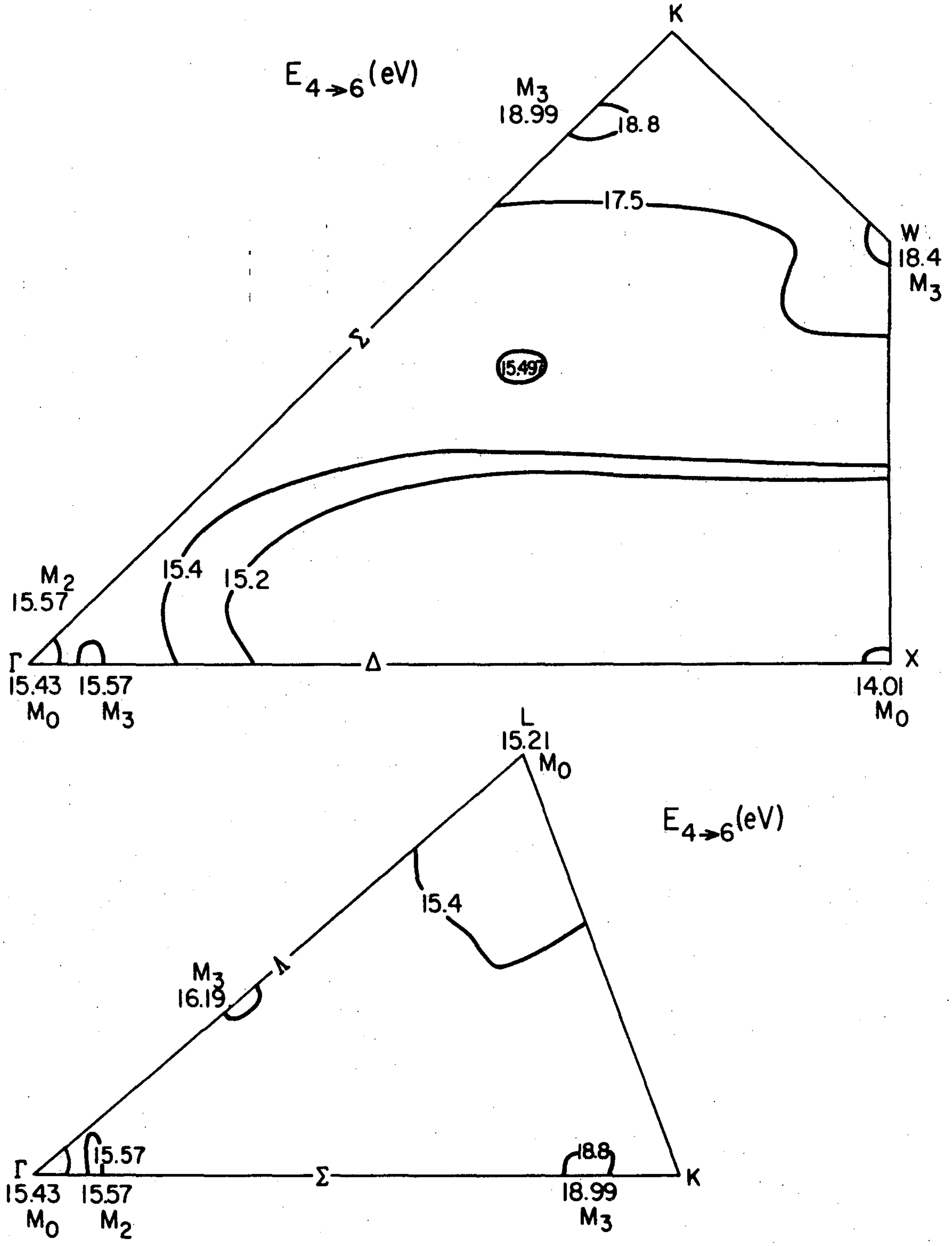
$E_{4\to6}$(eV)
K
M_3
18.99
18.8
17.5
W
18.4
M_3
Σ
15.497
M_2
15.57
15.4
15.2
Γ
Δ
X
15.43
M_0
15.57
M_3
14.01
M_0
L
15.21
M_0
$E_{4\to6}$(eV)
15.4
M_3
16.19
Λ
Γ
15.57
Σ
18.8
K
15.43
M_0
15.57
M_2
18.99
M_3

Fig. 7

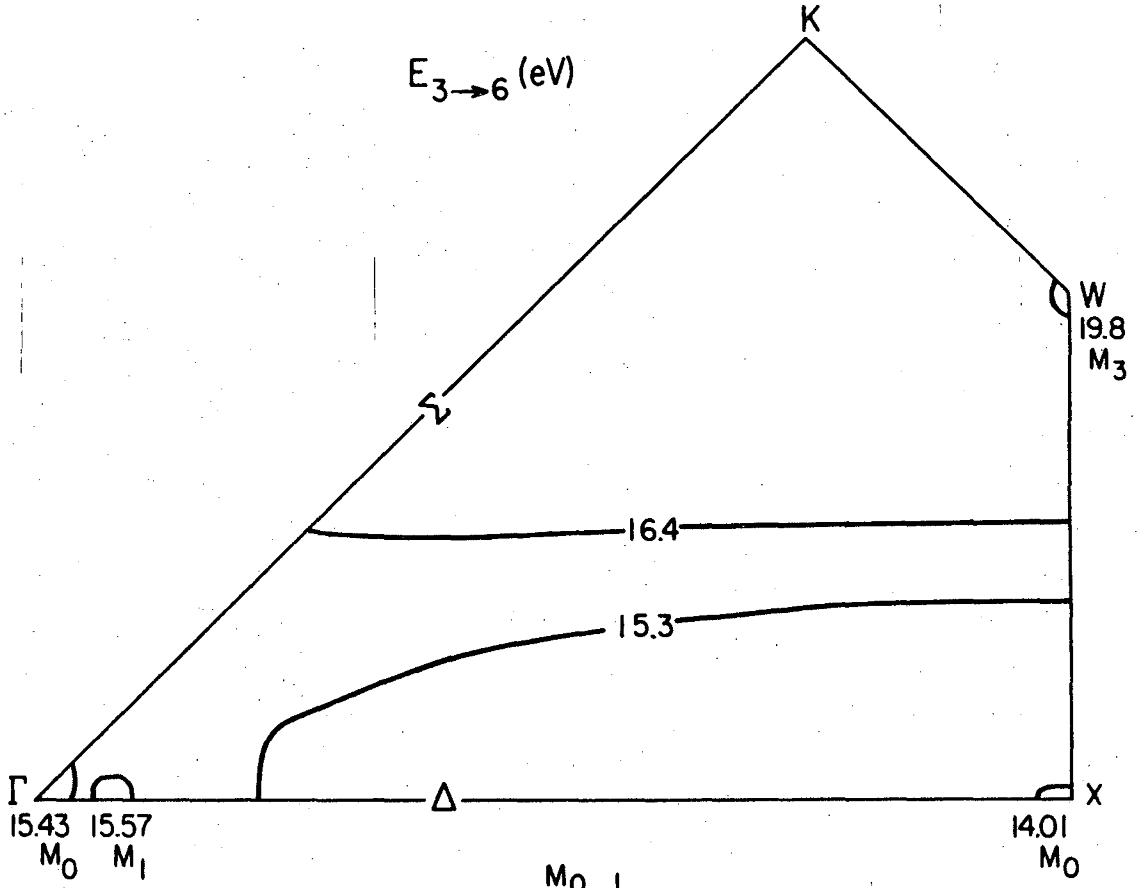
K
$E_{3\to6}$ (eV)
W
19.8
M_3
Σ
16.4
15.3
Γ
15.43
M_0
15.57
M_1
Δ
X
14.01
M_0

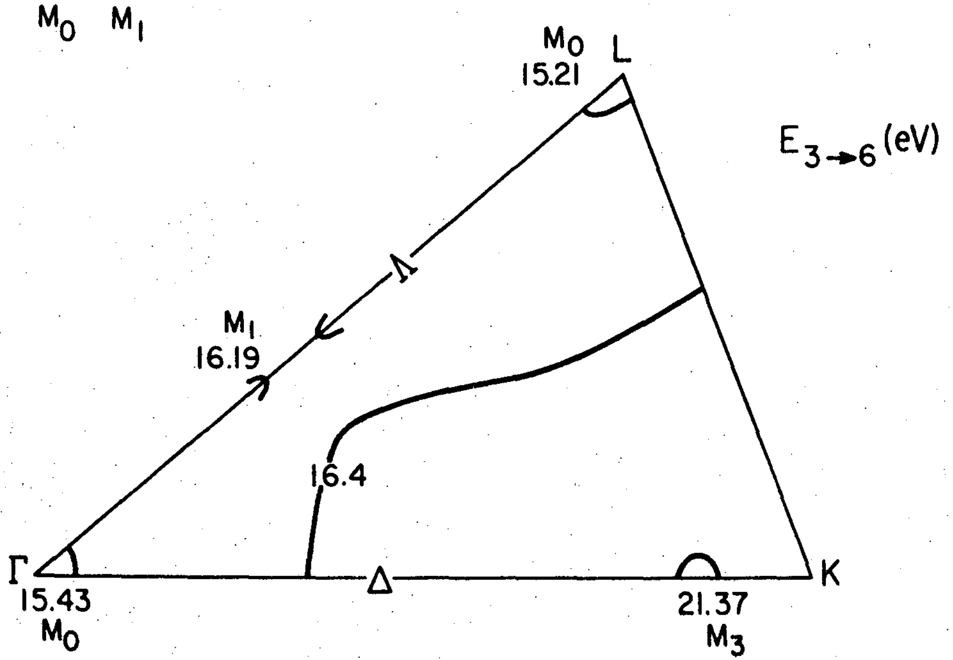
M_0
15.21
L
$E_{3\to6}$ (eV)
Λ
M_1
16.19
16.4
Γ
15.43
M_0
Δ
21.37
M_3
K

Fig. 8

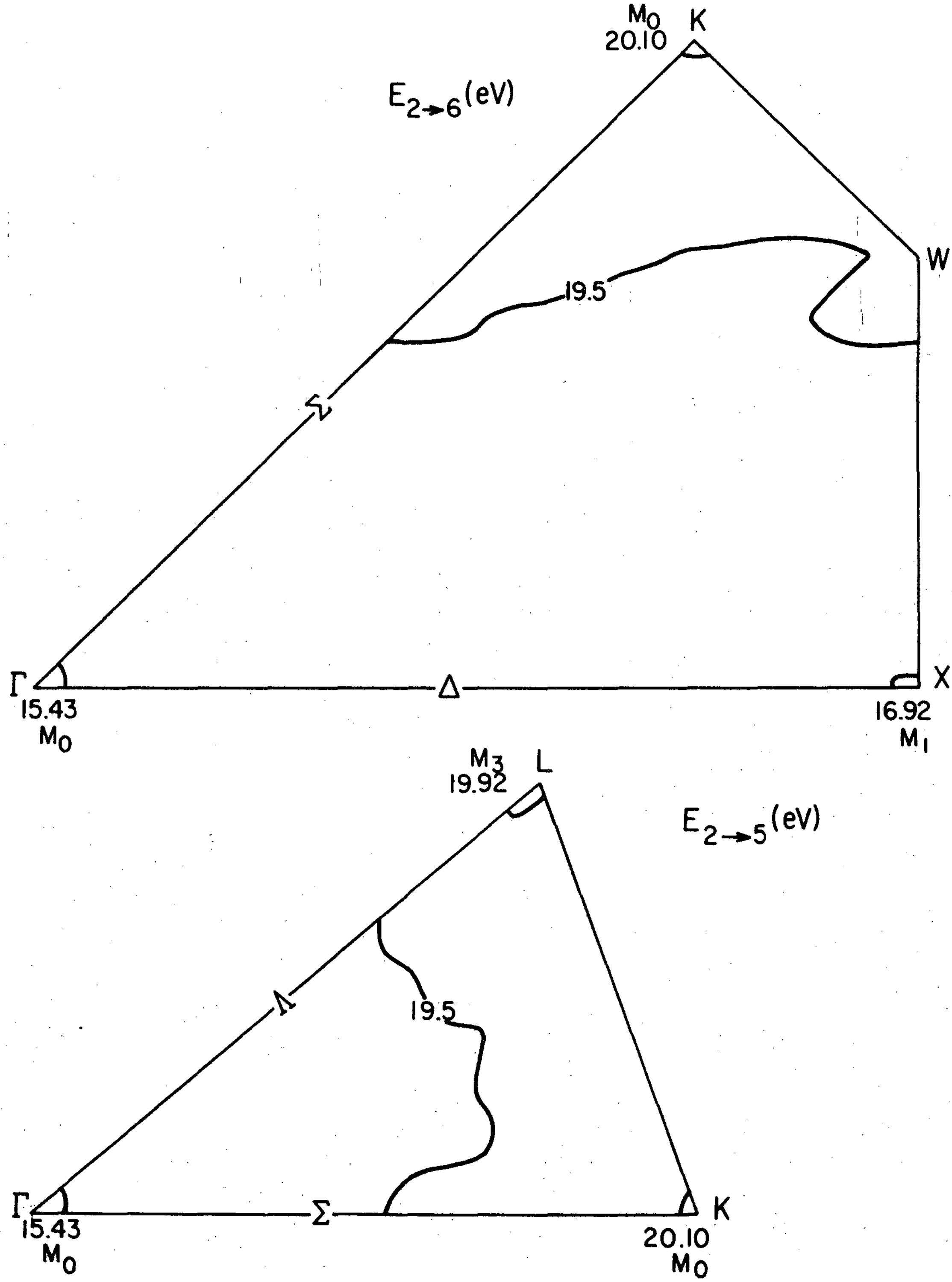

$E_{2\to6}$(eV)
M_0
20.10
K
W
19.5
Σ
Γ
15.43
M_0
Δ
X
16.92
M_1
M_3
19.92
L
$E_{2\to5}$(eV)
Λ
19.5
Γ
15.43
M_0
Σ
K
20.10
M_0

Fig. 9

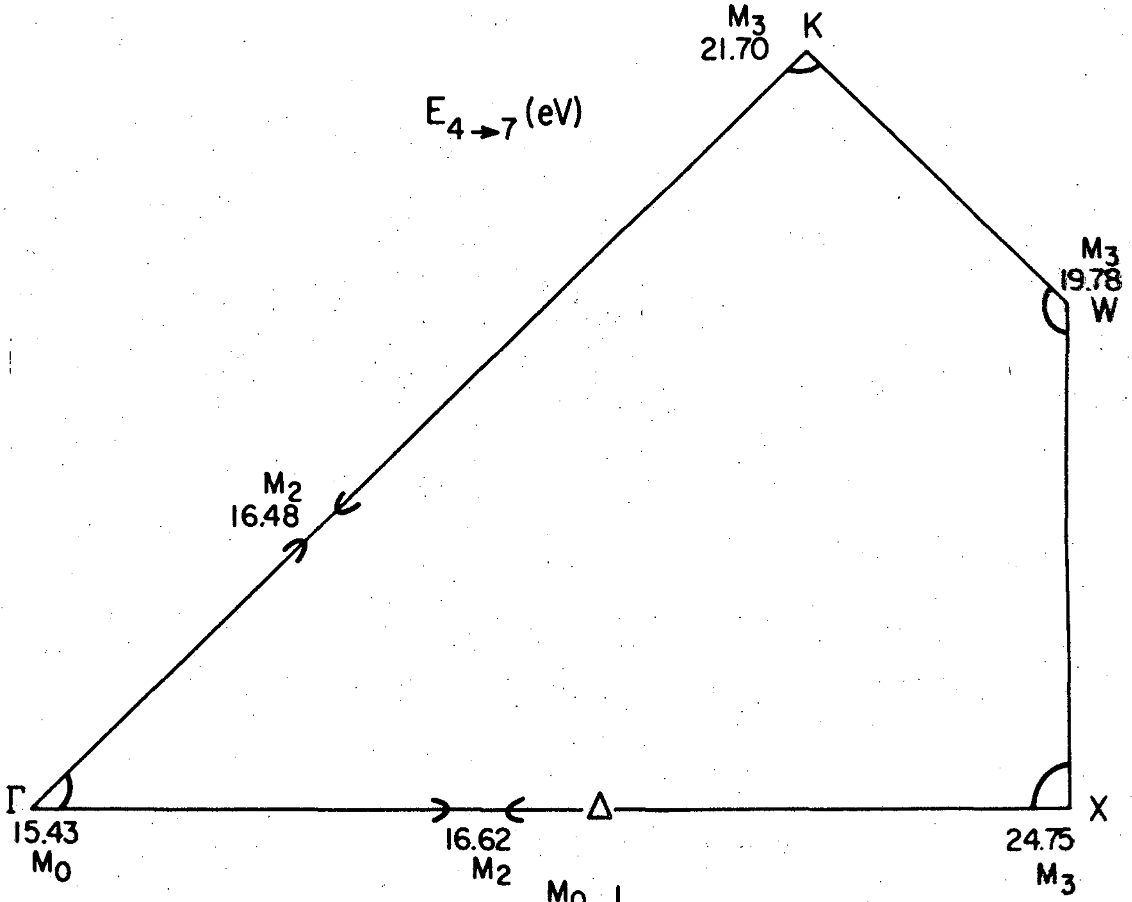
$E_{4\to7}$ (eV)
M_3
21.70
K
M_3
19.78
W
M_2
16.48
Γ
15.43
M_0
16.62
M_2
Δ
X
24.75
M_3

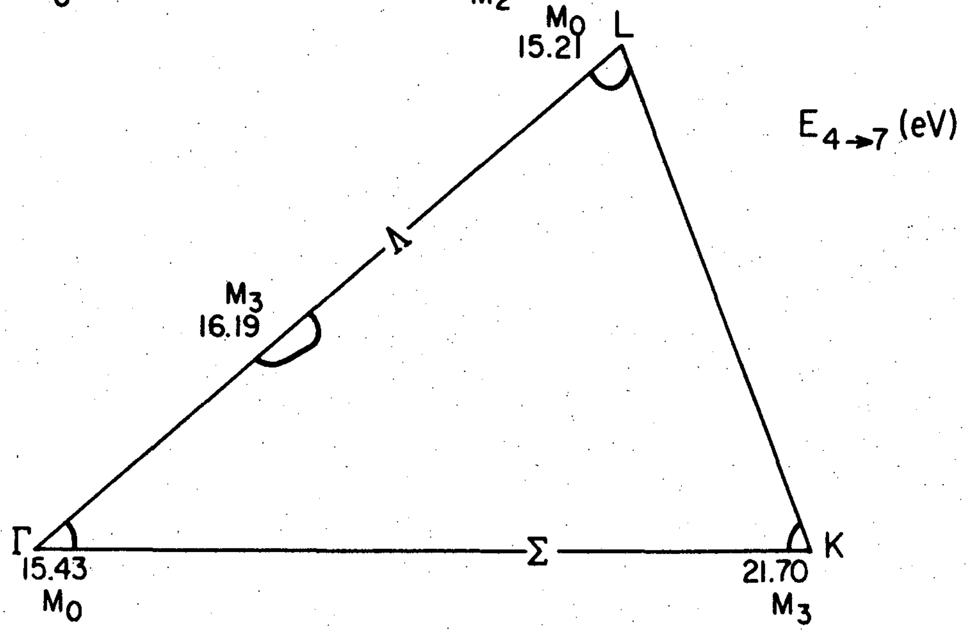
M_0
15.21
L
$E_{4\to7}$ (eV)
Λ
M_3
16.19
Γ
15.43
M_0
Σ
K
21.70
M_3

Fig. 10

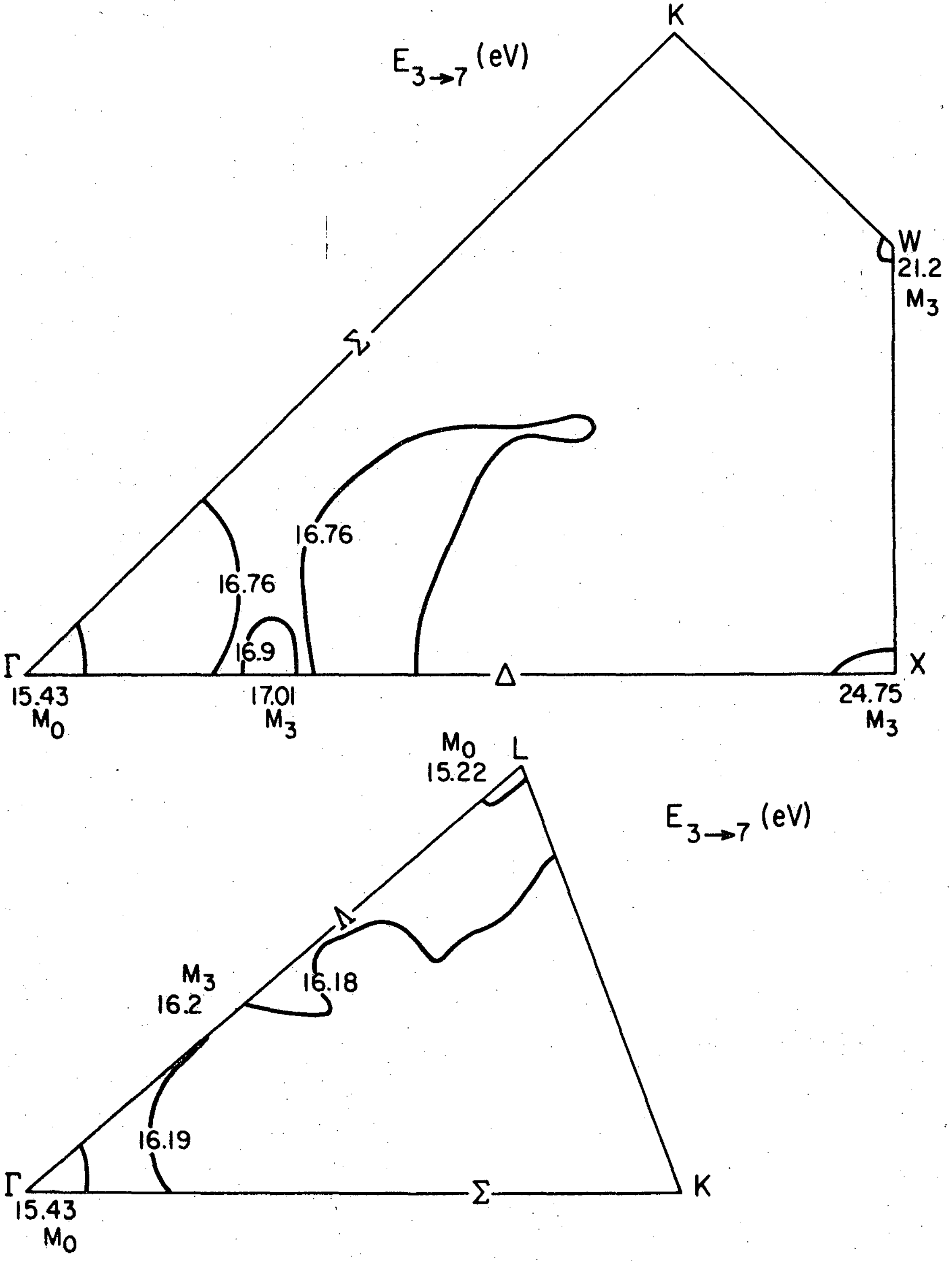
K
$E_{3\rightarrow7}$ (eV)
W
21.2
M_3
Σ
16.76
16.76
16.9
Γ
15.43
M_0
17.01
M_3
Δ
X
24.75
M_3
M_0
15.22
L
$E_{3\rightarrow7}$ (eV)
Λ
M_3
16.2
16.18
16.19
Γ
15.43
M_0
Σ
K

Fig. 11

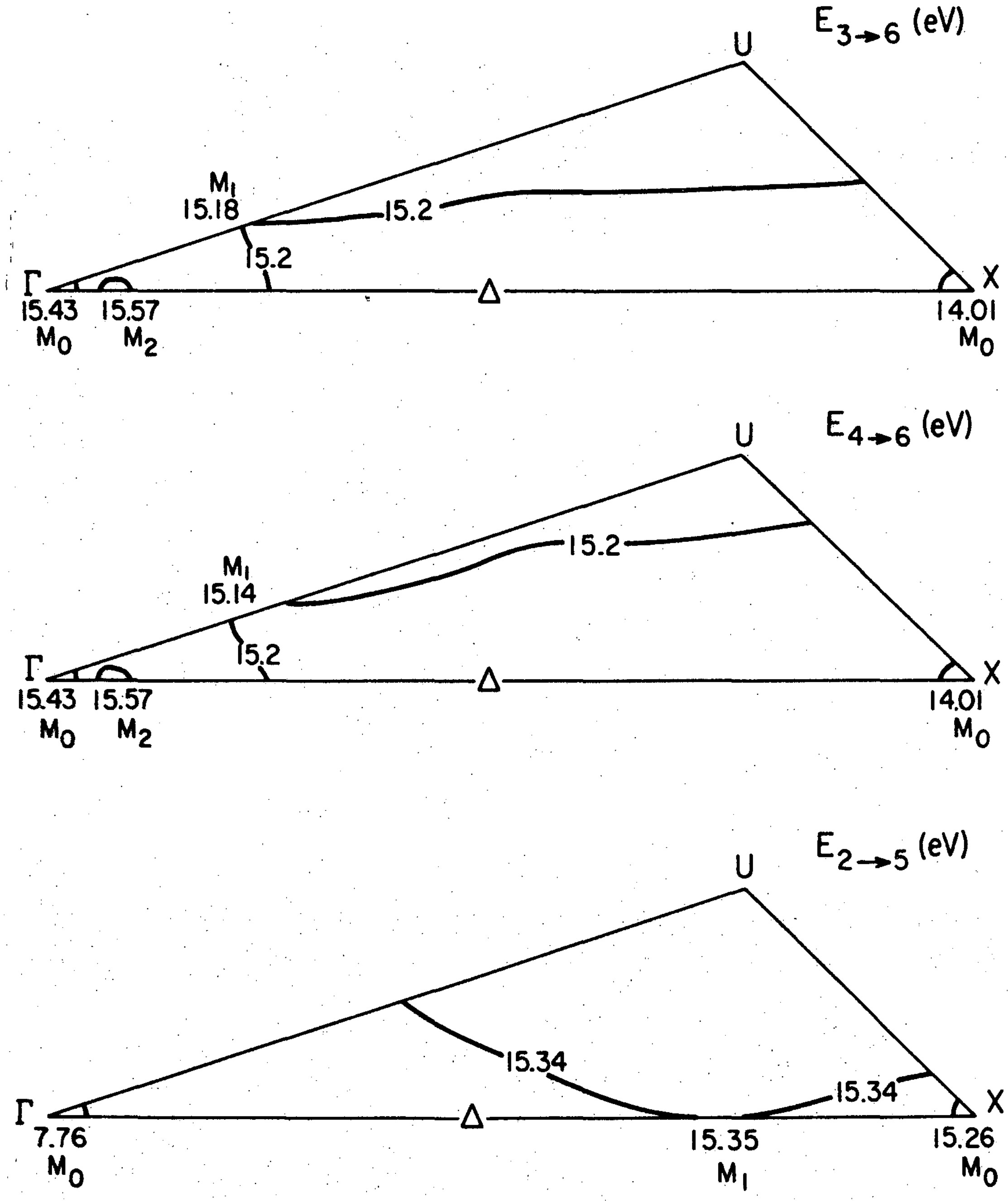
$E_{3\to6}$ (eV)
U
M_1
15.18
15.2
15.2
Γ
15.43
M_0
15.57
M_2
Δ
X
14.01
M_0
$E_{4\to6}$ (eV)
U
M_1
15.14
15.2
15.2
Γ
15.43
M_0
15.57
M_2
Δ
X
14.01
M_0
$E_{2\to5}$ (eV)
U
15.34
15.34
Γ
7.76
M_0
Δ
15.35
M_1
X
15.26
M_0

Fig. 12

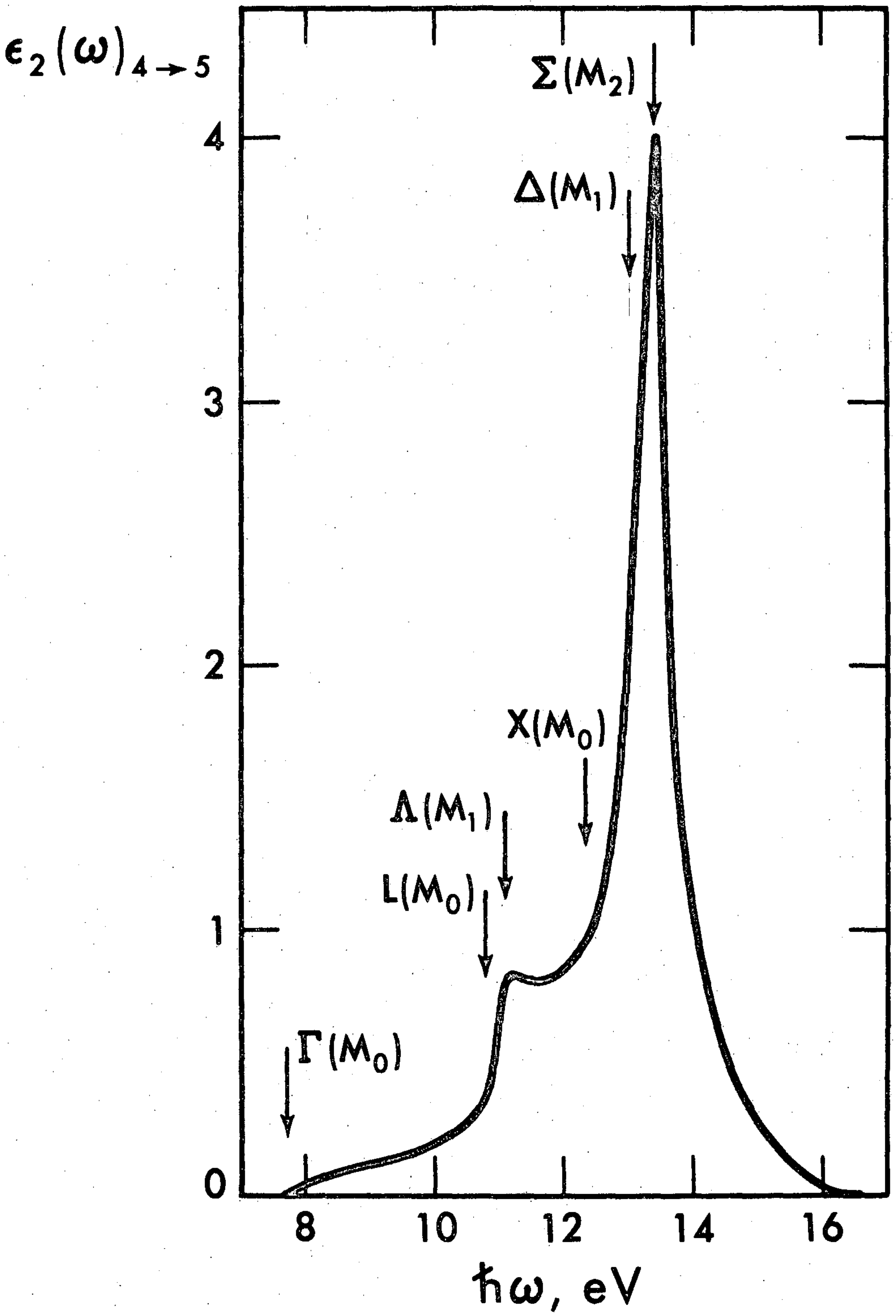
$\epsilon_2(\omega)_{4\rightarrow5}$
$\Sigma(M_2)$
$\Delta(M_1)$
$X(M_0)$
$\Lambda(M_1)$
$L(M_0)$
$\Gamma(M_0)$
0
1
2
3
4
8
10
12
14
16
$\hbar\omega$, eV

Fig. 13

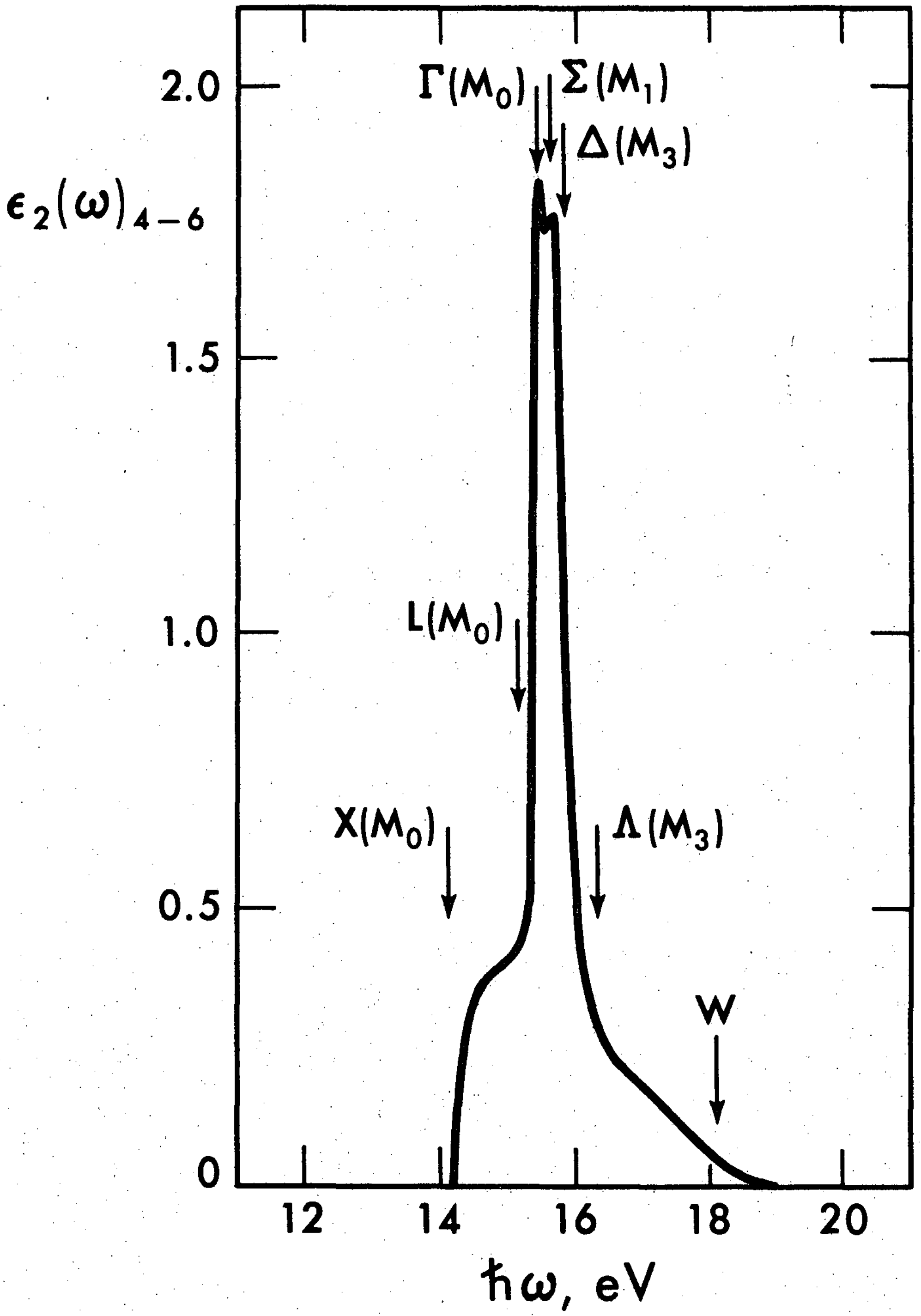

$\epsilon_2(\omega)_{4-6}$
2.0
1.5
1.0
0.5
0
12
14
16
18
20
$\hbar\omega$, eV
$\Gamma(M_0)$
$\Sigma(M_1)$
$\Delta(M_3)$
$L(M_0)$
$X(M_0)$
$\Lambda(M_3)$
W

Fig. 14

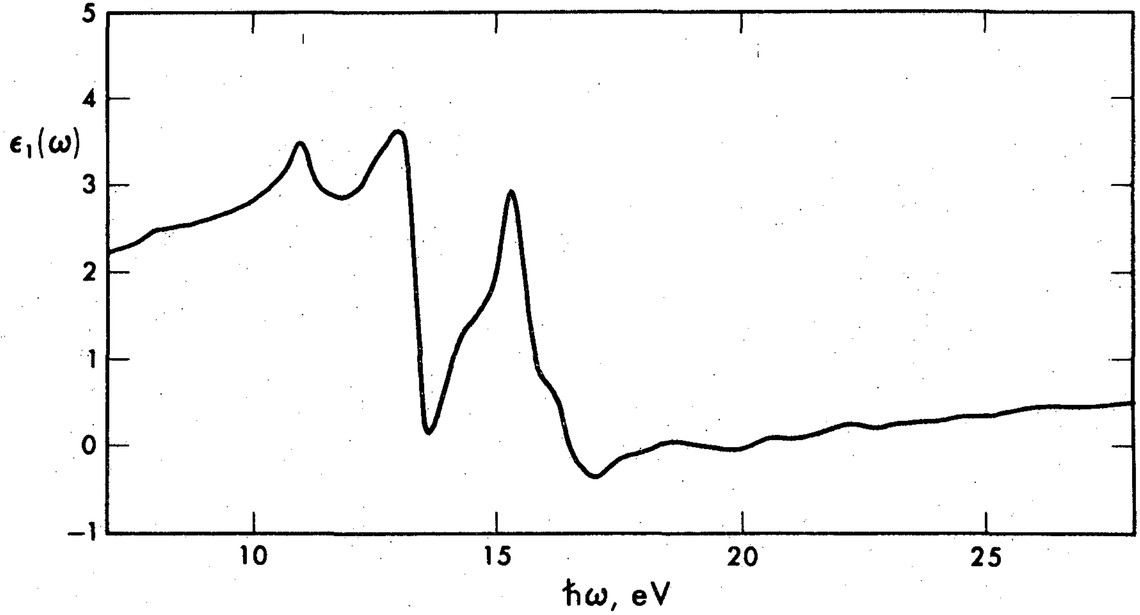

Fig. 15

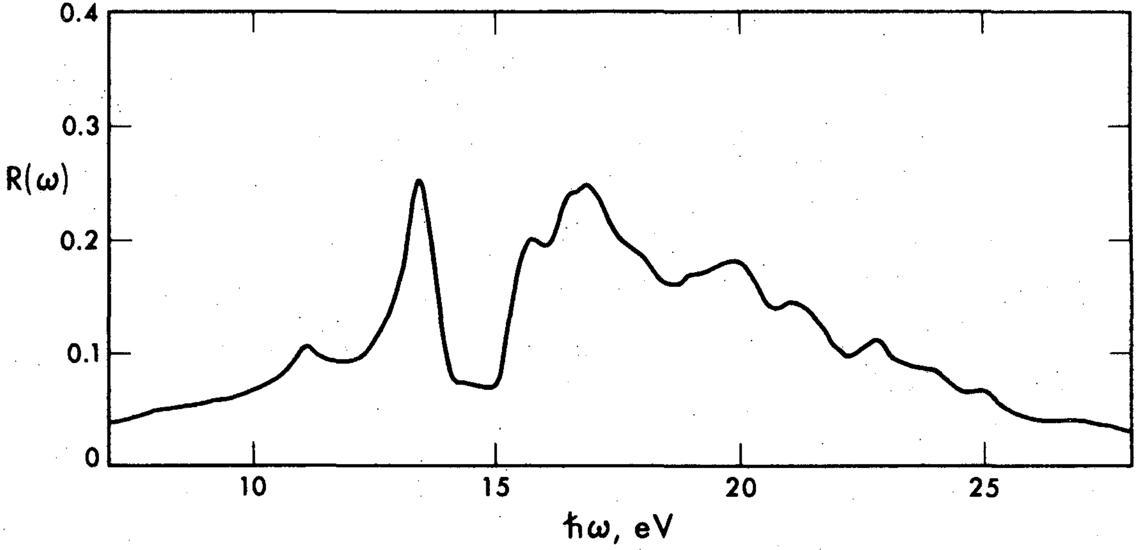

Fig. 16

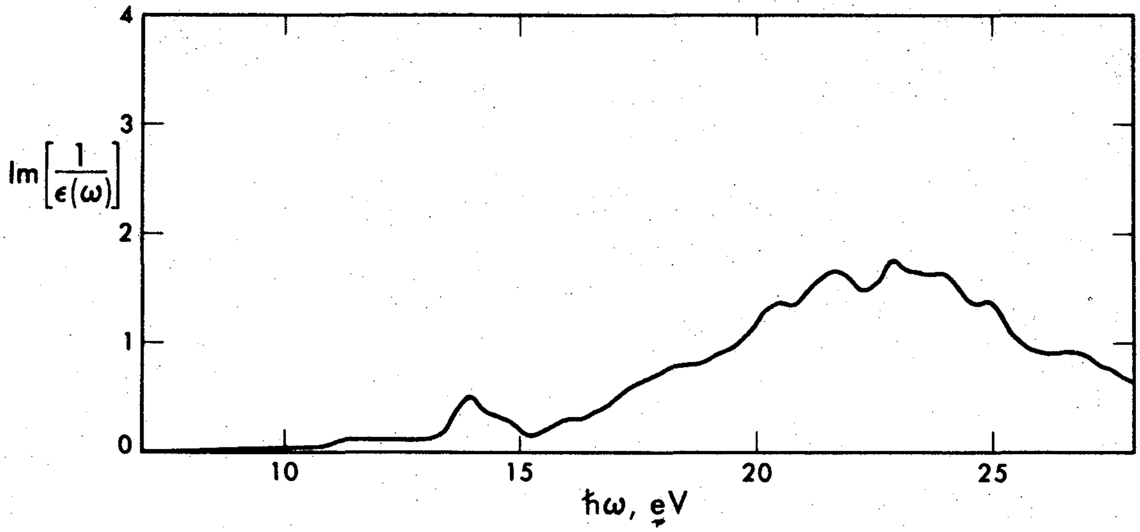
4
3
2
1
0
$\mathrm{Im}\left[\frac{1}{\epsilon(\omega)}\right]$
10
15
20
25
$\hbar\omega$, eV

Fig. 17

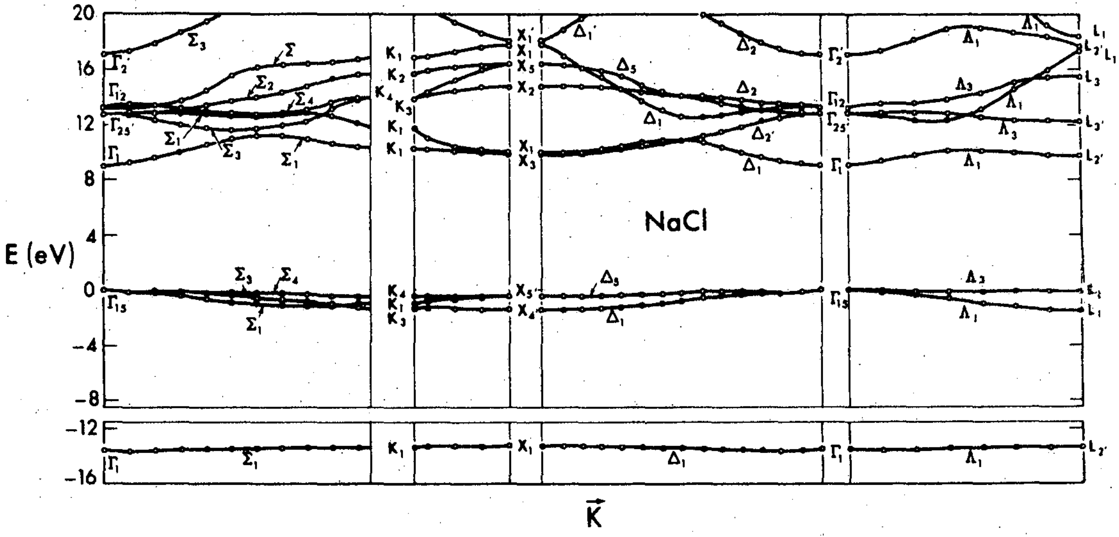
NaCl
E (eV)
20
16
12
8
4
0
−4
−8
−12
−16
$\vec{K}$
Γ_2'
Γ_{12}
$\Gamma_{25'}$
Γ_1
Γ_{15}
K_1
K_2
K_4
K_3
X_1'
X_1
X_5
X_2
X_3
X_5'
X_4
L_1
$L_{2'}$
L_3
$L_{3'}$
Σ_1
Σ_2
Σ_3
Σ_4
Δ_1
Δ_1'
Δ_2
$\Delta_{2'}$
Δ_5
Λ_1
Λ_3

Fig. 18

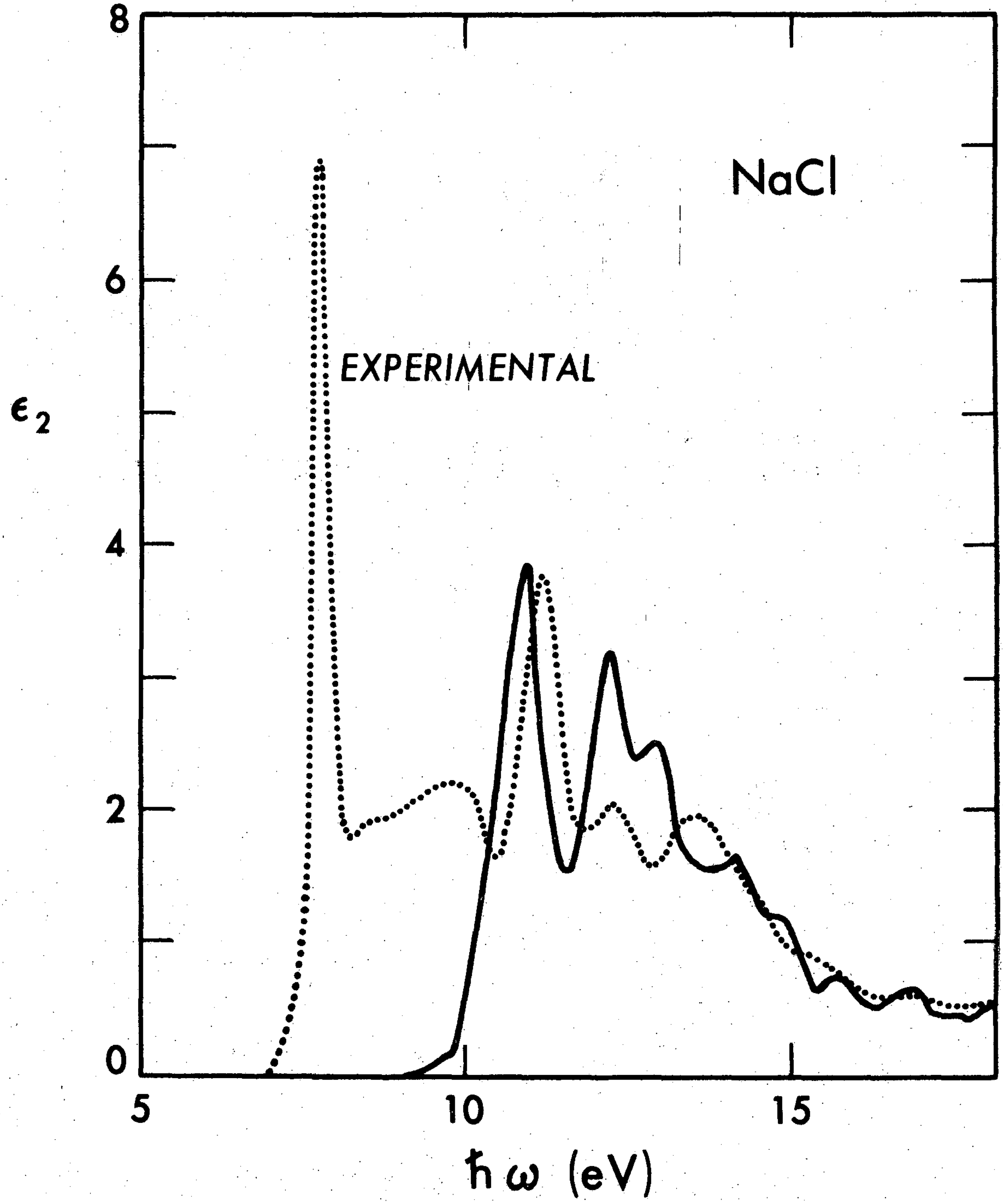

Fig. 19

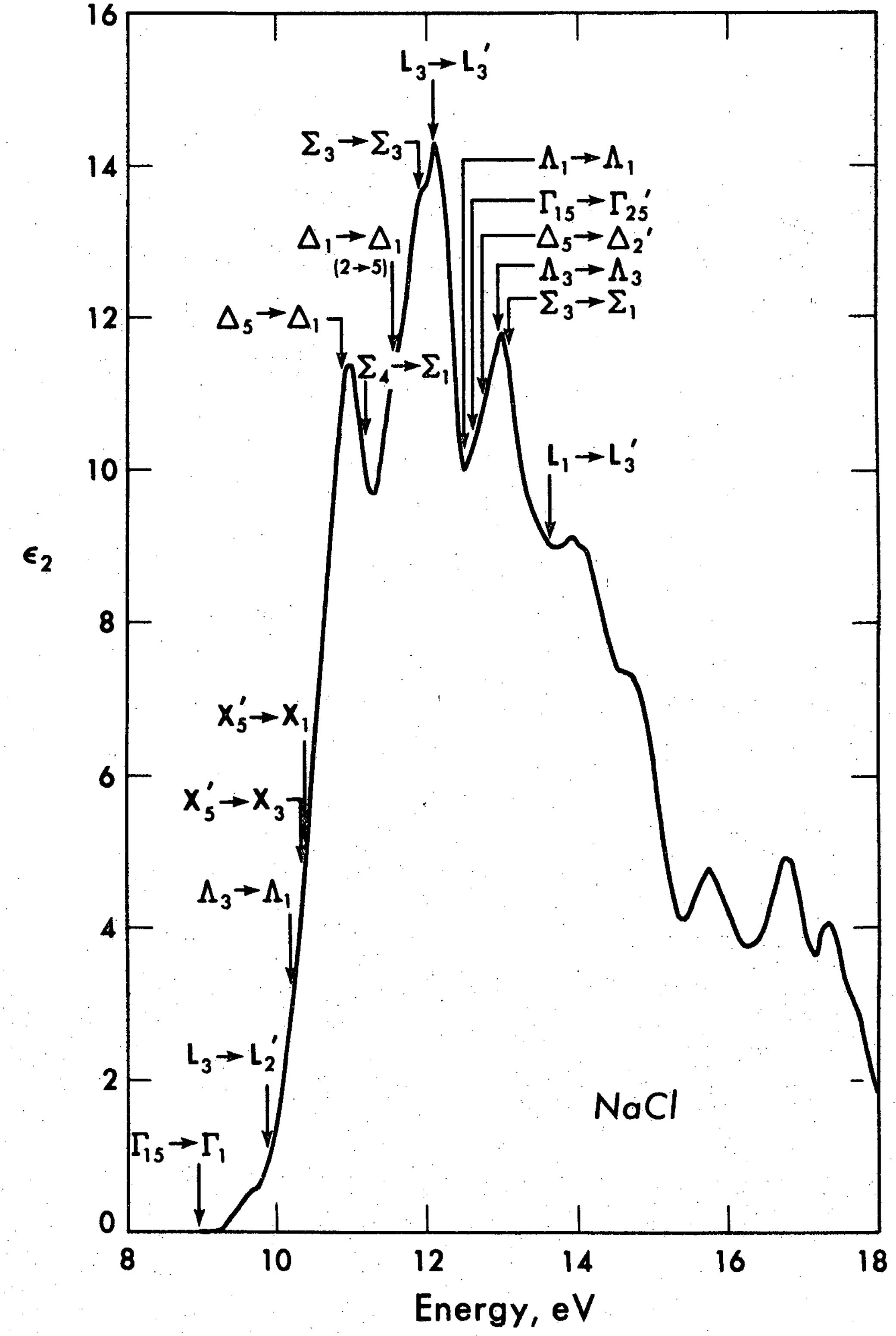

16
14
12
10
8
6
4
2
0
ϵ_2
8
10
12
14
16
18
Energy, eV
NaCl
$L_3 \rightarrow L_3'$
$\Sigma_3 \rightarrow \Sigma_3$
$\Lambda_1 \rightarrow \Lambda_1$
$\Gamma_{15} \rightarrow \Gamma_{25}'$
$\Delta_1 \rightarrow \Delta_1$
(2→5)
$\Delta_5 \rightarrow \Delta_2'$
$\Lambda_3 \rightarrow \Lambda_3$
$\Delta_5 \rightarrow \Delta_1$
$\Sigma_3 \rightarrow \Sigma_1$
$\Sigma_4 \rightarrow \Sigma_1$
$L_1 \rightarrow L_3'$
$X_5' \rightarrow X_1$
$X_5' \rightarrow X_3$
$\Lambda_3 \rightarrow \Lambda_1$
$L_3 \rightarrow L_2'$
$\Gamma_{15} \rightarrow \Gamma_1$

Fig. 20

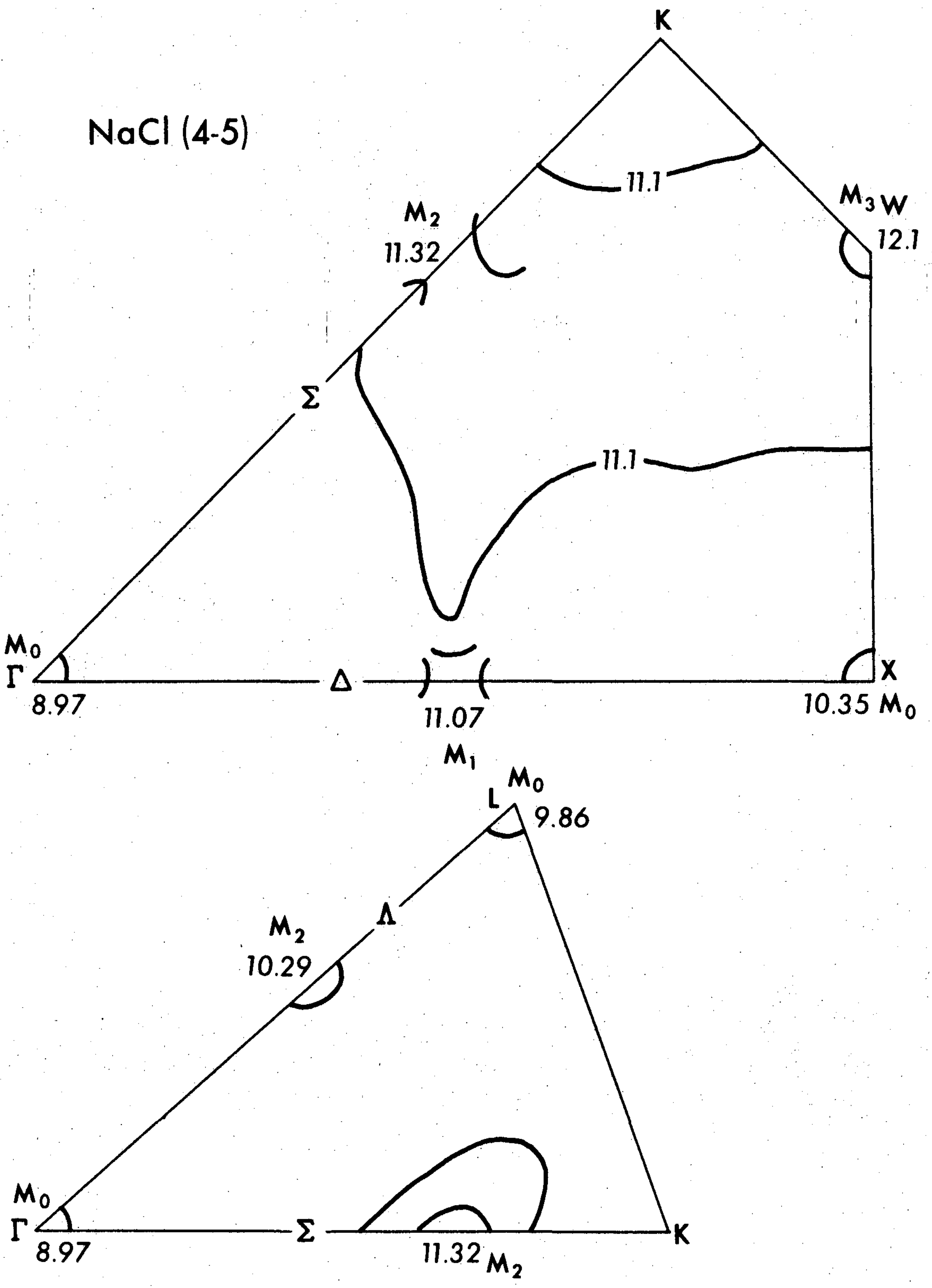
NaCl (4-5)
K
11.1
M₃ W
12.1
M₂
11.32
Σ
11.1
M₀
Γ
8.97
Δ
11.07
M₁
X
10.35 M₀
M₀
L
9.86
M₂
10.29
Λ
M₀
Γ
8.97
Σ
11.32 M₂
K

Fig. 21

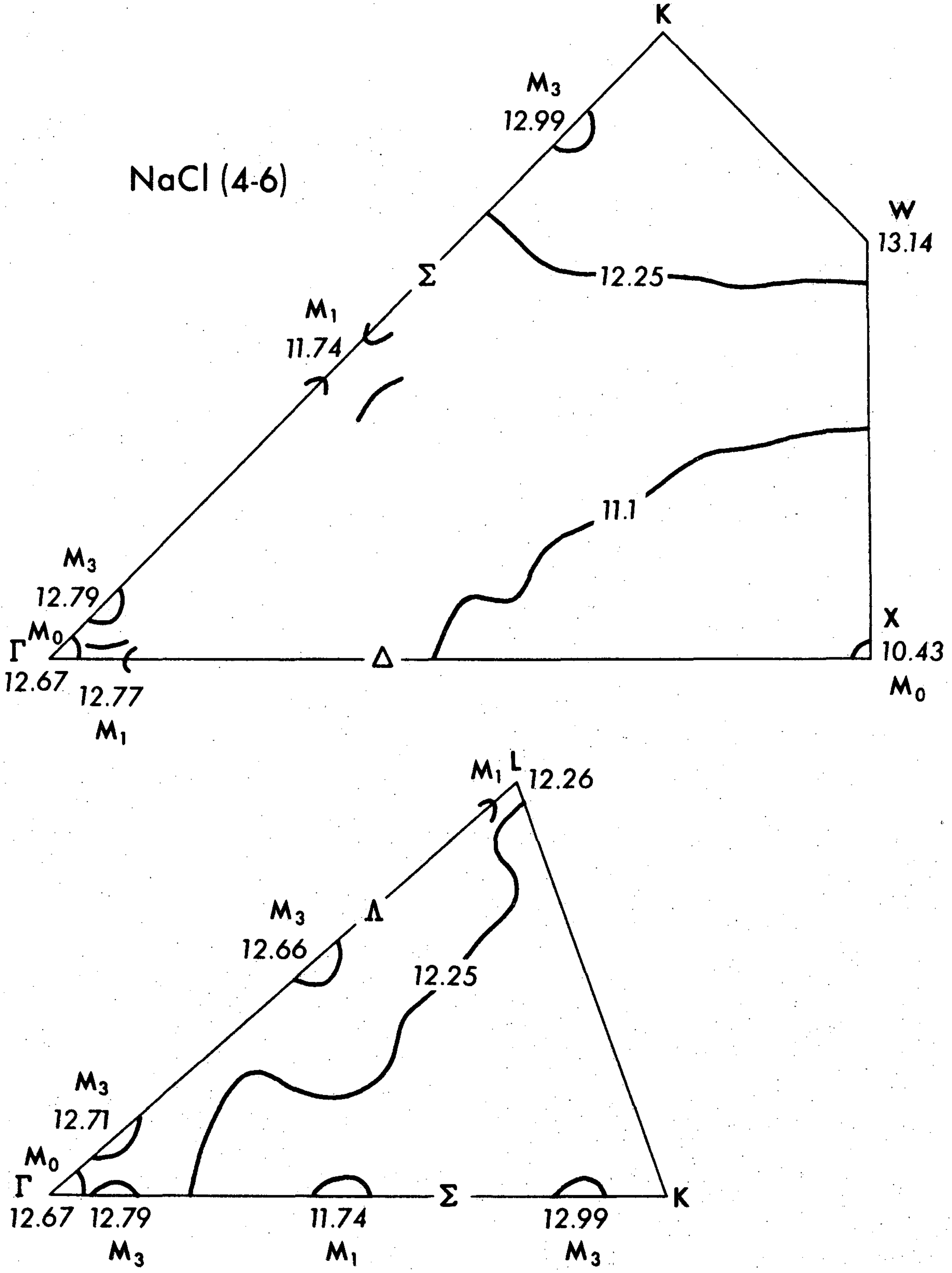
NaCl (4-6)
K
M_3
12.99
W
13.14
Σ
12.25
M_1
11.74
11.1
M_3
12.79
M_0
Γ
12.67
12.77
M_1
Δ
X
10.43
M_0
M_1
L
12.26
M_3
Λ
12.66
12.25
M_3
12.71
M_0
Γ
12.67
12.79
M_3
11.74
M_1
Σ
12.99
M_3
K

Fig. 22

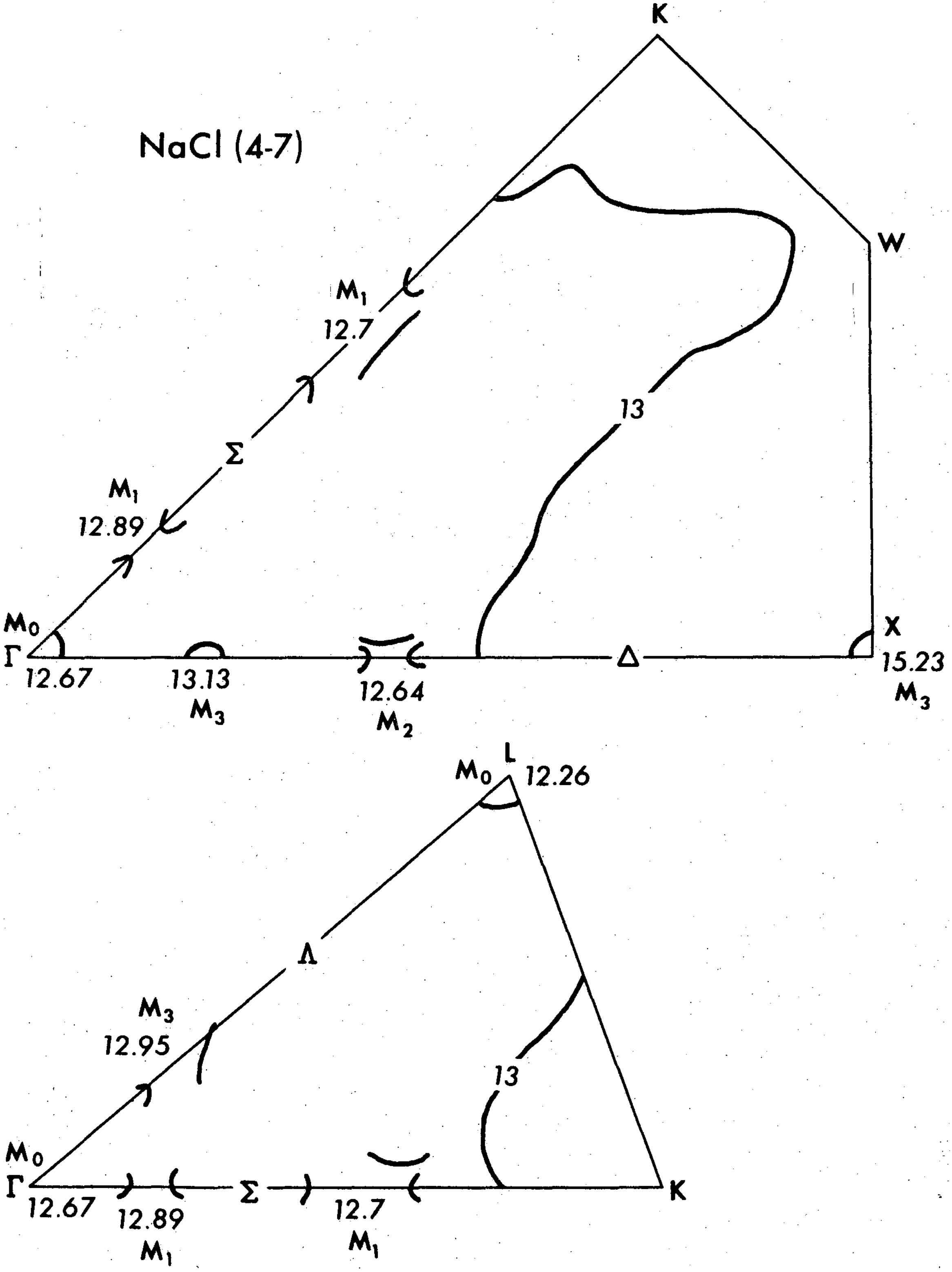
NaCl (4-7)
K
W
X
15.23
M3
Γ
M0
12.67
13.13
M3
12.64
M2
Δ
13
Σ
M1
12.89
M1
12.7
L
M0
12.26
Λ
M3
12.95
13
M0
Γ
12.67
12.89
M1
Σ
12.7
M1
K

Fig. 23

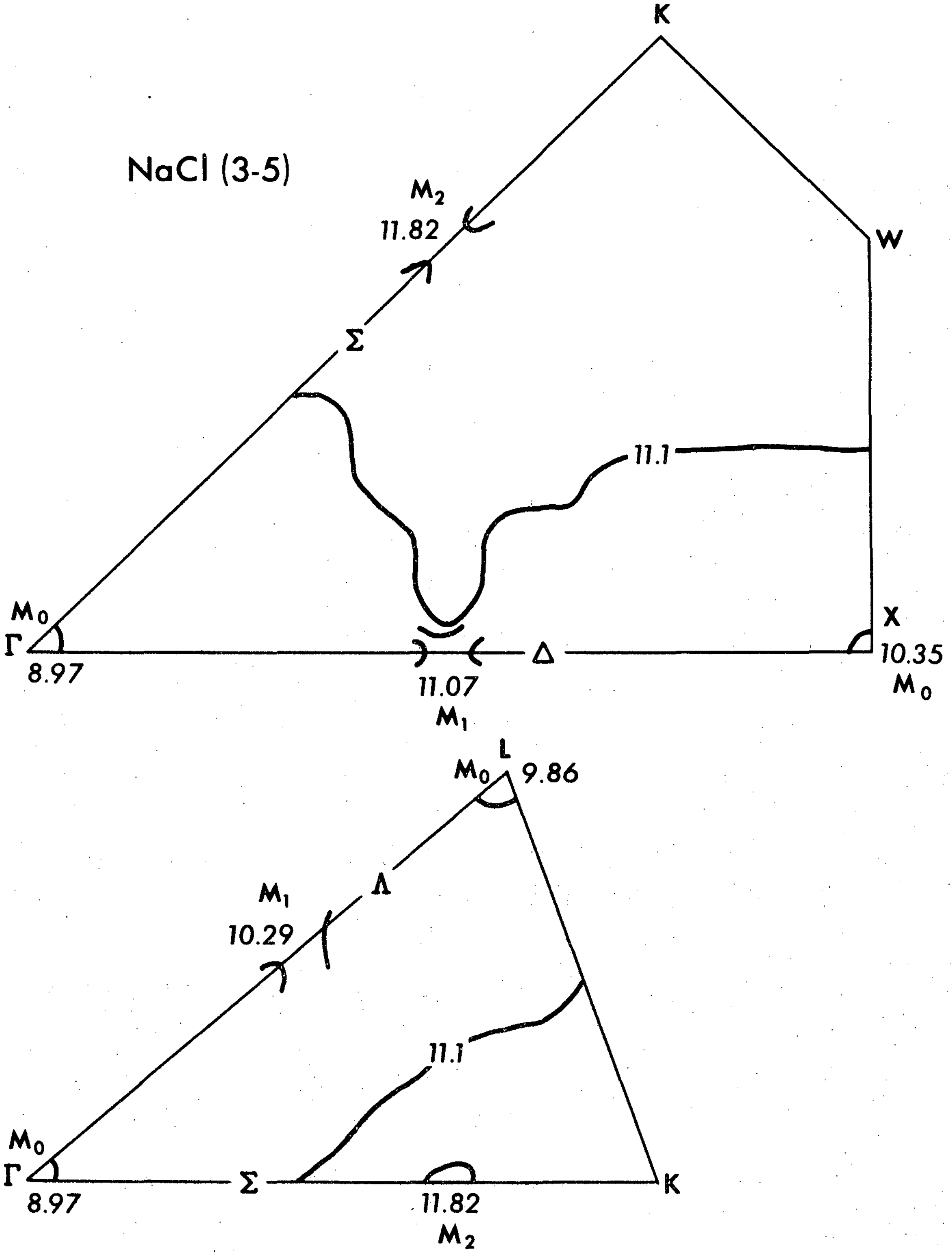
NaCl (3-5)
K
W
M$_2$
11.82
Σ
11.1
M$_0$
Γ
8.97
11.07
M$_1$
Δ
X
10.35
M$_0$
L
M$_0$
9.86
M$_1$
10.29
Λ
11.1
M$_0$
Γ
8.97
Σ
11.82
M$_2$
K

Fig. 24

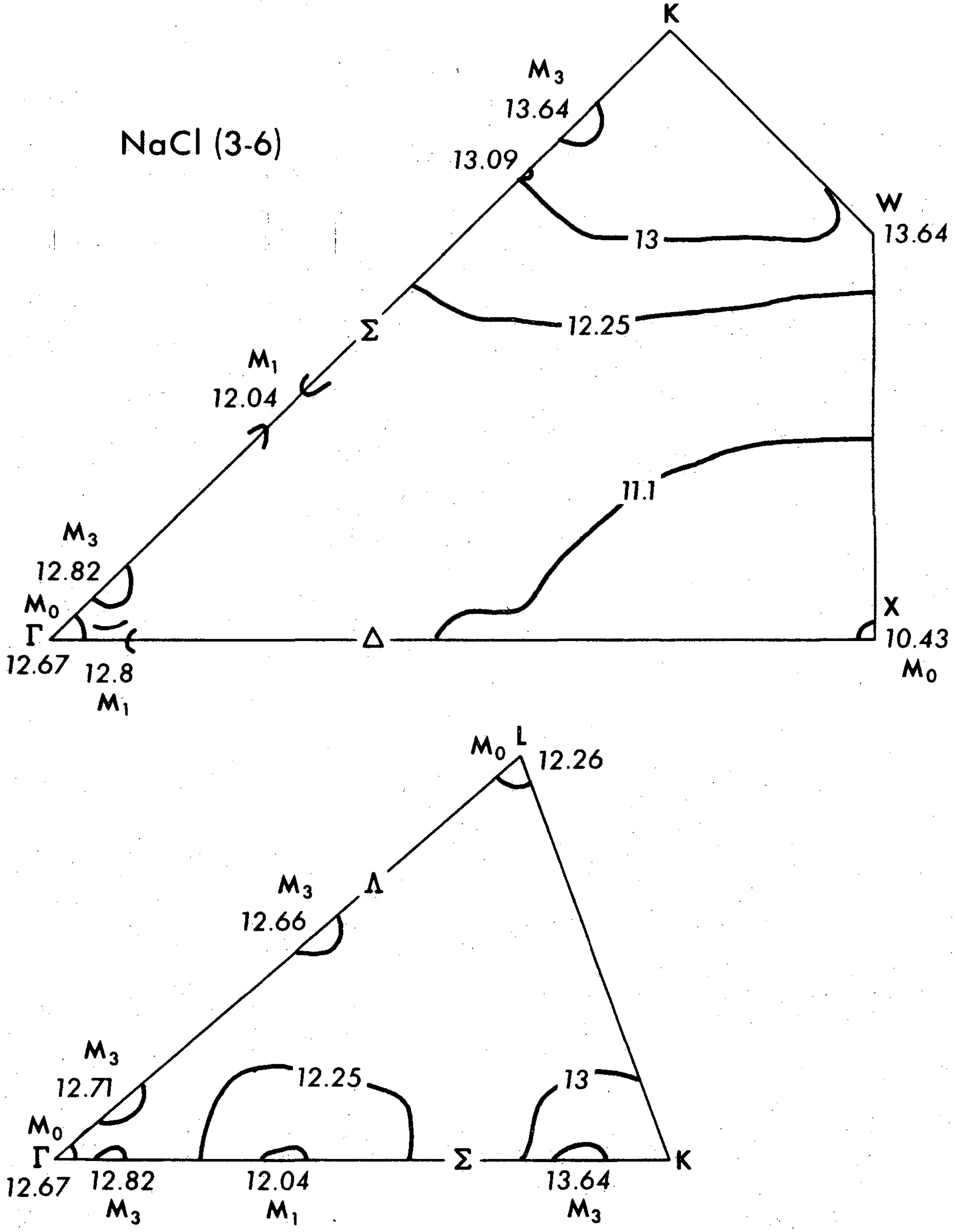
NaCl (3-6)
K
M3
13.64
13.09
W
13.64
13
12.25
Σ
M1
12.04
11.1
M3
12.82
M0
Γ
12.67
12.8
M1
Δ
X
10.43
M0
M0
L
12.26
M3
Λ
12.66
M3
12.71
M0
Γ
12.67
12.82
M3
12.25
12.04
M1
Σ
13
13.64
M3
K

Fig. 25

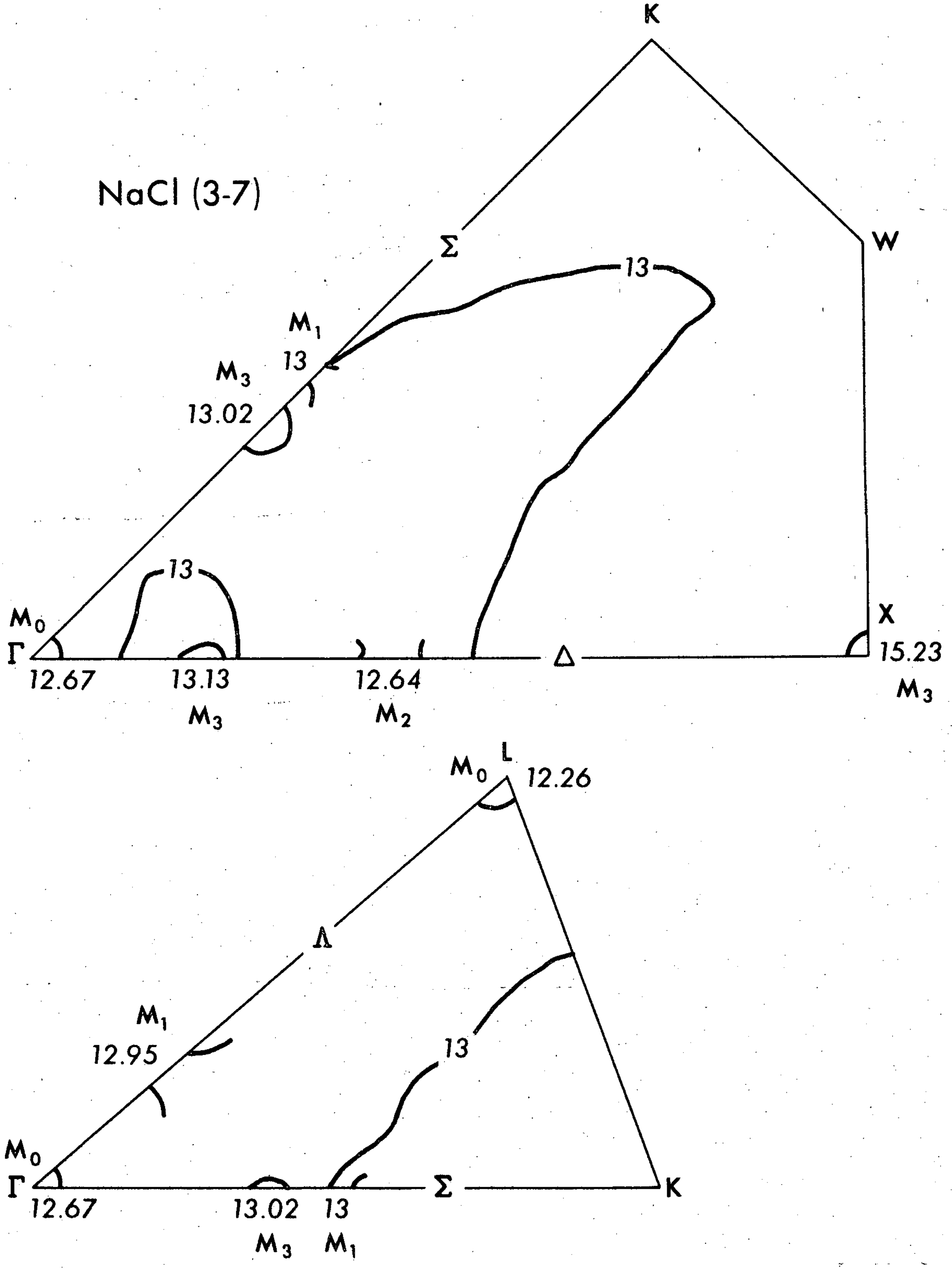
NaCl (3-7)
K
W
Σ
13
M₁
13
M₃
13.02
13
M₀
Γ
12.67
13.13
M₃
12.64
M₂
Δ
X
15.23
M₃
M₀
L
12.26
Λ
M₁
12.95
13
M₀
Γ
12.67
13.02
M₃
13
M₁
Σ
K

Fig. 26

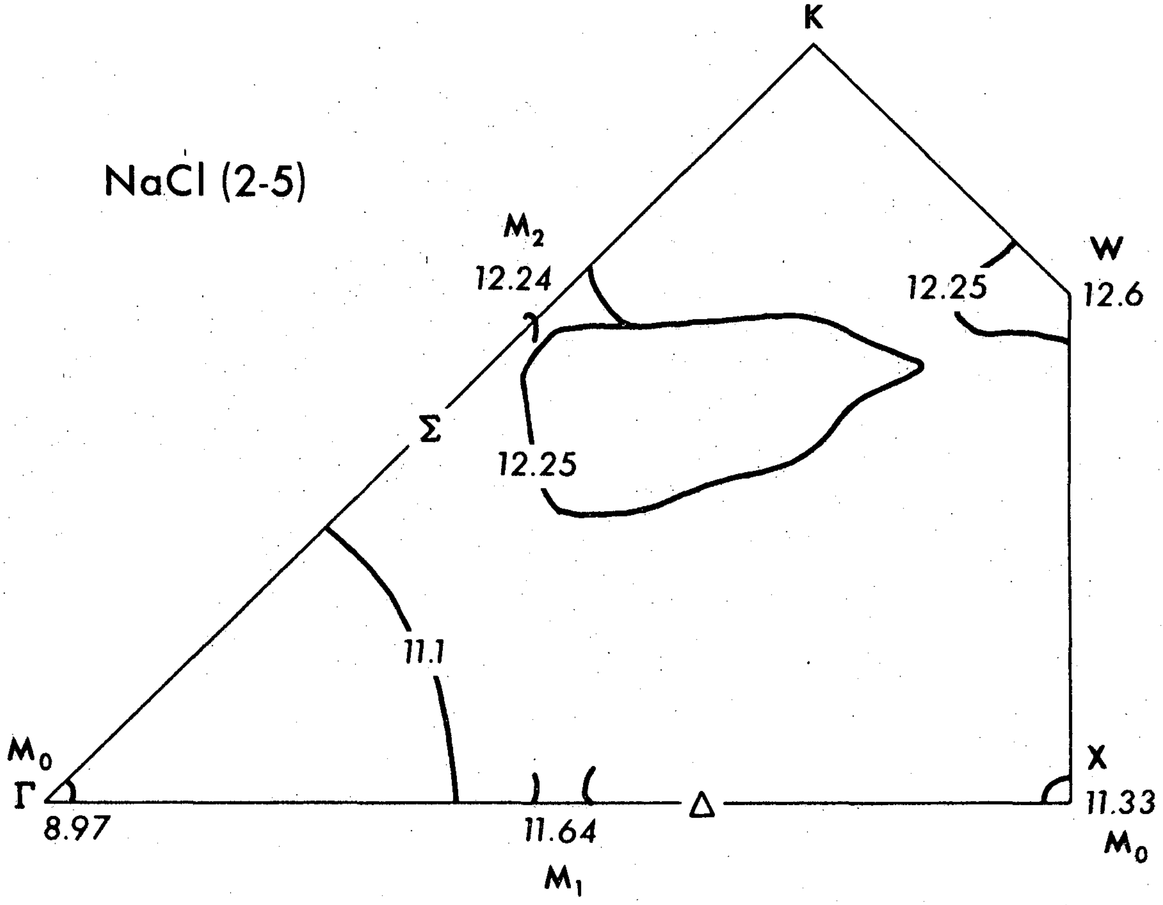
NaCl (2-5)
K
W
12.6
M₂
12.24
12.25
12.25
Σ
11.1
M₀
Γ
8.97
11.64
M₁
Δ
X
11.33
M₀

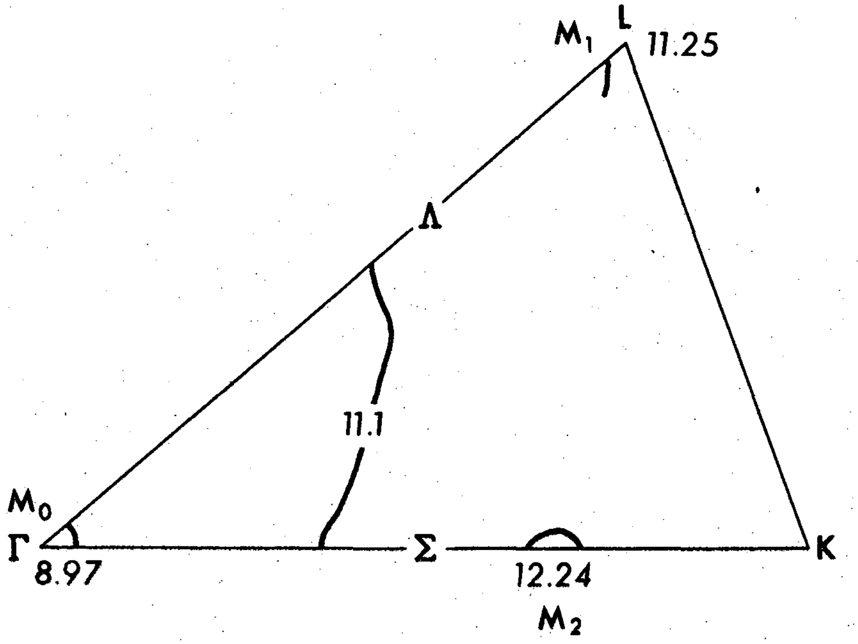
M₁
L
11.25
Λ
11.1
M₀
Γ
8.97
Σ
12.24
M₂
K

Fig. 27

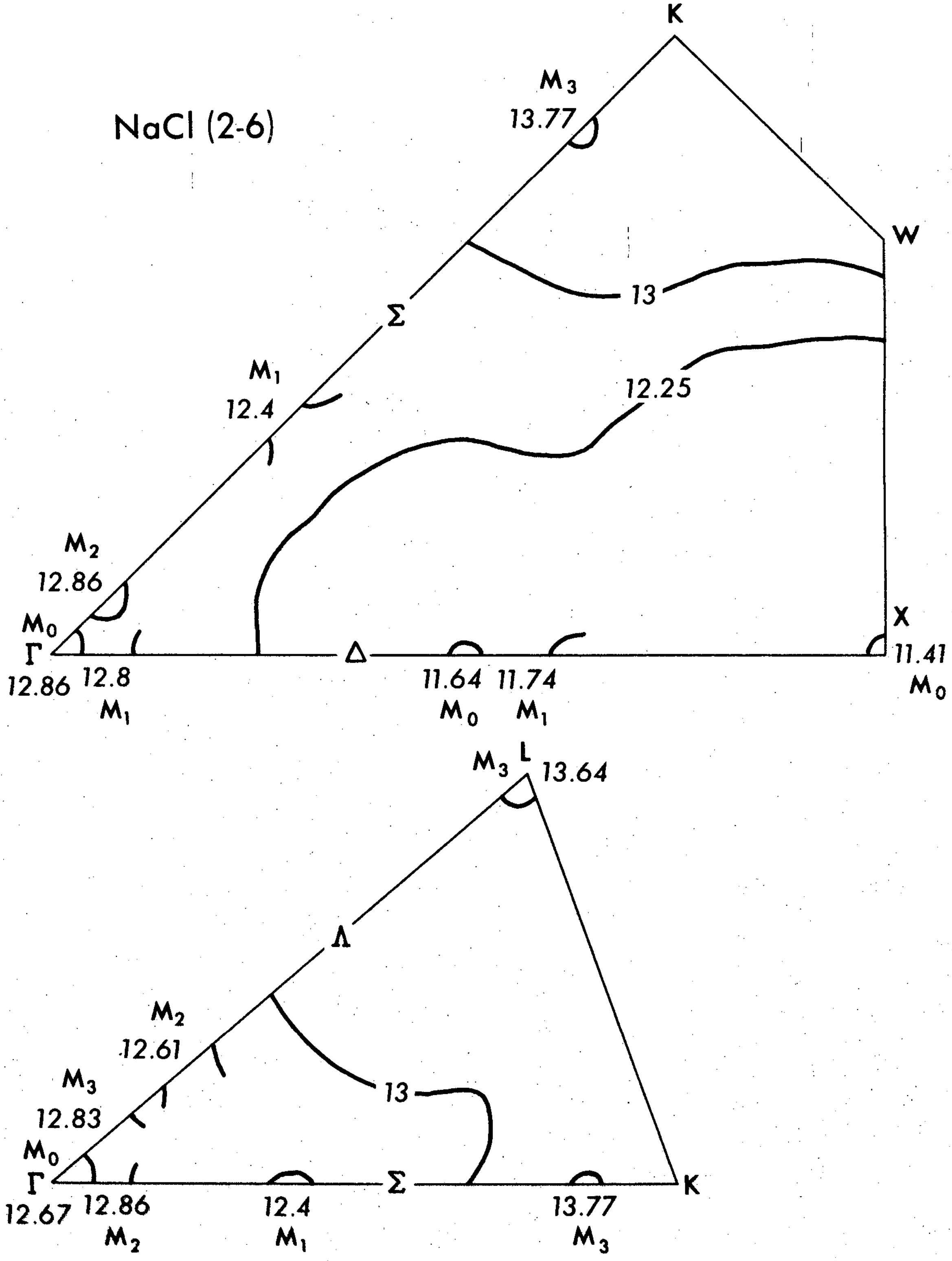

NaCl (2-6)

Fig. 28

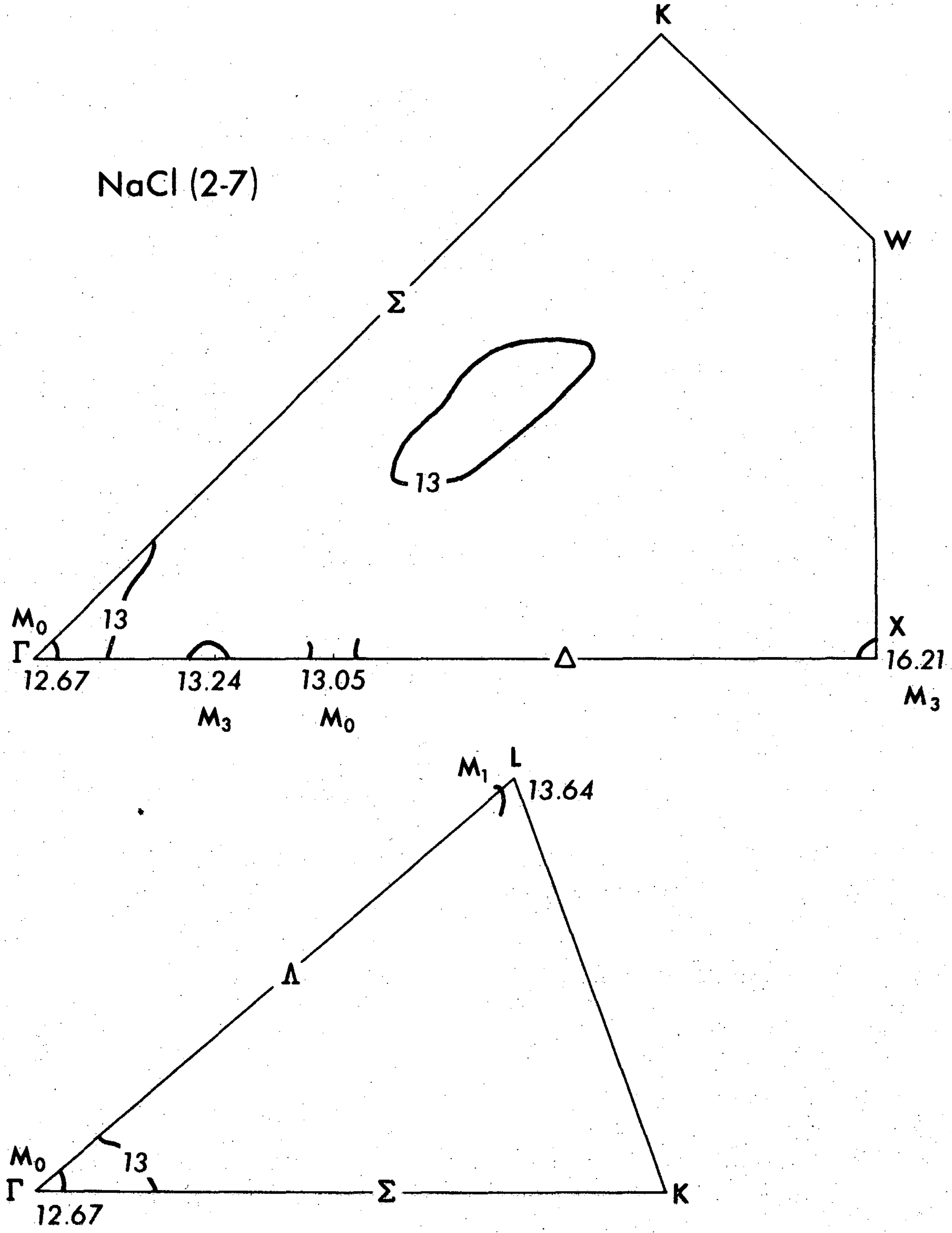
NaCl (2-7)
K
W
Σ
13
13
M_0
Γ
12.67
13.24
M_3
13.05
M_0
Δ
X
16.21
M_3
M_1
L
13.64
Λ
M_0
13
Γ
12.67
Σ
K

Fig. 29

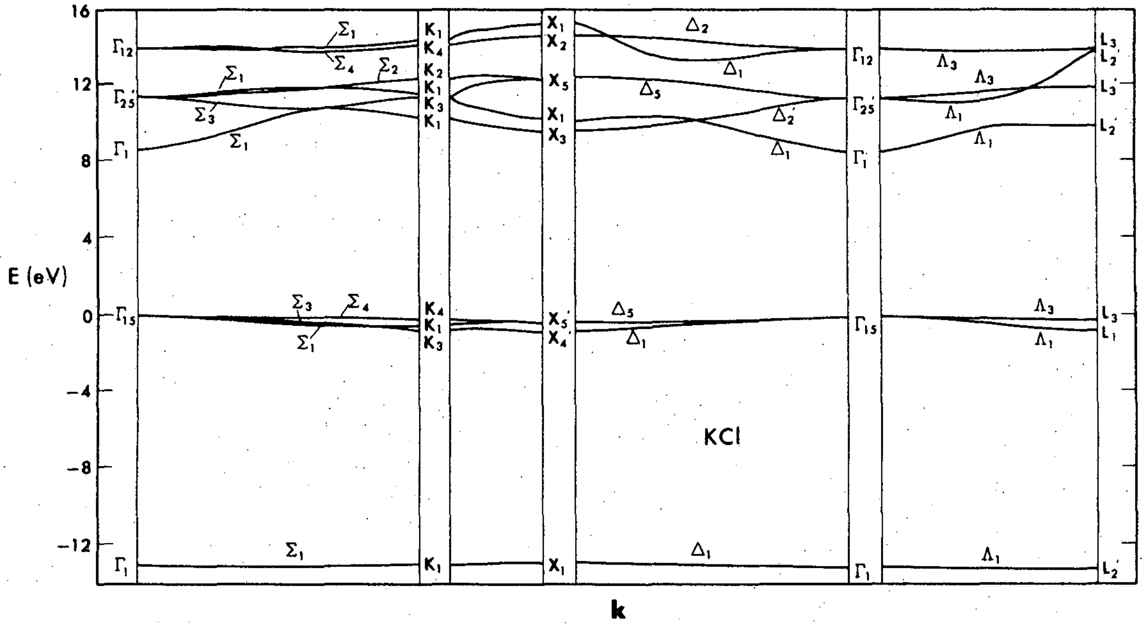
16
12
8
4
0
−4
−8
−12
E (eV)
k
KCl
Γ₁₂
Γ′₂₅
Γ₁
Γ₁₅
Γ₁
Σ₁
Σ₄
Σ₂
Σ₁
Σ′₃
Σ₁
Σ₃
Σ₄
Σ′₁
Σ₁
K₁
K₄
K₂
K₁
K₃
K₁
K₄
K₁
K₃
K₁
X₁
X₂
X₅
X₁
X₃
X′₅
X′₄
X₁
Δ₂
Δ₁
Δ₅
Δ′₂
Δ₁
Δ₅
Δ₁
Δ₁
Γ₁₂
Γ′₂₅
Γ′₁
Γ₁₅
Γ₁
Λ₃
Λ₃
Λ₁
Λ₁
Λ₃
Λ₁
Λ₁
L₃
L′₂
L′₃
L′₂
L₃
L₁
L′₂

Fig. 30

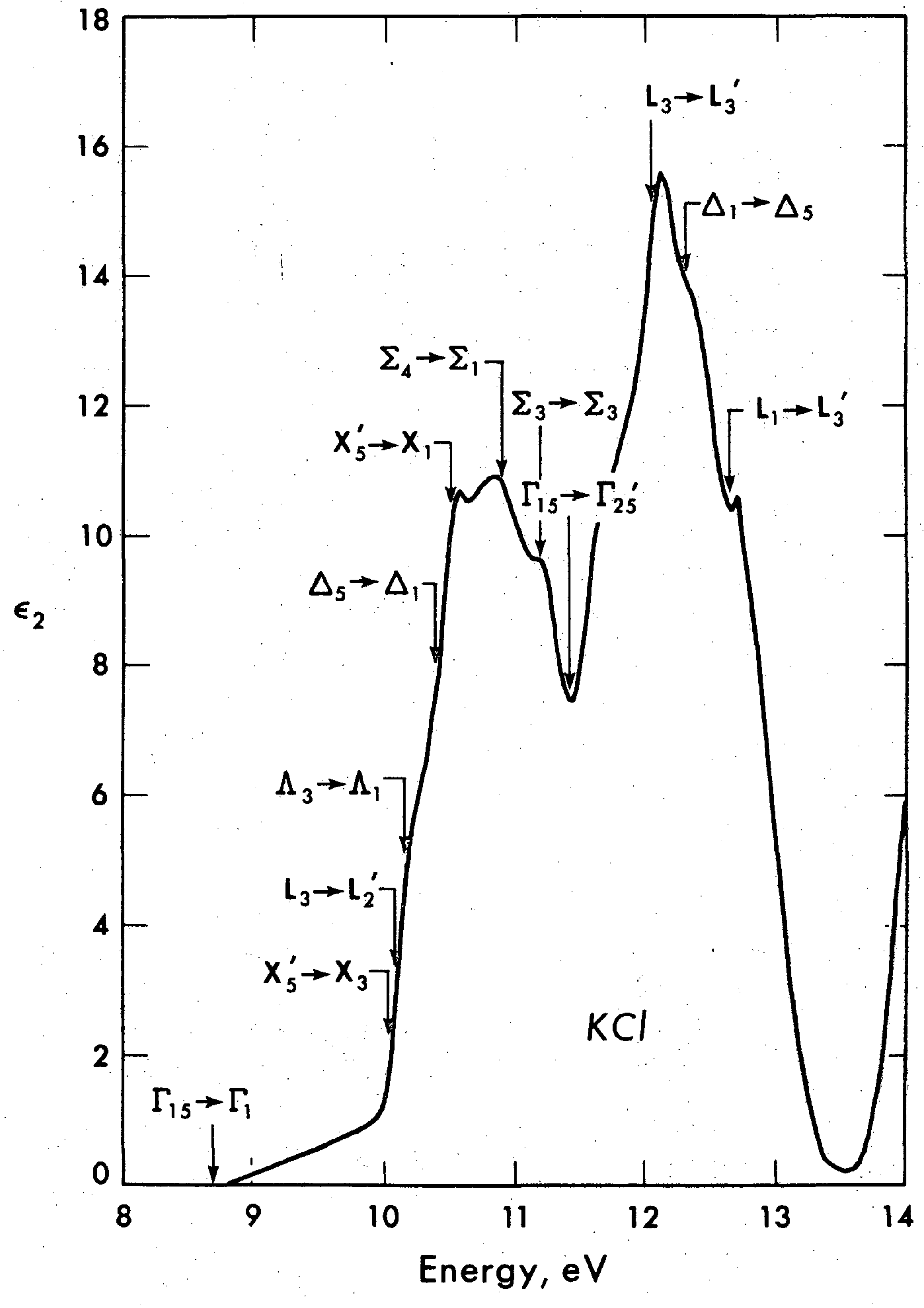

ϵ_2
18
16
14
12
10
8
6
4
2
0
8
9
10
11
12
13
14
Energy, eV
KCl
$L_3 \rightarrow L_3'$
$\Delta_1 \rightarrow \Delta_5$
$\Sigma_4 \rightarrow \Sigma_1$
$\Sigma_3 \rightarrow \Sigma_3$
$L_1 \rightarrow L_3'$
$X_5' \rightarrow X_1$
$\Gamma_{15} \rightarrow \Gamma_{25}'$
$\Delta_5 \rightarrow \Delta_1$
$\Lambda_3 \rightarrow \Lambda_1$
$L_3 \rightarrow L_2'$
$X_5' \rightarrow X_3$
$\Gamma_{15} \rightarrow \Gamma_1$

Fig. 31

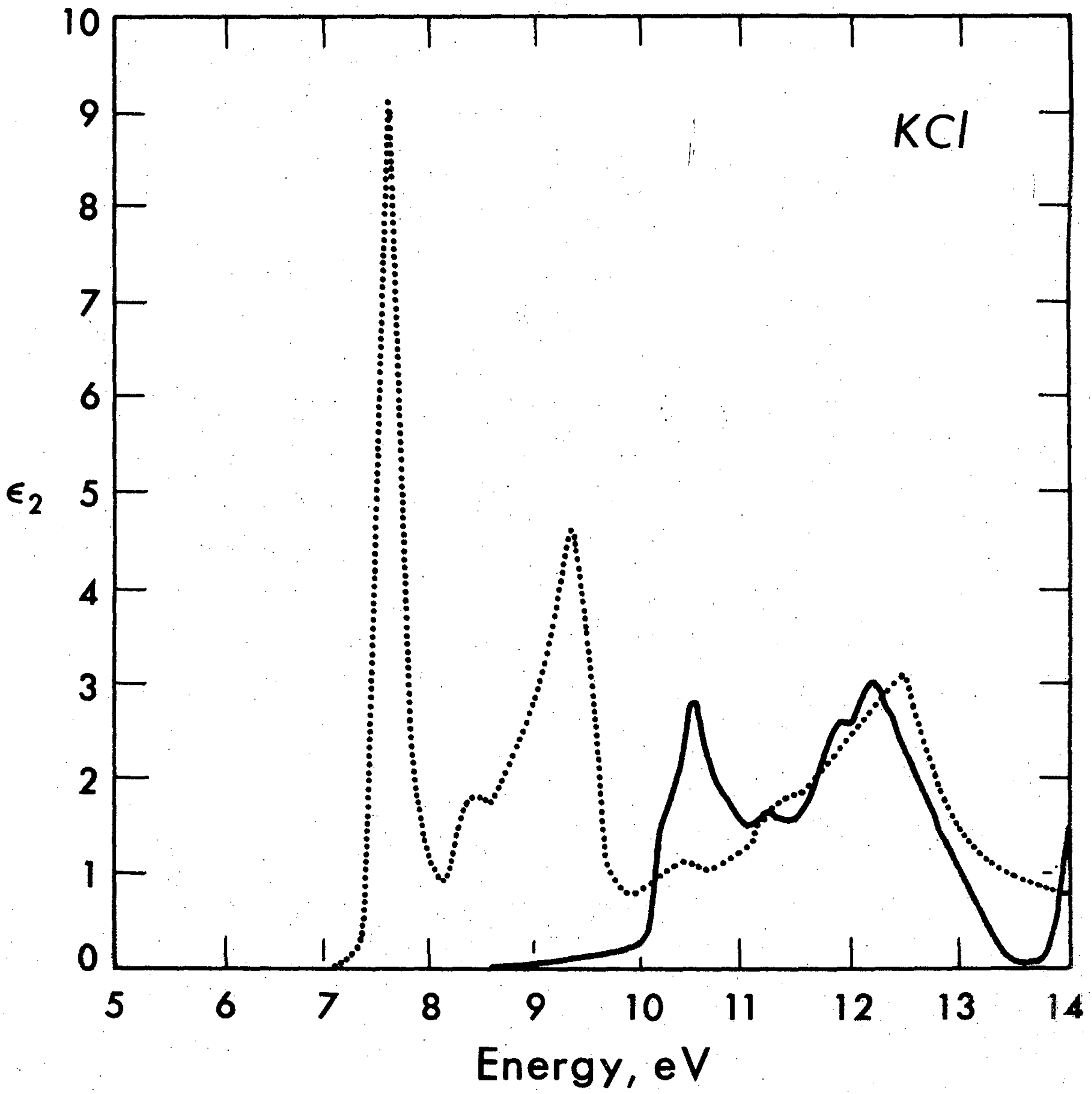

Fig. 32

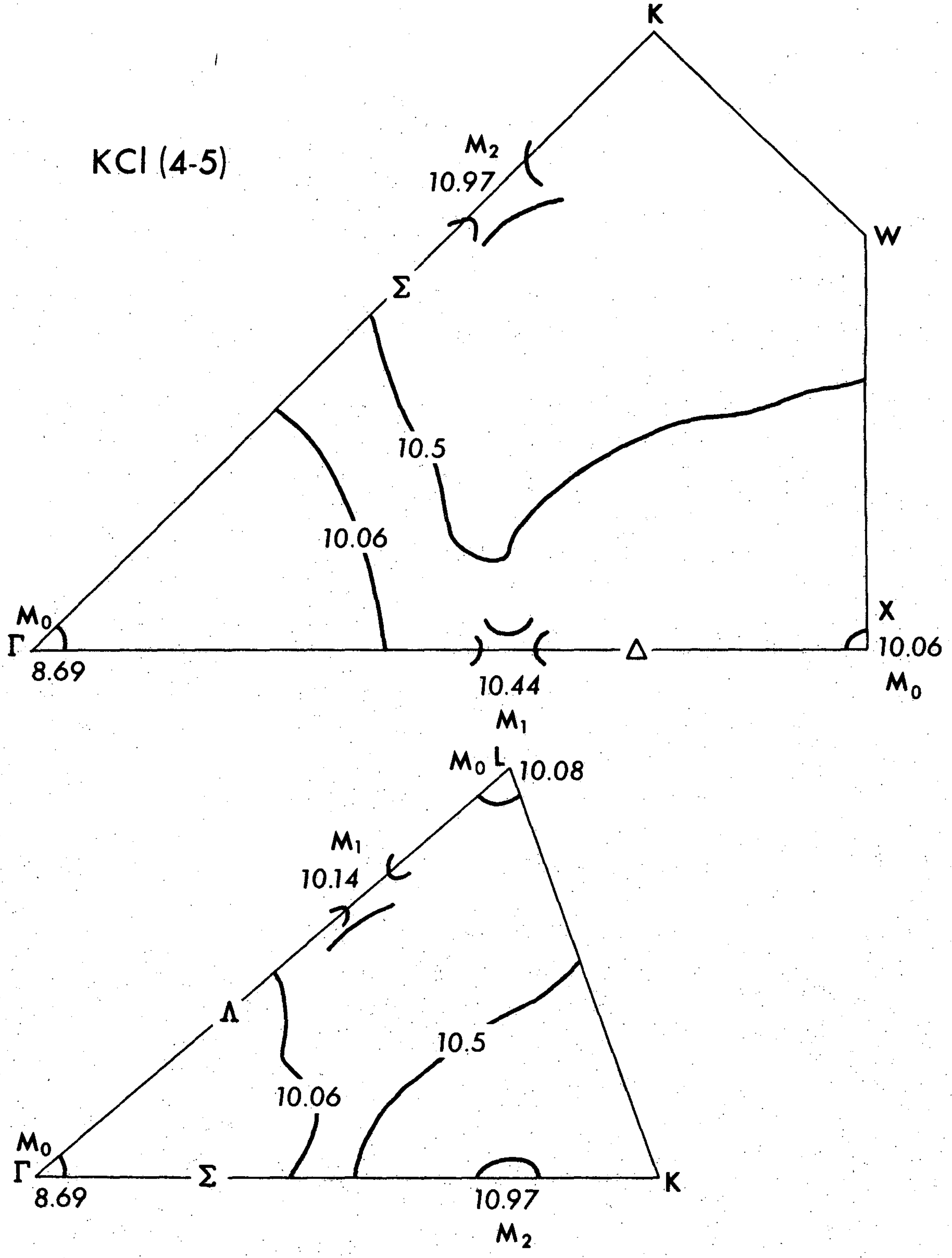
KCl (4-5)
K
M₂
10.97
W
Σ
10.5
10.06
M₀
Γ
8.69
10.44
M₁
Δ
X
10.06
M₀
M₀
L
10.08
M₁
10.14
Λ
10.5
10.06
M₀
Γ
8.69
Σ
10.97
M₂
K

Fig. 33

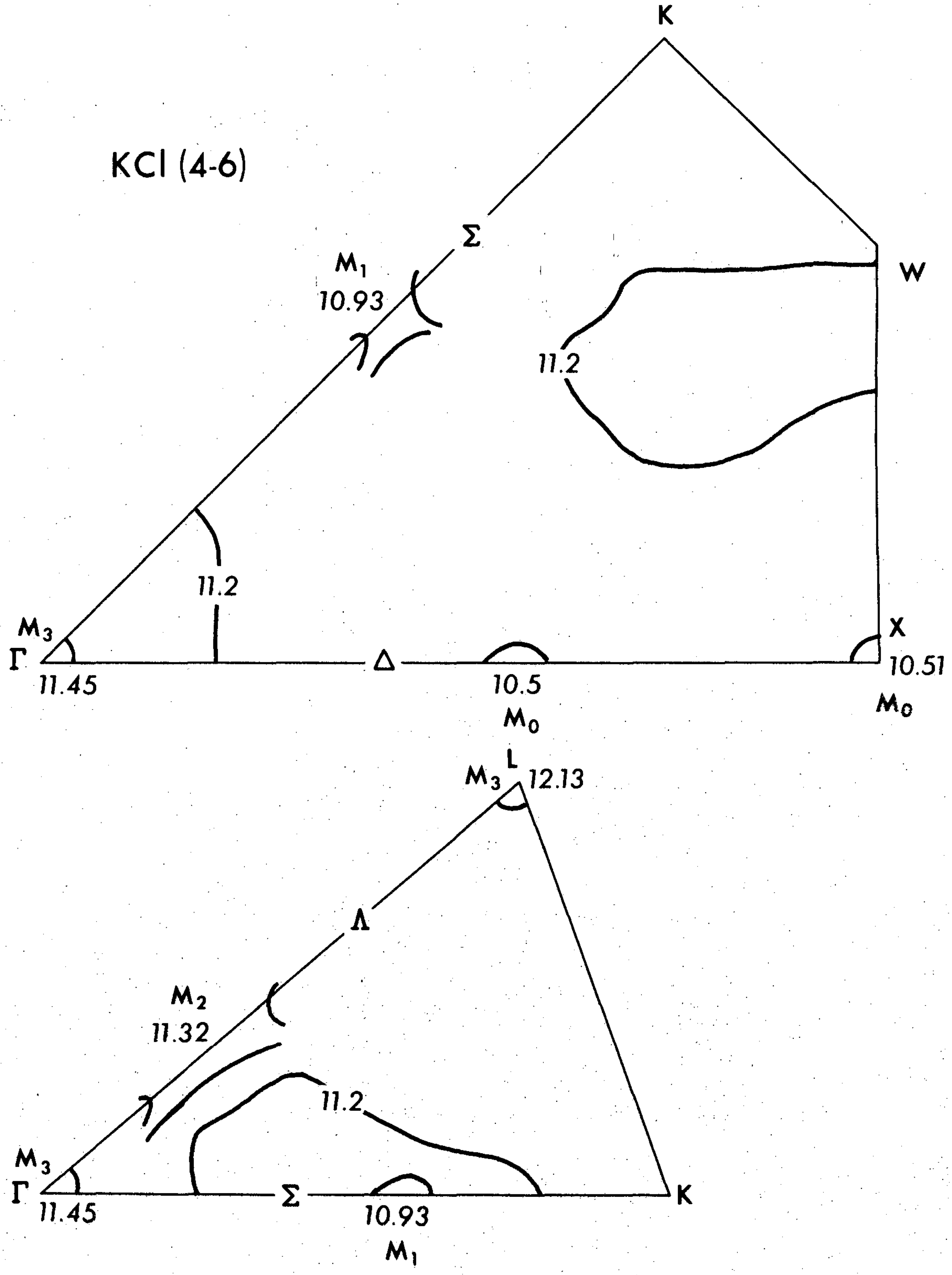
KCl (4-6)
K
Σ
M_1
10.93
W
11.2
11.2
M_3
Γ
11.45
Δ
10.5
M_0
X
10.51
M_0
L
M_3
12.13
Λ
M_2
11.32
11.2
M_3
Γ
11.45
Σ
10.93
M_1
K

Fig. 34

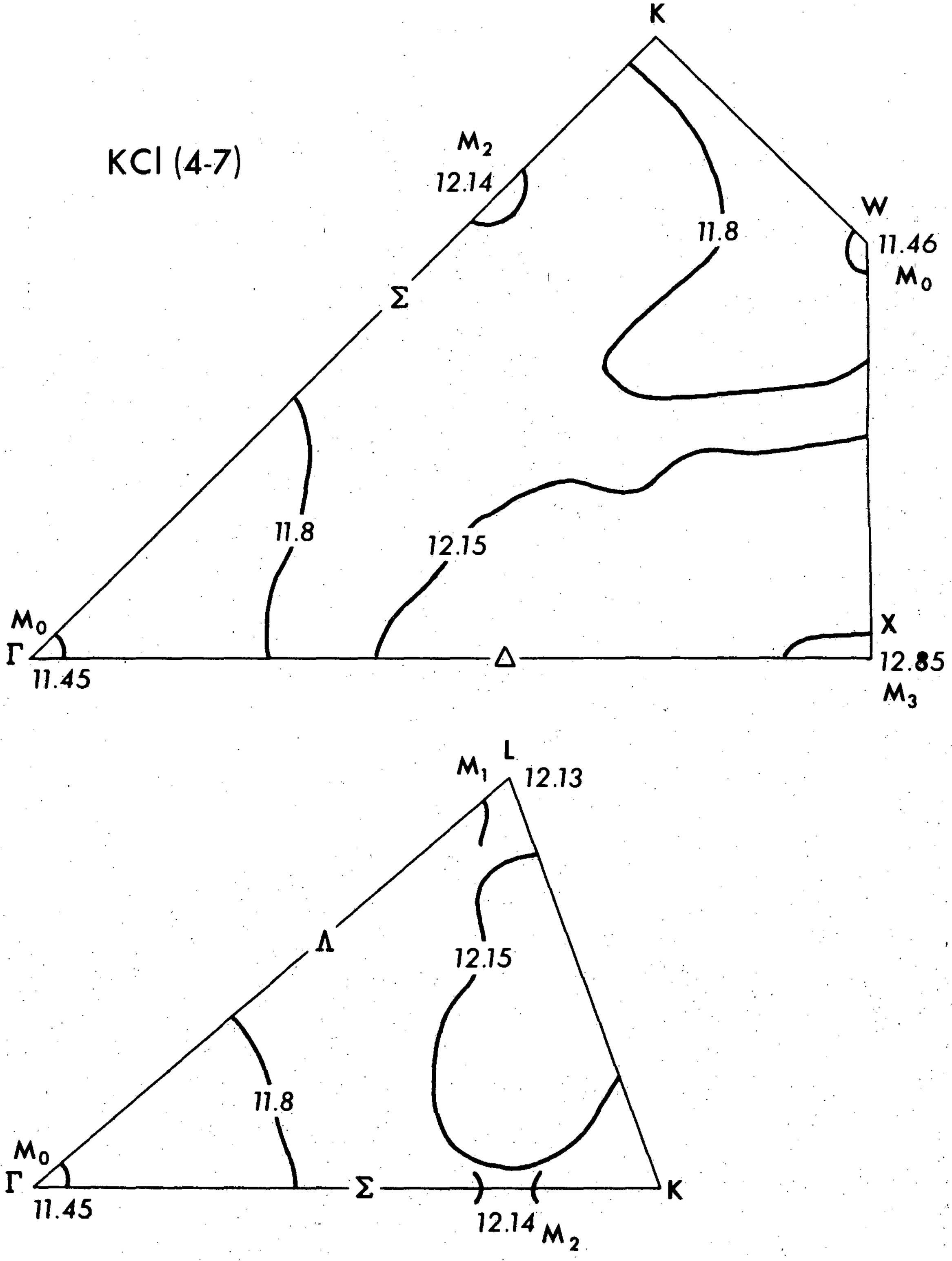
KCl (4-7)
K
M₂
12.14
11.8
W
11.46
M₀
Σ
11.8
12.15
M₀
Γ
11.45
Δ
X
12.85
M₃
L
M₁
12.13
Λ
12.15
11.8
M₀
Γ
11.45
Σ
12.14
M₂
K

Fig. 35

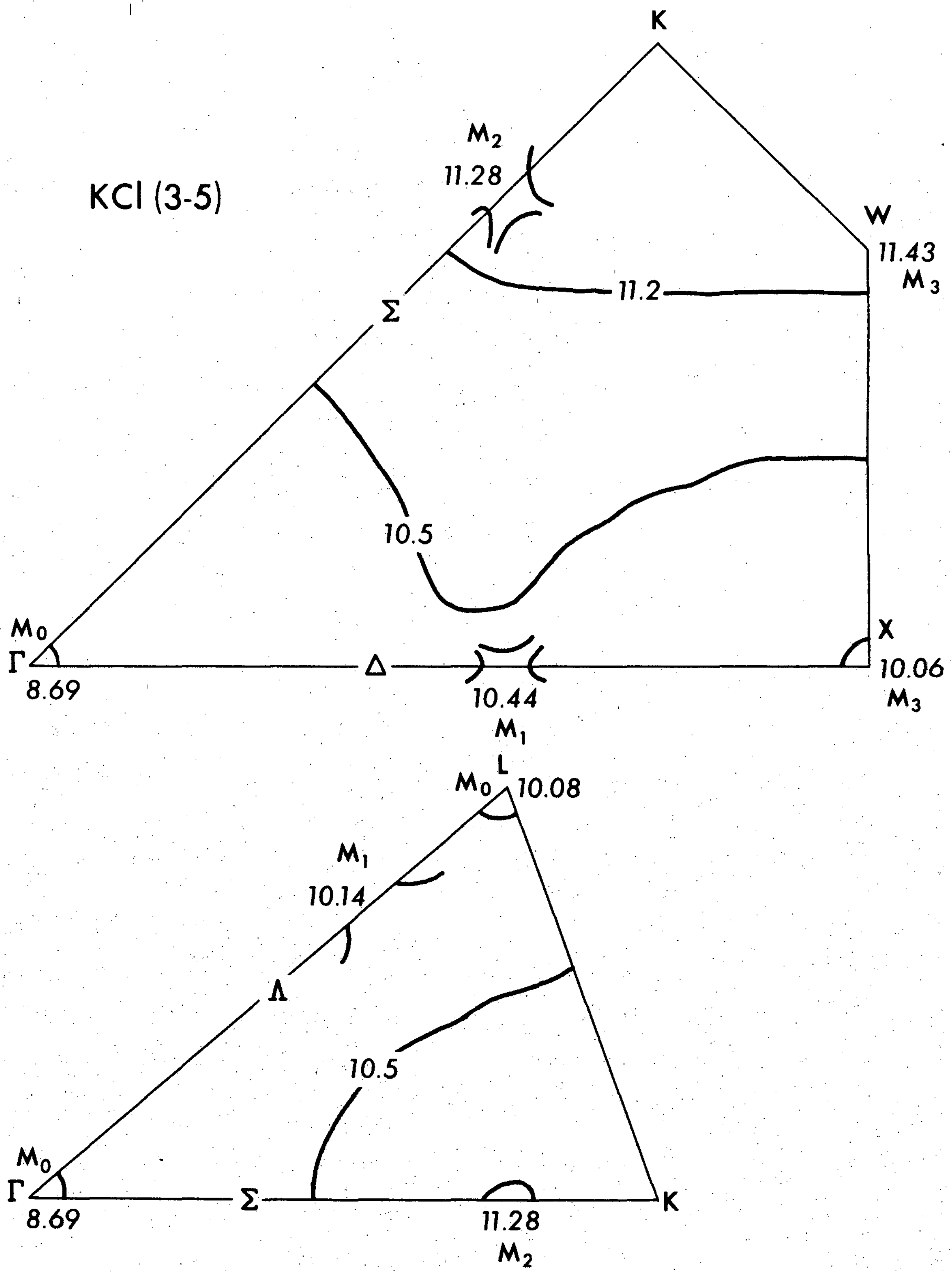
KCl (3-5)
K
M₂
11.28
W
11.43
M₃
Σ
11.2
10.5
M₀
Γ
8.69
Δ
10.44
M₁
X
10.06
M₃
L
M₀
10.08
M₁
10.14
Λ
10.5
M₀
Γ
8.69
Σ
11.28
M₂
K

Fig. 36

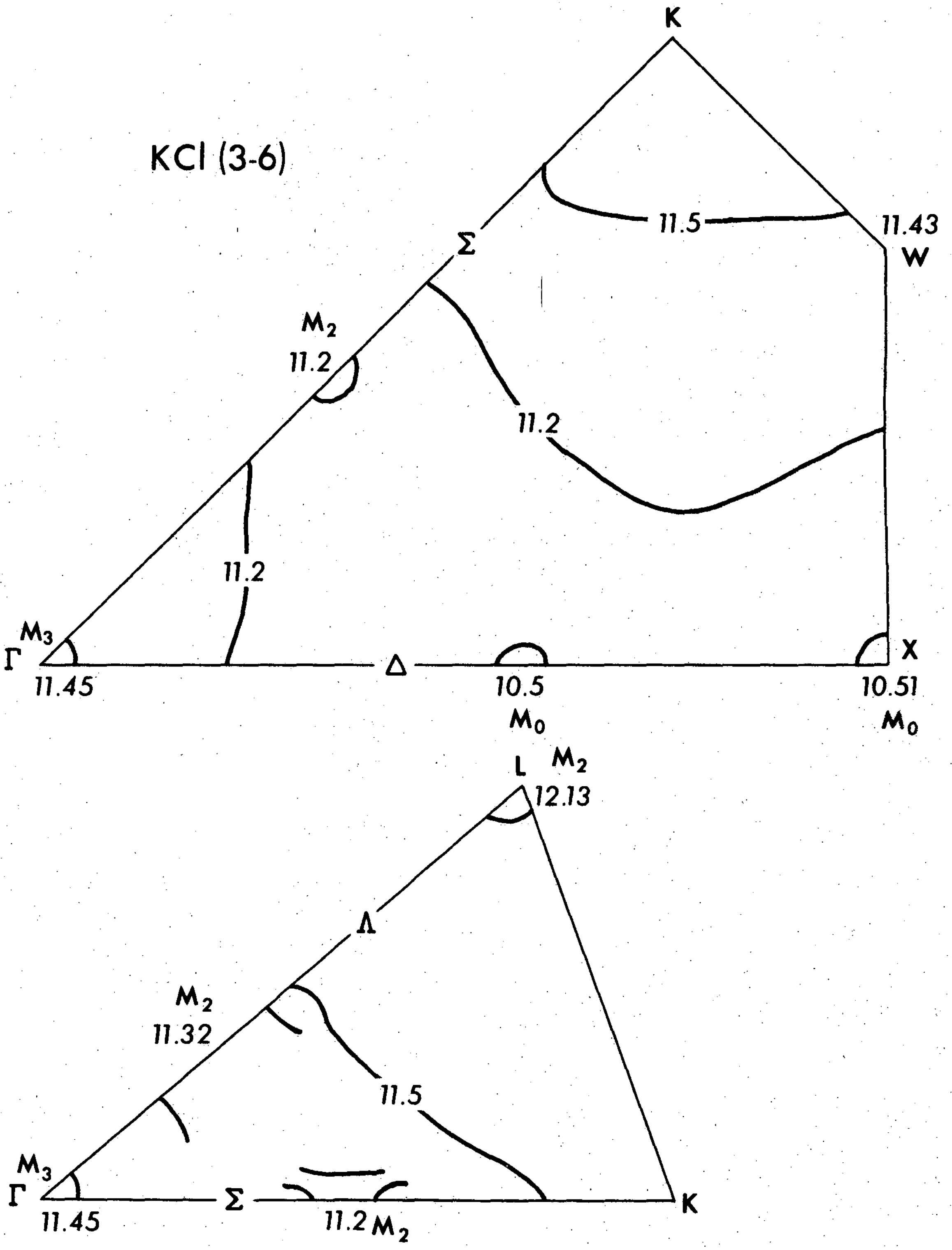
KCl (3-6)
K
Σ
11.5
11.43
W
M₂
11.2
11.2
11.2
M₃
Γ
11.45
Δ
10.5
M₀
X
10.51
M₀
L
M₂
12.13
Λ
M₂
11.32
11.5
M₃
Γ
11.45
Σ
11.2
M₂
K

Fig. 37

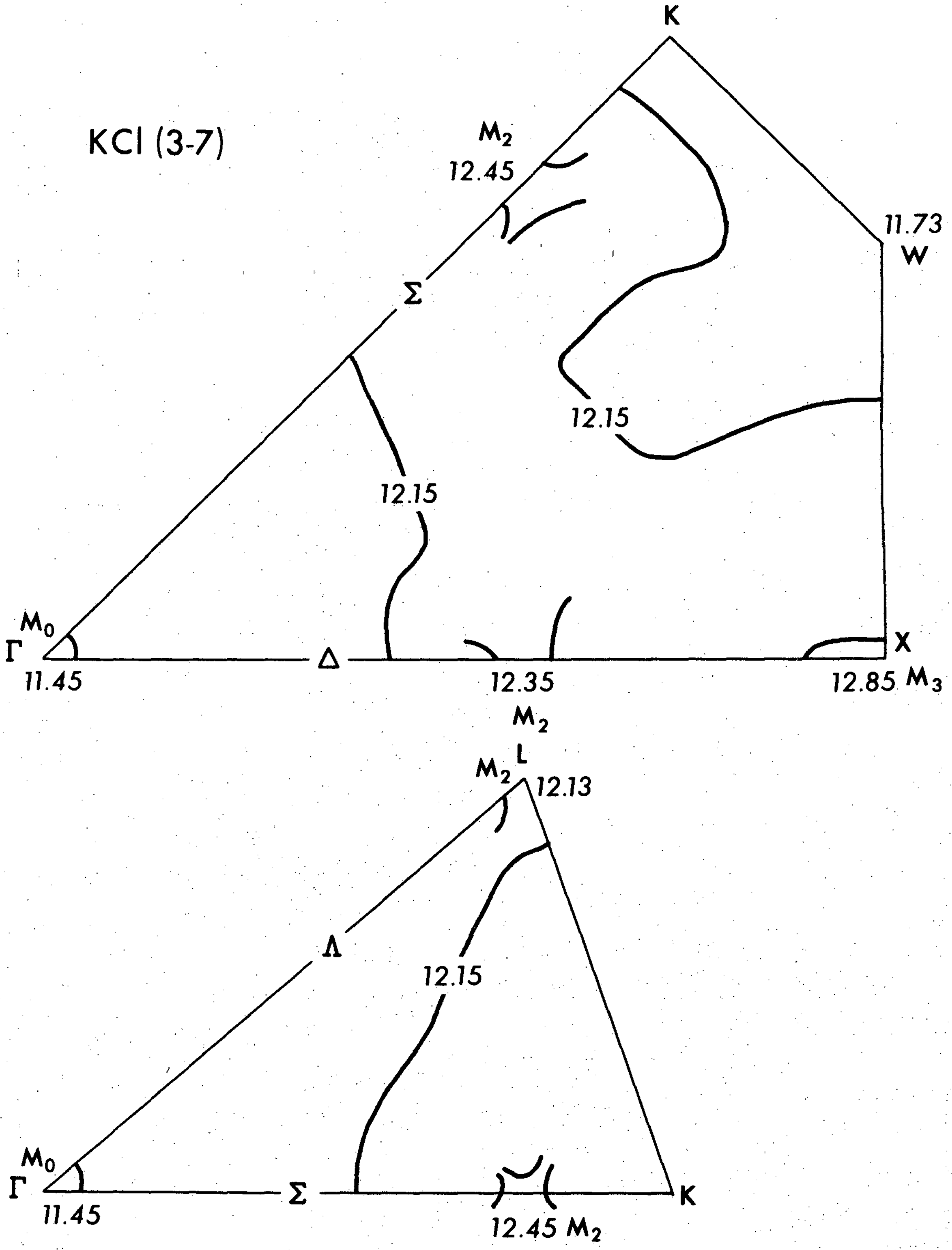
KCl (3-7)
K
M$_2$
12.45
11.73
W
Σ
12.15
12.15
M$_0$
Γ
11.45
Δ
12.35
X
12.85
M$_3$
M$_2$
L
M$_2$
12.13
Λ
12.15
M$_0$
Γ
11.45
Σ
K
12.45
M$_2$

Fig. 38

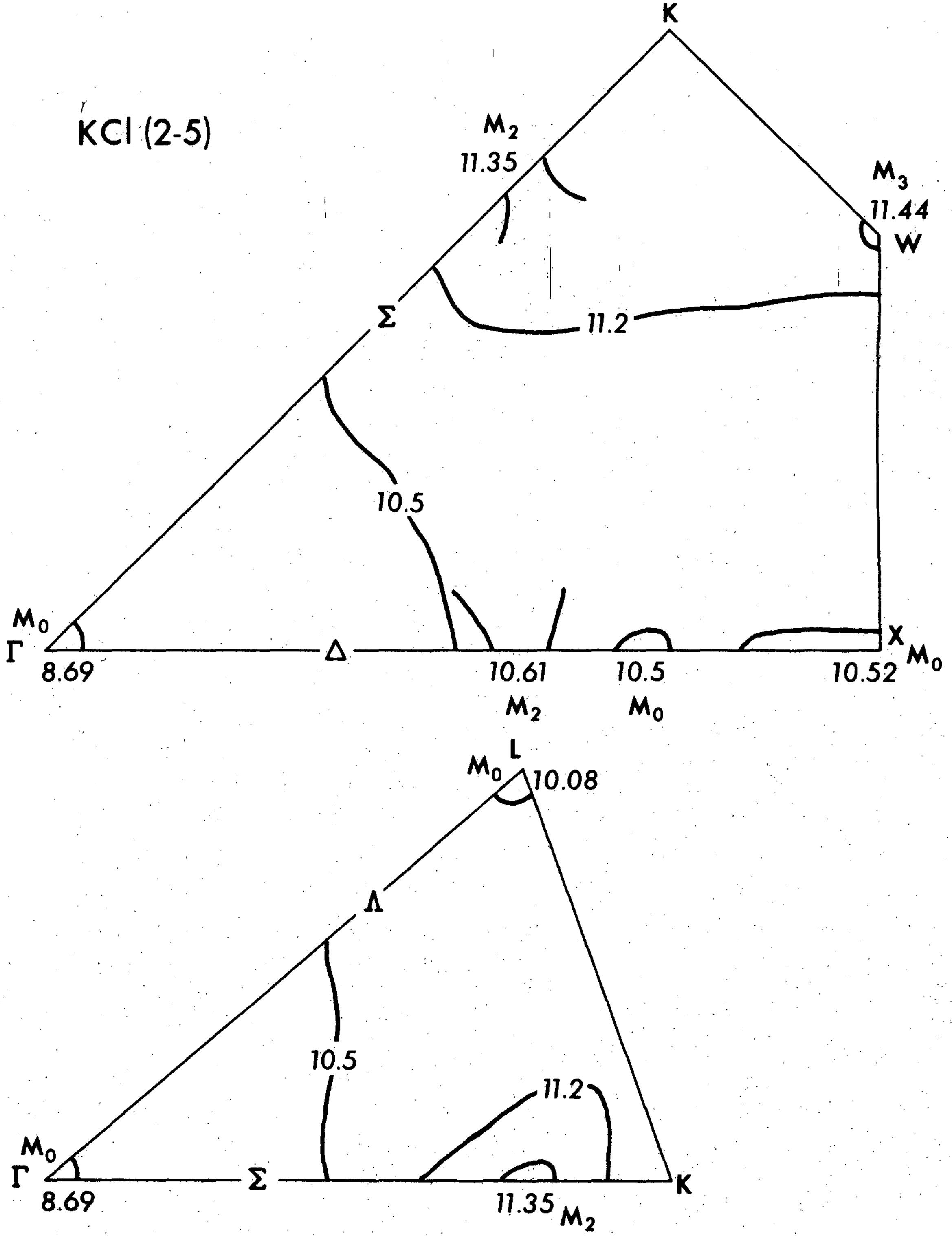
KCl (2-5)
K
M₂
11.35
M₃
11.44
W
Σ
11.2
10.5
M₀
Γ
8.69
Δ
10.61
M₂
10.5
M₀
10.52
X
M₀
L
M₀
10.08
Λ
10.5
11.2
M₀
Γ
8.69
Σ
11.35
M₂
K

Fig. 39

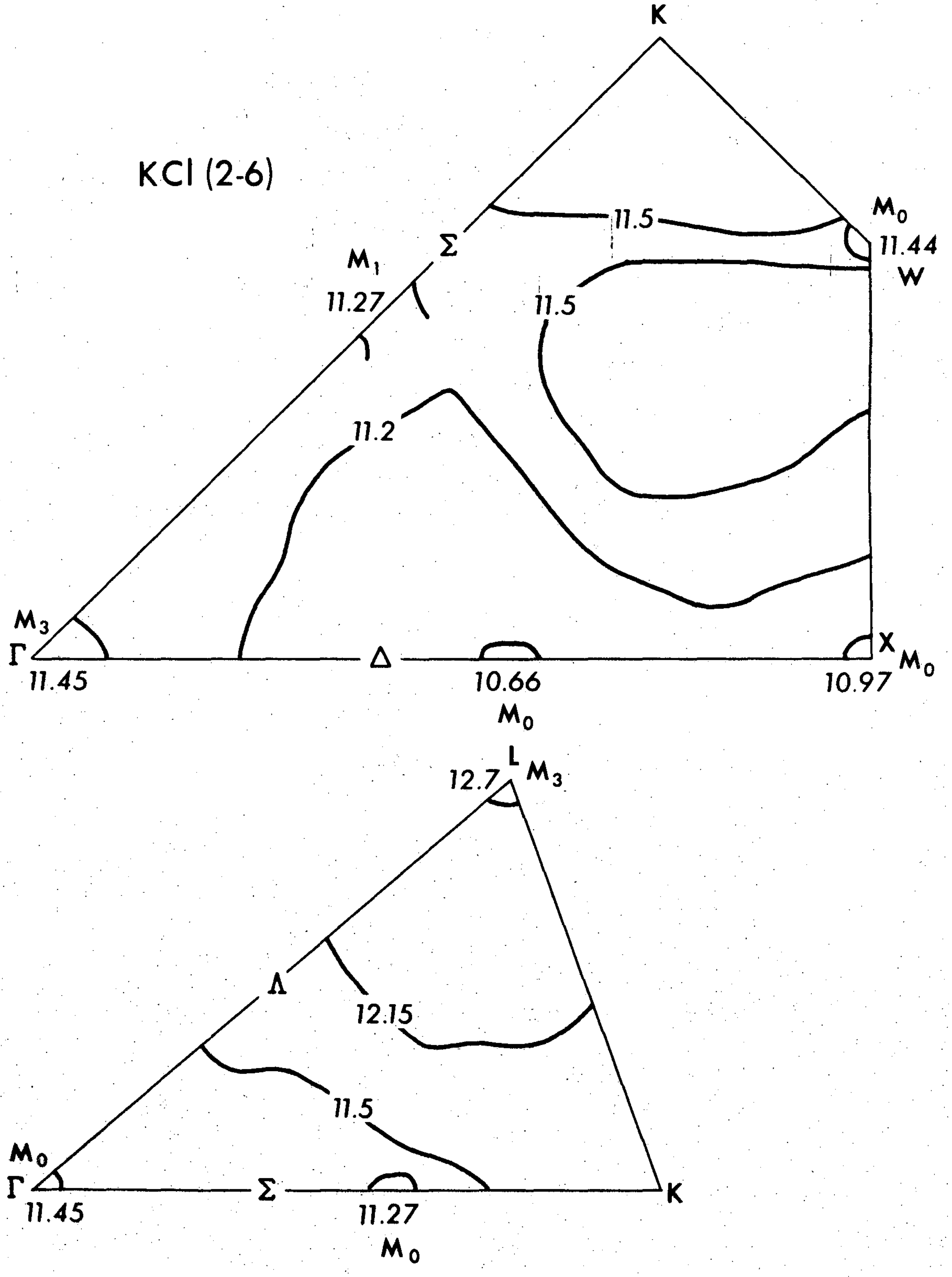
KCl (2-6)
K
Σ
M₁
11.27
11.5
11.5
M₀
11.44
W
11.2
M₃
Γ
11.45
Δ
10.66
M₀
X
M₀
10.97
L
12.7
M₃
Λ
12.15
11.5
M₀
Γ
11.45
Σ
11.27
M₀
K

Fig. 40

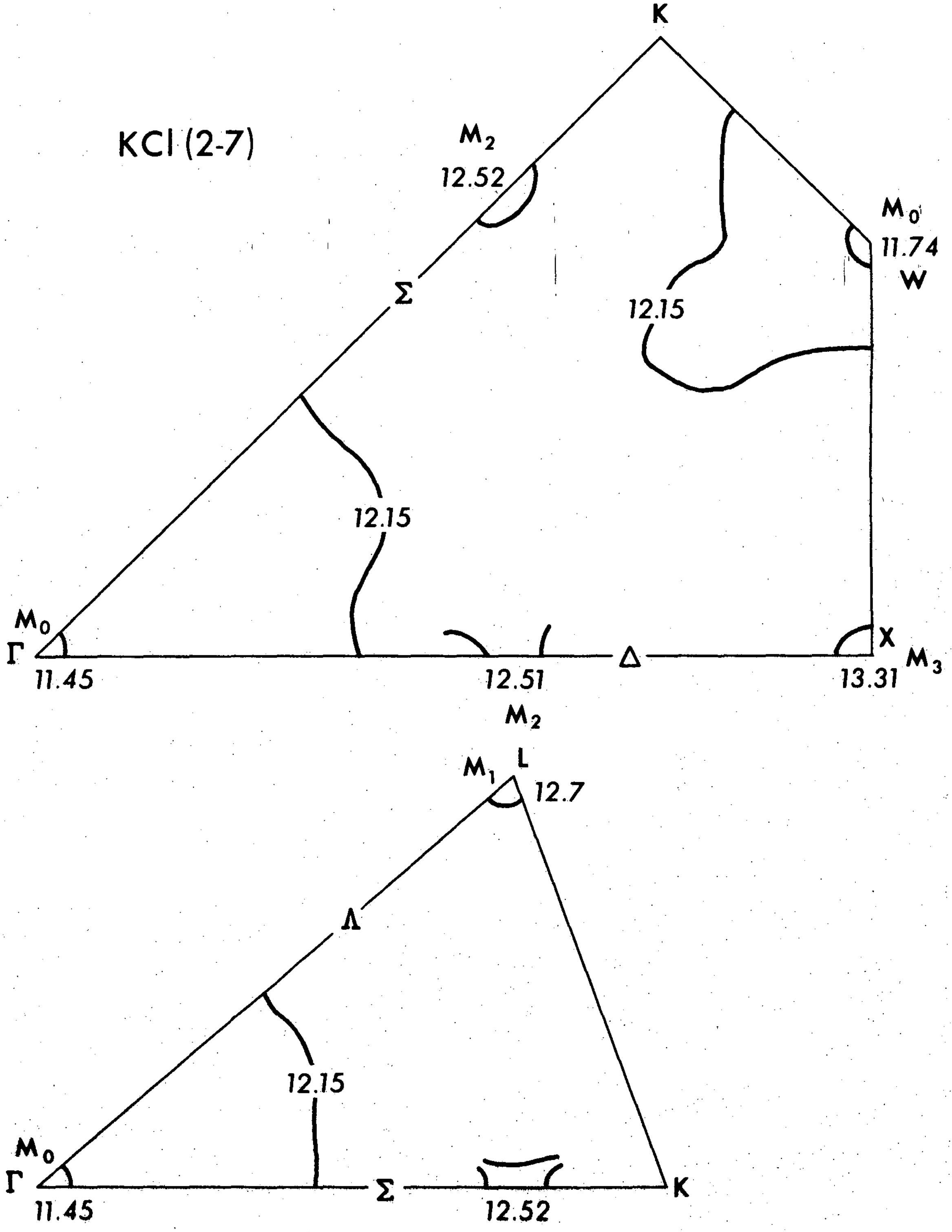
KCl (2-7)
K
M₂
12.52
Σ
M₀
11.74
W
12.15
12.15
M₀
Γ
11.45
12.51
M₂
Δ
X
M₃
13.31
M₁
L
12.7
Λ
12.15
M₀
Γ
11.45
Σ
12.52
K

Fig. 41

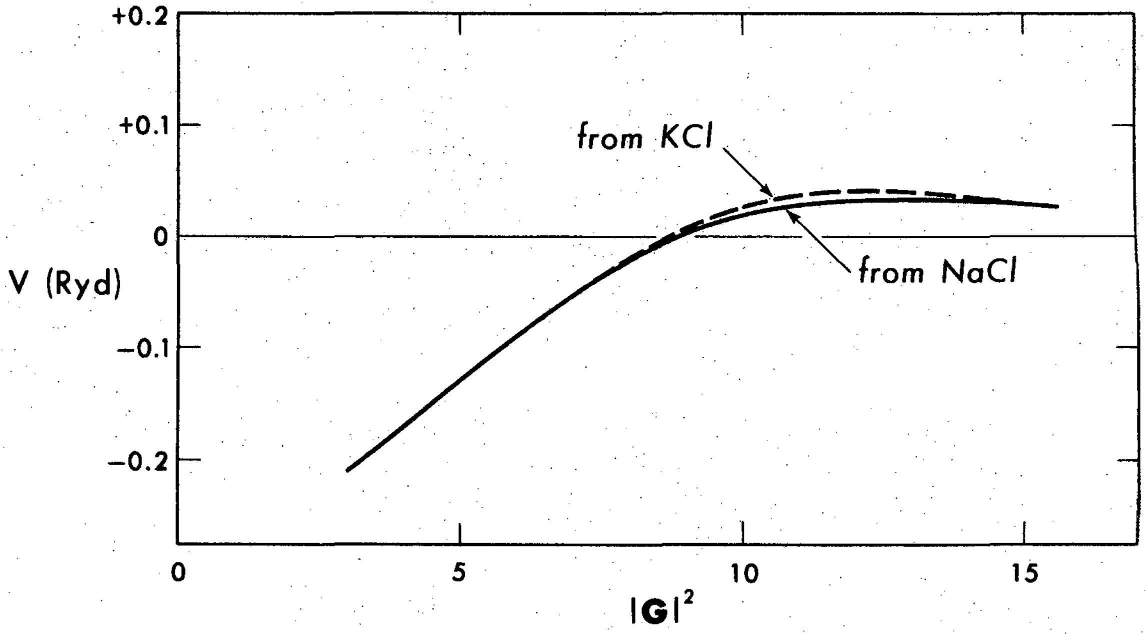

Fig. 42

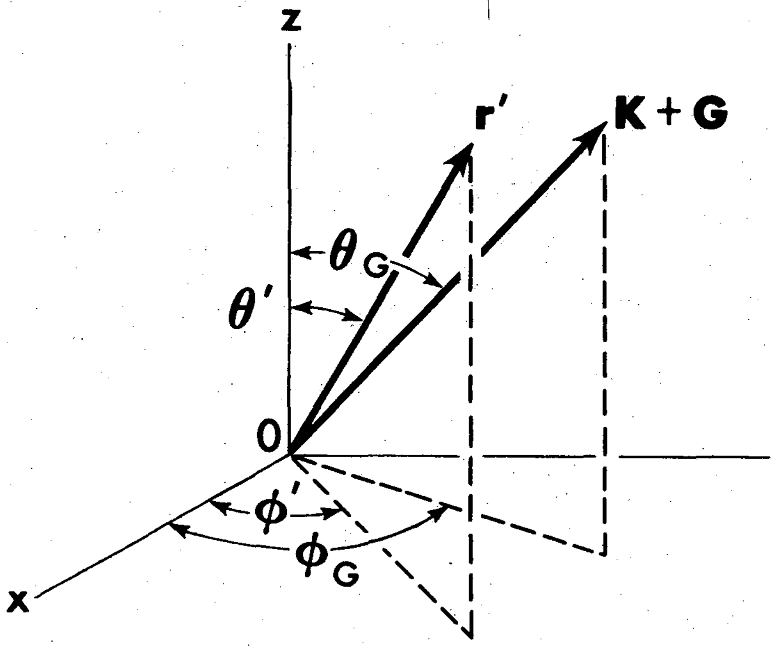

Fig. A1

Table I.

Form Factor	Current Calculation	Reference 14
$V^S(200)$	-0.0956 Ryd.	-0.1008 Ryd.
$V^S(220)$	0.0705	0.0745
$V^S(222)$	0.0191	0.0238
$V^A(111)$	0.2471	0.2500
$V^A(311)$	0.0136	0.0160

Table II.

Prominent Interband Transitions	Energy (theory) (eV)	Energy (experiment) (eV)
$\Gamma_{15} \to \Gamma_1$	7.76	7.77
$\Lambda_3 \to \Lambda_1$ (10.8) $L_3 \to L_2'$	11.1 (peak)	10.8 (peak)
$\Delta_5 \to \Delta_1$ $\Sigma_4 \to \Sigma_1$ (13.3) ($4 \to 5$)	13.2 (peak)	13.2 (peak)
$L_3 \to L_3'$	15.2	15.7
$\Sigma_3 \to \Sigma_1$	15.7 (peak)	16.8 (peak)
$\Lambda_3 \to \Lambda_3$	16.2 (peak)	17.4 (peak)
$\Sigma_4 \to \Sigma_1$ ($4 \to 6$)	19	20.5

Table III.

Calculated Critical Point Energy (eV)	Band Transition	Symmetry
7.77	$\Gamma_{15} \rightarrow \Gamma_1$	M_0
10.885	$L_3 \rightarrow L_2'$	M_0
10.893	$\Lambda_3 \rightarrow \Lambda_1$	M_1
12.35	$X_5 \rightarrow X_1$	M_0
13.04	$\Delta_5 \rightarrow \Delta_1$	M_1
13.3	$\Sigma_4 \rightarrow \Sigma_1$ $(4 \rightarrow 5)$	M_2
14.02	$X'_5 \rightarrow X_3$	M_0
15.2	$L_3 \rightarrow L'_3$	M_0
15.35	$\Delta_1 \rightarrow \Delta_1$	M_1
15.43	$\Gamma_{15} \rightarrow \Gamma'_{25}$	M_0
15.57	$\Delta_5 \rightarrow \Delta_2'$ $(3 \rightarrow 6)$	M_1
15.573	$\Sigma_4 \rightarrow \Sigma$ (forbidden)	M_1
15.576	$\Delta_5 \rightarrow \Delta_2'$ $(4 \rightarrow 6)$	M_3
15.59	$L_1 \rightarrow L_2'$	M_1
15.66	$\Sigma_3 \rightarrow \Sigma_1$ $(3 \rightarrow 5)$	M_2
16.2	$\Lambda_3 \rightarrow \Lambda_3$ $(4 \rightarrow 6,7)$ $(3 \rightarrow 6,7)$	M_3
16.39	$\Sigma_4 \rightarrow \Sigma_2$	M_2
16.59	$\Sigma_1 \rightarrow \Sigma_1$ $(2 \rightarrow 5)$	M_2
16.63	$\Delta_5 \rightarrow \Delta_1$ $(4 \rightarrow 7)$	M_2
16.93	$X_{4'} \rightarrow X_3$ (forbidden)	M_1

Table III. (continued)

Calculated Critical Point Energy (eV)	Band Transition	Symmetry
17.01	$\Delta_5 \rightarrow \Delta_1$ $(3 \rightarrow 7)$	M_3
18.3	$W(2 \rightarrow 5)$	M_3
18.4	$W(4 \rightarrow 6)$	M_3
18.99	$\Sigma_4 \rightarrow \Sigma_1$ $(4 \rightarrow 6)$	M_3
19.79	$W(4 \rightarrow 7)$, $(3 \rightarrow 6)$	M_3
20.105	$K_1 \rightarrow K_1$	M_0
21.2	$W(3 \rightarrow 7)$	M_3
21.7	$\Sigma_1 \rightarrow \Sigma_1$	M_3
21.704	$K_4 \rightarrow K_2$	M_3
24.755	$X(4 \rightarrow 7)$	M_3

Table IV.

Form Factor (symmetric)	Scaled from Si	Actual Values Used
$V^S(200)$	-0.076 Ryd.	-0.083 Ryd.
$V^S(220)$	0	-0.0186
$V^S(222)$	0.036	0.047

Table V.

Form Factor (Antisymmetric)	Numerical Value
$V^A(111)$	0.1448 Ryd.
$V^A(311)$	-0.0255

Table VI.

Prominent Interband Transitions	Energy (theory) (eV)	Energy (experiment) (eV)
$\Gamma_{15} \rightarrow \Gamma_1$	8.97	8.967
$L_3 \rightarrow L'_2$	9.86	9.5±0.3
$\Lambda_3 \rightarrow \Lambda_1$	10.29	10.±0.3
$X'_5 \rightarrow X_3$	10.34	
$X'_5 \rightarrow X_1$	10.42	10.5
$\Delta_5 \rightarrow \Delta_1$	11.07	11.±0.2
$\Sigma_4 \rightarrow \Sigma_1$	11.32	11.4±0.2
$L_3 \rightarrow L'_3$	12.26	12.26 (peak)
$\Gamma_{15} \rightarrow \Gamma'_{25}$	12.68	13.±0.3

Table VII

Calculated critical point energy (eV)	Band transition	Symmetry
8.97	$\Gamma_{15} \rightarrow \Gamma_1$	M_0
9.86	$L_3 \rightarrow L_2'$	M_0
10.29	$\Lambda_3 \rightarrow \Lambda_1$ $(4 \rightarrow 5)$	M_2
10.35	$X_5' \rightarrow X_3$	M_0
10.43	$X_5' \rightarrow X_1$	M_0
11.07	$\Delta_5 \rightarrow \Delta_1$ $(4,3 \rightarrow 5)$	M_1
11.25	$L_1 \rightarrow L_2'$	M_1
11.32	$\Sigma_4 \rightarrow \Sigma_1$ $(4 \rightarrow 5)$	M_2
11.33	$X_4' \rightarrow X_3$ (forbidden)	M_0
11.41	$X_4' \rightarrow X_1$	M_0
11.64	$\Delta_1 \rightarrow \Delta_2'$ (forbidden)	M_0
	$\Delta_1 \rightarrow \Delta_1$ $(2 \rightarrow 5)$	M_1
11.74	$\Delta_1 \rightarrow \Delta_1$ $(2 \rightarrow 6)$	M_1
11.74	$\Sigma_4 \rightarrow \Sigma_3$ (forbidden)	M_1
11.82	$\Sigma_3 \rightarrow \Sigma_1$ $(3 \rightarrow 5)$	M_2
12.04	$\Sigma_3 \rightarrow \Sigma_3$	M_1
12.1	W $(4 \rightarrow 5)$	M_3
12.24	$\Sigma_1 \rightarrow \Sigma_1$	M_2
12.25	$L_1 \rightarrow L_3'$ $(4 \rightarrow 6)$	M
	$L_3 \rightarrow L_3'$ $(4 \rightarrow 7)(3 \rightarrow 6,7)$	M_0
12.4	$\Sigma_1 \rightarrow \Sigma_3$	M_1
12.6	W $(2,3 \rightarrow 5)$	M_3
12.61	$\Lambda_1 \rightarrow \Lambda_1$ $(2 \rightarrow 6)$	M_2

Table VII (continued)

Calculated critical point energy (eV)	Band transition	Symmetry
12.64	$\Delta_5 \rightarrow \Delta_1$ $(3,4 \rightarrow 7)$	M_2
12.66	$\Lambda_3 \rightarrow \Lambda_3$ $(3,4 \rightarrow 6)$	M_3
12.67	$\Gamma_{15} \rightarrow \Gamma'_{25}$	M_0
12.7	$\Sigma_4 \rightarrow \Sigma_1$ $(4 \rightarrow 7)$	M_1
12.71	$\Lambda_3 \rightarrow \Lambda_1$ $(3,4 \rightarrow 6)$	M_3
12.77	$\Delta_5 \rightarrow \Delta'_2$	M_1
12.79	$\Sigma_4 \rightarrow \Sigma_3$ (forbidden)	M_3
12.8	$\Delta_5 \rightarrow \Delta'_2$	M_1
12.82	$\Sigma_3 \rightarrow \Sigma_3$	M_3
12.83	$\Lambda_1 \rightarrow \Lambda_1$ $(2 \rightarrow 6)$	M_2
12.86	$\Sigma_1 \rightarrow \Sigma_3$	M_3
12.89	$\Sigma_4 \rightarrow \Sigma_1$ $(4 \rightarrow 7)$	M_1
12.95	$\Lambda_3 \rightarrow \Lambda_3$ $(4 \rightarrow 7)$	M_3
	$(3 \rightarrow 7)$	M_2
12.99	$\Sigma_4 \rightarrow \Sigma_1$ $(4 \rightarrow 6)$	M_3
13.	$\Sigma_3 \rightarrow \Sigma_1$ $(3 \rightarrow 7)$	M_1
13.13	$\Delta_5 \rightarrow \Delta_1$ $(4 \rightarrow 7)$	M_3
13.02	$\Sigma_3 \rightarrow \Sigma_1$ $(3 \rightarrow 7)$	M_3
13.05	$\Delta_1 \rightarrow \Delta_1$ $(2 \rightarrow 7)$	M_0
13.13	$\Delta_5 \rightarrow \Delta_1$	M_3
13.24	$\Delta_1 \rightarrow \Delta_1$ $(2 \rightarrow 7)$	M_3
13.64	$L_1 \rightarrow L_3$ $(2 \rightarrow 6)$	M_3
	$(2 \rightarrow 7)$	M_1

Table VII (continued)

Calculated critical point energy (eV)	Band transition	Symmetry
13.64	W (2,3 → 6)	M_3
13.64	$\Sigma_3 \rightarrow \Sigma_1$ (3 → 6)	M_3
13.77	$\Sigma_1 \rightarrow \Sigma_1$ (2 → 6)	M_3
15.23	$X_5' \rightarrow X_2$	M_3
16.21	$X_4' \rightarrow X_2$ (forbidden)	M_3

Table VIII.

Form Factor	Numerical Values	Scaled Values
$V^S(200)$	-0.0886 Ryd.	-0.075 Ryd.
$V^S(220)$	-0.0597	-0.035
$V^S(222)$	0.0082	0.0073
$V^A(111)$	0.1410	0.14
$V^A(311)$	-0.0537	
V^d	-1.26	

Table IX.

Prominent Interband Transitions	Energy (theory) (eV)	Energy (experiment) (eV)
$\Gamma_{15} \rightarrow \Gamma_1$	8.69	8.69
$X_5' \rightarrow X_3$	10.06	9.9
$L_3 \rightarrow L_2'$	10.08	9.0
$\Lambda_3 \rightarrow \Lambda_1$	10.14	9.2
$X_5' \rightarrow X_1$	10.52	10.9
$\Delta_5 \rightarrow \Delta_1$	10.44	11.1
$\Sigma_4 \rightarrow \Sigma_1$	10.93	10.4
$L_3 \rightarrow L_3'$	12.13	11.2
$\Gamma_{15} \rightarrow \Gamma_{25}'$	11.45	11.6

Table X

Calculated critical point energy (eV)	Band transitions	Symmetry
8.69	$\Gamma_{15} \rightarrow \Gamma_1$	M_0
10.06	$X'_5 \rightarrow X_3$	M_0
10.08	$L_3 \rightarrow L'_2$	M_0
10.14	$\Lambda_3 \rightarrow \Lambda_1$ $(3,4 \rightarrow 5)$	M_1
10.44	$\Delta_5 \rightarrow \Delta'_2$ (strong)	M_1
10.5	$\Delta_5 \rightarrow \Delta'_1$ $(3,4 \rightarrow 6)$	M_0
	$\Delta_1 \rightarrow \Delta'_2$ (forbidden)	M_0
10.51	$X'_5 \rightarrow X_1$ $(3,4 \rightarrow 6)$	M_0
10.52	$X'_4 \rightarrow X_3$ (forbidden)	M_0
10.61	$\Delta_1 \rightarrow \Delta'_2$ (forbidden)	M_2
10.66	$\Delta_1 \rightarrow \Delta_1$ $(2 \rightarrow 6)$	M_0
10.93	$\Sigma_4 \rightarrow \Sigma_4$ $(4 \rightarrow 5)$	M_1
10.97	$\Sigma_4 \rightarrow \Sigma_3$ (forbidden)	M_2
10.97	$X'_4 \rightarrow X_1$	M_0
11.2	$\Sigma_3 \rightarrow \Sigma_3$	M_2
11.27	$\Sigma_1 \rightarrow \Sigma_3$	M_1
11.28	$\Sigma_3 \rightarrow \Sigma_1$ $(3 \rightarrow 5)$	M_2
11.32	$\Lambda_3 \rightarrow \Lambda_1$ $(3,4 \rightarrow 6)$	M_2
11.35	$\Sigma_1 \rightarrow \Sigma_1$	M_2
11.43	W $(3 \rightarrow 5)$	M_3
11.44	W $(2 \rightarrow 5)$	M_3
	W $(2 \rightarrow 6)$	M_0
11.45	$\Gamma_{15} \rightarrow \Gamma'_{25}$ $(4 \rightarrow 6)(3 \rightarrow 6)$ $(2 \rightarrow 6)$	M_3

Table X (continued)

Calculated critical point energy (eV)	Band transitions	Symmetry
11.45	$\Gamma_{15} \rightarrow \Gamma'_{25}$ $(4 \rightarrow 7)(3 \rightarrow 7)$ $(2 \rightarrow 7)$	M_0
11.46	$W(4 \rightarrow 7)$	M_0
11.74	$W(2 \rightarrow 7)$	M_0
12.13	$L_3 \rightarrow L'_3$ $(4 \rightarrow 6)$	M_3
	$(4 \rightarrow 7)$	M_1
	$(3 \rightarrow 6)(3 \rightarrow 7)$	M_2
12.14	$\Sigma_4 \rightarrow \Sigma_1$ $(4 \rightarrow 7)$	M_2
12.35	$\Delta_5 \rightarrow \Delta_5$	M_2
12.45	$\Sigma_3 \rightarrow \Sigma_1$ $(3 \rightarrow 7)$	M_2
12.51	$\Delta_1 \rightarrow \Delta_5$	M_2
12.52	$\Sigma_1 \rightarrow \Sigma_1$ $(2 \rightarrow 7)$	M_2
12.7	$L_1 \rightarrow L'_3$	M_3
12.85	$X'_5 \rightarrow X_5$	M_3
13.31	$X'_4 \rightarrow X_5$	M_3

REFERENCES

1. R. Hilsch and R. W. Pohl, Z. Physik 59, 812 (1930).

2. E. G. Schneider and H. M. O'Bryan, Phys. Rev. 51, 293 (1937); J. E. Eby, K. J. Teegarden and D. B. Dutton, ibid, 116, 1099 (1959); K. J. Teegarden and G. Baldini, ibid, 155, 896 (1967); F. Fischer and R. Hilsch, Nachr. Akad. Wiss. Goettingen II, Math. Physik Kl. 8, 241 (1959); F. Fischer, Z. Physik 160, 194 (1960).

3. P. L. Hartman, J. R. Nelson and J. G. Siegfried, Phys. Rev. 105, 123 (1957); J. W. Taylor and P. L. Hartman, ibid, 113, 1421 (1959); H. R. Phillipp and H. Ehrenreich, ibid, 131, 2016 (1963); T. Tomiki, J. Phys. Soc. Japan 22, 463 (1967); G. Baldini and B. Bosacchi, Phys. Rev. 166, 863 (1968).

4. D. M. Roessler and W. C. Walker, Phys. Rev. 166, 599 (1968).

5a. W. Shockley, Phys. Rev. 50, 754 (1936).

5b. S. R. Tribbs, Trans. Faraday Soc. 35, 1471 (1939).

5c. R. C. Casella, Phys. Rev. 104, 1260 (1956).

6a. L. P. Howland, Phys. Rev. 109, 1927 (1958).

6b. S. Oyama and T. Miyakawa, J. Phys. Soc. Japan 21, 868 (1966).

6c. P. D. Decicco, Phys. Rev. 153, 931 (1967).

7. M. L. Cohen and T. K. Bergstresser, Phys. Rev. 141, 789 (1966); T. K. Bergstresser and M. L. Cohen, ibid, 164, 1069 (1967); T. K. Bergstresser, Thesis, the University of California (1966) and reference therein.

8. J. C. Phillips, Phys. Rev. 122, 685 (1958); J. C. Phillips and L. Kleinman, ibid, 116, 287 (1959) and L. Kleinman and J. C. Phillips, ibid, 118, 1153 (1960).

9. M. H. Cohen and V. Heine, Phys. Rev. 122, 1821 (1961).

10. B. J. Austin, V. Heine and L. J. Sham, Phys. Rev. 127, 276 (1962).

11. I. V. Abarenkov and V. Heine, Phil. Mag. 9, 451 (1964); ibid, 12, 529 (1965).

12. A. O. E. Animalu and V. Heine, Phil. Mag. 12, 1249 (1965).

13. W. A. Harrison, Pseudopotential in Metals, Benjamin Press (1963), and references therein.

14. M. L. Cohen, P. J. Lin, D. M. Roessler and W. C. Walker, Phys. Rev. 155, 992 (1967).

15. D. M. Roessler and W. C. Walker, Phys. Rev. 159, 733 (1967).

16. J. C. Phillips, in Solid State Physics, F. Seitz and D. Turnbull, eds. (Academic Press Inc., New York, 1965), Vol. 16 and references therein.

17. D. Brust, Phys. Rev. 134, A1337 (1964).

18. D. M. Roessler and W. C. Walker, Phys. Rev. Letters 17, 319 (1966).

19. T. K. Bergstresser, W. Saslow, C. Y. Fong, M. L. Cohen, and D. Brust, Solid State Comm. 5, 667 (1967).

20. J. Walter, to be published.

21. K. L. Shaklee, J. E. Roew, M. Cardona, preprint, Brown University.

22. M. J. G. Lee and L. M. Falicov, to be published Roy. Soc. Proc. A.

23. C. Kittel, Introduction to Solid State Physics, 3 ed., John Wiley and Sons, Inc., New York, 1966, p. 105.

24. J. C. Phillips, Phys. Rev. 136, 1705 (1964).

A1. P. M. Morse and H. Feshbach, Methods of Theoretical Physics, Vol. 2, p. 1574, McGraw-Hill Book Company, 1953; J. D. Jackson, Classical Electrodynamics, John Wiley and Sons, Inc., 1962, p. 68.

APPENDIX I

Evaluation of Matrix Elements for ℓ=2 Nonlocal Pseudopotential

The form of the d-character nonlocal pseudopotential is

$$V_{NL}(\underline{r}) = \sum_{\underline{R}_j} V_2(|r - R_j|)\, P_2^{\ell}\, P_2^{r} \qquad (A1)$$

where $\underline{R}_j$ is the lattice vector.

P_2^{ℓ}, P_2^{r} are the projection operators defined in the text.

$$\begin{aligned} V_2(\underline{r} - \underline{R}_j) &= A_2 \qquad && \text{for } |\underline{r} - \underline{R}_j| \leq R_s \\ &= 0 && \text{for } |\underline{r} - \underline{R}_j| > R_s \end{aligned} \qquad (A2)$$

A_2 is the depth of the potential well and is treated as a parameter, in unit of rydbergs.

R_s = 1.33A for the radius of the K^+ ion.

The matrix element of $V_{NL}(\underline{r})$ is evaluated over the basis set, in the form of $e^{i(\underline{k}+\underline{G})\cdot\underline{r}}$

$$\langle V_{NL}\rangle = \langle e^{i(k+G')\cdot r}|V_{NL}|e^{i(\underline{k}+\underline{G})\cdot\underline{r}}\rangle = \sum_{\underline{R}_j}\int e^{-i(\underline{k}+\underline{G})\cdot\underline{r}}$$

$$V_2(|\underline{r}-\underline{R}_j|)\, P_2^{\ell}\, P_2^{r}\, e^{i(k+G)\cdot r}\, d^3r \qquad (A3)$$

Let $\underline{r}' = \underline{r}-\underline{R}_j$

$$\langle V_{NL}\rangle = \frac{V}{\Omega}\int_{cell} e^{-i(\underline{k}+\underline{G}')\cdot\underline{r}'}\, V_2(r')\, P_2^{\ell}\, P_2^{r}\, e^{i(\underline{k}+\underline{G})\cdot\underline{r}'}\, d^3r' \qquad (A4)$$

where Ω is the volume of the unit cell and V is the volume of the crystal.

The volume V will cancel out with the other terms in the pseudopotential Hamiltonian.

Expanding the plane wave in terms of spherical hamonics and Bessel's functions,[A1] we get,

$$e^{i(\underline{k}+\underline{G})\cdot\underline{r}'} = 4\pi \sum_{\ell=0}^{\infty} \sum_{m=-\ell}^{\ell} i^{\ell} j_{\ell}(|\underline{k}+\underline{G}| r') \, Y^{*}_{\ell m}(\theta_{\underline{G}}, \phi_{\underline{G}}) \, Y_{\ell m}(\theta', \phi') \quad (A5)$$

The geometry of the angles and vectors are shown in Fig. A1. We apply the projection operators P_2^{ℓ} and P_2^{r} and obtain

$$P_2^{r} \, e^{i(\underline{k}+\underline{G})\cdot\underline{r}'} = 4\pi \sum_{m=-2}^{2} (-1) \, j_2(|\underline{k}+\underline{G}| r') \, Y^{*}_{2m}(\theta_{\underline{G}}, \phi_{\underline{G}}) \, Y_{2m}(\theta', \phi')$$

$$(A6)$$

$$P_2^{\ell} \, e^{-i(\underline{k}+\underline{G})\cdot r'} = 4\pi \sum_{m=-2}^{2} (-1) \, j_2(|\underline{k}+\underline{G}| r') \, Y_{2m}(\theta_{\underline{G}}, \phi_{\underline{G}}) \, Y^{*}_{2m}(\theta', \phi')$$

Putting (A6) into (A4),

$$\langle V_{NL} \rangle = \frac{A_2 V}{\Omega} \sum_{m=-2}^{2} \int_0^{R_S} r'^2 \, dr' (4\pi)^2 j_2(|\underline{k}+\underline{G}'| r') \, j_2(|\underline{k}+\underline{G}| r') \, Y_{2m}(\theta_{G}', \phi_{G}') \, Y^{*}_{2m}(\theta_{\underline{G}}, \phi_{\underline{G}}) \quad (A7)$$

The summation over m can be simplified[A1] by

$$P_2(\gamma) = \frac{4\pi}{5} \sum_{m=-2}^{2} Y^{*}_{2m}(\theta, \phi) \, Y_{2m}(\theta', \phi') \quad (A8)$$

where $P_2(\gamma)$ is the Legendre polynomial.

$$\cos \gamma = \cos \theta \cos \theta' + \sin \theta \sin \theta' \cos(\phi-\phi')$$

$\langle V_{NL} \rangle$ can then be expressed in terms of the radial integral only,

$$\langle V_{NL} \rangle = \frac{A_2 V}{\Omega} \cdot 20\pi \cdot P_2(\gamma) \int_0^{R_S} r'^2 dr' \, j_2(|\underline{k}+\underline{G}| r') \, j_2(|\underline{k}+\underline{G}'| r') \tag{A9}$$

We separate the radial integral into three cases: a. the diagonal matrix element; b. the off-diagonal matrix element with $|\underline{k} + \underline{G}| = |\underline{k} + \underline{G}'|$; c. the off-diagonal matrix element with $|\underline{k} + \underline{G}| = |\underline{k} + \underline{G}'|$. All the following integrations are tabulated in Ref. A1.

a. $$\langle V_{NL} \rangle = \frac{A_2 V}{\Omega} \cdot 10\pi \cdot R_s^3 \, [j_2^2(|\underline{k}+\underline{G}|R_s) - j_1(|\underline{k}+\underline{G}|R_s) \, j_3(|\underline{k}+\underline{G}|R_s)] \tag{A10}$$

b. $$\langle V_{NL} \rangle = \frac{A_2 V}{\Omega} \cdot 10\pi \cdot P_2(\gamma) \, R_s^3 \, [j_2^2(|\underline{k}+\underline{G}|R_s) - j_1(|\underline{k}+\underline{G}|R_s) \, j_3(|\underline{k}+\underline{G}|R_s)] \tag{A11}$$

c. $$\langle V_{NL} \rangle = \frac{A_2 V}{\Omega} \cdot 20\pi \cdot P_2(\gamma) \left[\frac{R_S^2}{|\underline{k}+\underline{G}'|^2 - |\underline{k}+\underline{G}|^2} \right] \cdot \Big[|\underline{k}+\underline{G}| \, j_2(|\underline{k}+\underline{G}'|R_s) \, j_1(|\underline{k}+\underline{G}|R_s) - |\underline{k}+\underline{G}'| \, j_1(|\underline{k}+\underline{G}'|R_s) \, j_2(|\underline{k}+\underline{G}|R_s) \Big] \tag{A12}$$

where

$$\cos \gamma = \cos \theta_{\underline{k}+\underline{G}} \cos \theta_{\underline{k}+\underline{G}'} + \sin \theta_{\underline{k}+\underline{G}} \sin \theta_{\underline{k}+\underline{G}'} \cos(\phi_{\underline{k}+\underline{G}} - \phi_{\underline{k}+\underline{G}'})$$

ACKNOWLEDGMENTS

I would like to express my deep gratitude to Professor Marvin L. Cohen for suggesting this investigation. His kindness, patience and encouragement are greatly appreciated.

I am also deeply indebted to Professor C. Kittel. Without his kindness, I should not have had the change to work in the Solid Theory Group at Berkeley.

I would like to thank Professor W. C. Walker and Dr. D. M. Roessler for sending their data prior to publication and for many helpful discussions, and Professor L. Brewer and the Inorganic Materials Research Division of the Lawrence Radiation Laboratory for providing the convenience in using the computer facilities at U.C. LRL. I wish to thank Professor L. M. Falicov for the help in the nonlocal pseudopotential, and Professor J. C. Phillips for the discussions of the results of KCl.

Thanks are due to the faculty members in the Department of Physics, in particular, Professor Y. R. Shen, with whom I have had many interesting discussions.

I would like to thank Miss Y. Tung, Mr. L. Sander and Mr. J. Walter, Mr. W. Au-Yang, Mr. P. Allen for many helpful discussions and Mr. J. Chang for help on the last part of the calculation of KCl. Thanks are also due to Mr. W. Saslow for teaching me how to use the computer program.

I wish to thank Mrs. Madeline Moore for typing the parts of this work being published and Mrs. Pat Shand for her typing of this work.

The financial support of the National Science Foundation and the United States Atomic Energy Commission is gratefully acknowledged.